LAPPEENRANTA UNIVERSITY OF TECHNOLOGY
LUT School of Energy Systems
Degree Program in Electrical Engineering

Master's Thesis
2018

Aleksi Riitala

ESTIMATING THE SPEED OF A PERMANENT MAGNET SYNCHRONOUS MACHINE USING MAGNETIC LEAKAGE FLUX

Examiners: Professor Juha Pyrhönen
D.Sc. (Tech.) Andrej Burakov

Abstract

Lappeenranta University of Technology
LUT School of Energy Systems
Degree Program in Electrical Engineering

Aleksi Riitala

Estimating the speed of a permanent magnet synchronous machine using magnetic leakage flux

Master's Thesis

2018

113 pages, 61 figures, 11 tables and 1 appendix.

Examiners: Professor Juha Pyrhönen
D.Sc. (Tech.) Andrej Burakov

Keywords: speed control, angle estimation, leakage flux, stray flux, PMSM, elevator system

A precise speed control of an elevator is essential for passenger safety and ride comfort. Modern speed control solutions for electric machines enable a high degree of accuracy and precision, but they often come with substantial costs. Elevator manufacturers operate in a highly competitive industry which has strict requirements for product quality and safety, but also a high cost pressure. In this work, it is investigated whether it is possible to determine the rotation speed of an elevator motor by just using the magnetic stray flux created by the permanent magnets embedded in the machine. As the machine rotates, a signal created by the magnetic flux resembles a sine wave. Using a suitable post-processing method and an analog-to-digital converter, the speed of the machine can be calculated without the need for an expensive angle sensor. A leakage flux–based speed estimation method is evaluated both with simulated and measured leakage flux data. The most significant error sources are identified and possible correction methods are discussed. Using suitable error correction, the speed information is calculated with sufficient accuracy.

Tiivistelmä

Lappeenrannan teknillinen yliopisto
LUT School of Energy Systems
Sähkötekniikan koulutusohjelma

Aleksi Riitala

Kestomagneettitahtikoneen hajavuoperusteinen nopeusmittaus

Diplomityö

2018

113 sivua, 61 kuvaa, 11 taulukkoa ja 1 liite

Tarkastajat: Professori Juha Pyrhönen
TkT Andrej Burakov

Hakusanat: nopeussäätö, kulman arviointi, hajavuo, kestomagneettitahtikone, hissikäyttö
Keywords: speed control, angle estimation, leakage flux, stray flux, PMSM, elevator system

Hissin tarkalla nopeussäädöllä on olennainen vaikutus matkustajien turvallisuuteen ja ajomukavuuteen. Nykyaikaiset nopeussäätöjärjestelmät mahdollistavat korkean tarkkuuden, mutta ovat usein kalliita. Hissivalmistajat toimivat tiukasti kilpaillussa ympäristössä, jossa tuotteiden laadulle ja turvallisuudelle on tarkat vaatimukset, mutta myös kova hintapaine. Tässä työssä tutkitaan, voisiko hissimoottorin pyörimisnopeuden laskea hyödyntämällä moottoriin asennettujen kestomagneettien tuottamaa magneettista hajavuota. Moottorin pyöriessä hajavuon indusoima signaali muistuttaa siniaaltoa. Sopivalla jälkikäsittelymenetelmällä ja A/D-muuntimella koneen pyörimisnopeus voidaan selvittää ilman kallista kulmasensoria. Työssä arvioidaan hajavuoperusteisen nopeudenlaskentamenetelmän soveltuvuutta sekä simuloiduilla että mitatuilla hajavuotiedoilla. Myös merkittävimpiä virhelähteitä ja niihin soveltuvia korjausmenetelmiä käsitellään. Sopivaa virheenkorjausta käyttämällä nopeustieto saadaan laskettua riittävällä tarkkuudella.

Preface

This thesis was carried out for the Machinery R&D team at KONE Oyj between January and May 2018. I would like to express my gratitude to the team members for giving me this opportunity to work with an interesting research topic in a supportive and positive working environment. Many thanks to all the people who helped me at different stages of the project.

In particular, I would like to thank my instructor at KONE, Dr. Andrej Burakov for guiding me throughout the project and providing helpful advice and helpful ideas when I needed them. I would also like to thank my supervisor at LUT, Prof. Juha Pyrhönen for examining this thesis and for numerous engaging lectures during my studies.

Finally, I would like to thank my family for always supporting me and my friends for an unforgettable student life.

Hyvinkää, May 30th, 2018

Aleksi Riitala

Table of Contents

1 Introduction **6**

1.1 Objectives and restrictions 7

1.2 Structure of the thesis 8

1.3 Previous work 9

2 Magnetic flux and its measurement **12**

2.1 Permanent magnet synchronous motors 12

2.2 Leakage flux of a PMSM 14

2.2.1 Magnet edge leakage flux 20

2.3 Finite element analysis 21

2.4 Measuring the magnetic flux 23

2.4.1 Hall probe 23

2.4.2 Magnetoresistor 24

2.4.3 Fluxgate Magnetometer 25

3 PMSM control **28**

3.1 Speed and position feedback for PMSMs 28

3.1.1 Vector control of a PMSM 30

3.1.2 PMSM control schemes 34

3.1.3 Sensorless position estimation 34

3.2 Position and velocity feedback devices 35

3.2.1 Incremental encoder 36

3.2.2 Absolute encoder 37

3.2.3 Resolver 39

3.2.4 Tachometer 40

3.3 Speed calculation in an elevator system 41

3.3.1 Performance requirements for position feedback 43

4 Speed estimation using rotor leakage flux **46**
4.1 Magnet edge leakage flux waveforms . . . 47
4.2 Inverse tangent method . . . 50
4.2.1 Coarse angle calculation . . . 51
4.2.2 Fine angle calculation . . . 53
4.2.3 Total angle calculation . . . 56
4.3 Inverse sine method . . . 58
4.4 ANF-PLL filter method . . . 60
4.4.1 Adaptive notch filter . . . 60
4.4.2 Phase-locked loop . . . 64

5 Modeling the leakage flux measurement **68**
5.1 Simulation model . . . 68
5.2 Simulation results . . . 74

6 Experimental procedure and analysis **81**
6.1 Measurement system . . . 81
6.2 Machine 1 . . . 83
6.3 Machine 2 . . . 89
6.4 Simulations with measured signals . . . 92
6.5 Discussion . . . 99

7 Conclusions **102**
7.1 Summary . . . 103
7.2 Future work . . . 105

Nomenclature

Notations

A	area, amplitude
B	magnetic flux density
d	diameter
H	Hall signal
i	current
j	imaginary unit
L	inductance
l	length
m	position updates per electrical angle
n	rotation speed, index
P	power
p	number of pole pairs
R	reluctance
S	switching function variable
s	Laplace domain operator
T	torque
t	time
U	voltage
z	z-domain operator
β	reluctance ratio
δ	angle error
λ	magnet-to-magnet leakage flux ratio
μ_0	permeability in vacuum
μ_r	relative permeability
ν	magnet-end leakage flux ratio
Ω	mechanical angular speed
ω	angular speed

Φ	magnetic flux
ρ	filter pole
σ	filter gain
θ	angle

Abbreviations

AC	Alternating current
ADC	Analog to digital converter
ANF	Adaptive notch filter
DC	Direct current
DSP	Digital signal processor/processing
EMF	Electromotive force
FEM	Finite element method
ID	Identification
IIR	Infinite impulse response
IPM	Interior permanent magnet
IPMSM	Interior permanent magnet synchronous machine
LF	Loop filter
MTPA	Maximum torque per ampere
MTPV	Maximum torque per voltage
N	Magnetic north pole
PD	Phase detector
PI	Proportional-integral
PLL	Phase-locked loop
PM	Permanent magnet
PMSM	Permanent magnet synchronous machine
ppr	Pulses per revolution
S	Magnetic south pole
SHA	Sample and hold amplifier
THD	Total harmonic distortion
UPS	Uninterrupted power source
VCO	Voltage-controlled oscillator
XOR	Exclusive or

Subscripts

0	fundamental

D	damper winding on d-axis
d	direct axis
e	electrical
err	error
g	air gap
h	harmonic
i	integral
m, ma	magnet, magnetic, magnetizing
max	maximum
mech	mechanical
min	minimum
mm	magnet-to-magnet
mr	magnet-to-rotor
p	proportional
PM	permanent magnet
Q	damper winding on q-axis
q	quadrature axis
r	rotor, relative
s	stator
tr	traction sheave
U	phase U
V	phase V
W	phase W
x	x-axis
y	y-axis
α	cosine
β	sine

Superscripts and other notations

$\hat{x}$	estimated value of x
$\tilde{x}$	estimation error of x
*	reference value

Chapter 1

Introduction

Speed control of an electric motor is an essential requirement in a broad range of control applications. In some devices, like pumps and fans, speed control is relatively easy since most of the time they are designed to run at a constant speed and their voltage can also be kept constant. In other fields, an exact speed and position control of the motor is among the most desired features. This is especially true in elevators, where any variations in speed can be felt by passengers. Motor control must ensure an adequate ride comfort especially in passenger elevators as human beings are very susceptible to fluctuations in speed. Moreover, a jerky ride may cause a perception of the elevator equipment being defective or unreliable. Elevator car speed cannot have large oscillations even during acceleration or deceleration. The load in the elevator car can change after every stop. As a result the requirements for the control systems in elevators are significantly stricter than for example in pumps or fans.

In synchronous machines, accurate torque production can only be achieved when the frequency of the alternating current in the stator is precisely synchronized with the rotation speed of the rotor. Traditionally, synchronization between the stator and the rotor is ensured by continuously measuring the absolute angular position of the rotor and the phase angle of the stator current. The angular position measurement is often done with an encoder. Although modern encoders can reach a high accuracy, they also have a number of drawbacks like high cost, accuracy deterioration over time and strict mechanical mounting requirements. When using an encoder, the absolute angle of the rotor is not known immediately after start-up. For these reasons, multiple *sensorless* control methods have been investigated.

In sensorless methods, the need for continuous angle measurement with an encoder or other

type of angle measurement device is eliminated. In this thesis, the rotor angle is attempted to be measured using the magnetic field created by the permanent magnets (PM) in the electric motor. This magnetic leakage flux–based angle measurement method takes a similar approach as sensorless control methods, using the characteristics of the machine in an attempt to sense the rotor angle. The final angle measurement method should be accurate and robust, since wrong angle information can easily lead to oscillations in the speed control system. These oscillations are then transformed into torque oscillations of an elevator motor, which, in turn, contributes to speed fluctuations of an elevator car. For a company operating in an elevator industry, providing a smooth and quiet ride experience is a key to ensure high perceived quality of its products and, hence, a great reputation.

As in any highly competitive industry, at the same time different components of the elevator system have a high cost pressure. In the end, a customer makes the decision on how much they are willing to pay for certain features. A speed measurement system based on the magnetic flux has a potential to be highly affordable.

This master's thesis is conducted for the elevator and escalator industry company KONE Corporation, headquartered in Espoo, Finland. Measurements for this thesis are performed in a research and development center of KONE, located in Hyvinkää, Finland. All measurement tools and test motors were provided by the company.

1.1 Objectives and restrictions

The objective of this thesis is to investigate a solution for position and speed estimation of an elevator motor using the magnetic leakage flux from the motor. The thesis is trying to address the following question:

"Is it possible to use the magnetic leakage flux from a permanent magnet synchronous motor as a feedback signal in order to accurately control the speed and position of an elevator?"

Investigation regarding the acceptance or rejection of this statement is the main goal of this thesis. The new solution should be safe, robust and low-cost. The thesis should give a better understanding of the behavior of the leakage flux in elevator motors ranging from small to medium sizes and operating at different speeds. The research is carried out using a literature review, simulations in software and a series of measurements. Two different motors are

measured, mostly in nominal speed and nominal torque range but also in situations when distortions in the leakage flux are larger. A comparison between currently used technologies and the presented system should be included in the thesis.

It is not in the scope of this thesis to attempt to develop a finished product, but rather to give specifications and suggestions for possible further development. Therefore it can be described as a feasibility study for the leakage flux–based speed measurement system.

As mentioned in the thesis question, this work focuses on permanent magnet synchronous machines (PMSMs) since they cover most of the electric machines produced by KONE. The difference between axial- and radial flux machines is shown in Figure 1.1. In KONE's axial flux machines the magnets are encapsulated into the motor structure with no obvious ways of directly measuring their leakage flux. The flux outside the machine is also minimal. For this reason the scope of this thesis is limited to radial flux machines. The location of PMs in radial flux motors used in KONE elevators makes it suitable for leakage flux measurements.

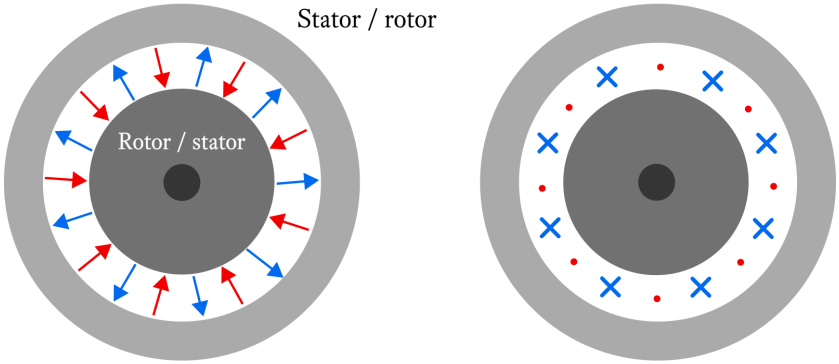

Figure 1.1. A radial flux machine (left) and an axial flux machine (right). In a radial flux machine, the main magnetic flux is oriented perpendicular to the machine axis, whereas in an axial flux machine it is oriented in parallel with the axis.

1.2 Structure of the thesis

The outline of the thesis is organized as follows:

Chapter 2 begins with an introduction to the thesis topic. Basic principles of PMSMs and

the physical background of leakage flux is described here. The leakage flux is covered both analytically and using finite element simulations. This section also covers different devices used to measure magnetic flux.

Chapter 3 briefly presents different control methods of PMSMs. The focus is on vector control methods. Angular feedback devices used in current systems are introduced here. The chapter concludes by describing speed estimation schemes in elevator systems.

Chapter 4 covers the particular magnetic leakage flux component used for speed estimation in more detail. Different methods for calculating rotation speed from the leakage flux are introduced. Three alternatives are presented based on the leakage flux waveform of an interior permanent magnet synchronous machine (IPMSM).

Chapter 5 continues by a presenting a simulation model used to analyze one of the speed estimation schemes. Different parts of the model are described individually. Results obtained by feeding an artificially generated measurement signal to the simulation model are also analyzed.

Chapter 6 describes the experimental section of the thesis. It covers the different setups, measurement devices and experiments. Measurement data gathered from the experiments is presented and analyzed.

Finally, Chapter 7 presents the conclusions of the investigation, a summary section, as well as suggestions for future research on the subject. The thesis finishes with a list of references and a full schematic of the simulation model.

1.3 Previous work

A lot of research has been conducted in the area of speed control of PMSMs. Using the leakage flux of the PMs as a source for speed information is, however, quite an uncommon research topic. Instead, the leakage flux has been widely investigated as means of monitoring the condition of an electric motor for example in (Kokko, 2003), (Goktas et al., 2016) and (Goktas et al., 2017). The basic principle in this type of condition monitoring is to mount magnetometers into specific locations around the motor and analyze the recorded flux pattern in either time or frequency domain. Different magnetic defects, like broken magnets, magnet imperfections and demagnetization, produce specific patterns into the leakage flux spectrum which can then be

identified based on previously recorded data. Leakage flux–based condition monitoring aims to avoid shortcomings in other condition monitoring systems, like phase current–based monitoring, by providing a monitoring system independent of winding type, load level, fault location and so on. In these studies the flux spectrum is analyzed at different torque-speed profiles, a method that was adopted also into this thesis.

In the field of speed control, sensorless control methods have been a subject of extensive research in order to reduce the cost and size of a rotor position estimation system like a shaft-mounted sensor. To compensate some of the limitations of sensorless methods, cheap magnetometers like Hall effect sensors have been proposed as being used in conjunction with the sensorless methods. In (Lidozzi et al., 2007), Hall sensors are used with back-EMF–based sensorless control, and in (Kim et al., 2011) they are used with a vector-tracking observer. In (Yang and Ting, 2014), Hall sensors are used to drive both surface-magnet PM motor and an interior-PM synchronous motor. These studies convert the signal from the Hall sensors to a discrete high/low signal, as opposed to sinusoidally shaped signals used in other studies. The basic configuration has three Hall sensors placed 120 electrical degrees apart from each other, together dividing each a full electrical cycle into six sections. This provides ±30 degrees of resolution which can then be improved by different signal processing or error correcting techniques.

In another branch of studies related to magnetic flux leakage in PMSMs, like in (Lee and Kim, 2017) and (Kiss and Vajda, 2014), the leakage flux is modeled for either axial or radial type of motor. Since leakage flux is essentially a loss of flux, these studies aim to minimize it by machine design choices. Time-consuming 3D FEM analysis is usually avoided and only used for verification of the analytical models. Design guidelines developed in these studies mostly rely on a magnetic circuit of a motor. In the motors used in this thesis, this kind of leakage flux has also been minimized, but the magnet edge flux used for the speed measurement is always present.

Leakage flux–based speed control systems have also been studied in a few studies. The motor types in these studies include an induction motor and different kind of PMSMs. The paper by (Adam et al., 2011) focuses mainly on the health-related effects that leakage flux from a PMSM can have on humans, but it is also mentioned that the flux has information that could be used to estimate rotor position. In (Ertan and Keysan, 2009), an external search coil was placed next to a stator in order to measure its leakage flux. Different coil shapes, axial positions and frame materials were investigated to achieve the best possible result. An offline algorithm to measure the speed of the rotor was developed and verified. The accuracy of the method was acceptable but low compared to a typical encoder.

In another past research, (Jung et al., 2010) and (Lee et al., 2017) have used leakage flux to drive a small, high-rotation-speed PM motor. In this case the flux was measured with Hall-effect sensors next to the PMs. The flux was observed to have a third harmonic component, and different methods were developed to compensate their effect, some of which are also tested in this thesis. It was concluded that the method was accurate enough for fans and pumps, where precise position control is not essential.

In the papers referred here the studied motors are used in applications requiring high speed but small torque. Many elevator motors differ from this since they have a low rotation speed but can carry large loads. Additionally, they are much larger in physical size and power level than the motors which have been previously researched for leakage flux–based speed control. For example the reaction caused by stator currents has mostly been ignored due to its relatively low significance. In this thesis the stator current has been taken into account, extending the range of motors for which a leakage flux–based speed estimation could be implemented.

Chapter 2

Magnetic flux and its measurement

In order to develop a speed estimation system based on magnetic flux, some basic understanding of the different flux components in a PMSM is required. The most popular method for describing magnetic behavior of an electric motor is using a magnetic circuit. In this chapter the main magnetic circuit of a radial flux PMSM is presented, along with the magnet edge leakage produced by the PMs inside the rotor that will be used for speed estimation in later chapters. Different methods for measuring the magnetic field are also discussed.

2.1 Permanent magnet synchronous motors

PMSMs have seen an increase in popularity as PM materials have become more accessible. PM machines have traditionally been targeted for servo drives, but they are also increasingly used as heavy-duty industrial motors. PMSMs have been gaining attention especially in wind power industry, and megawatt-range wind turbine generators are already widely used. Electric and hybrid car motor designs using PM technology are also common. All these applications require a high-torque and relatively low-speed machine, a category that includes also elevators. (Pyrhönen et al., 2016)

PMSMs are doubly excited machines which have two sources of excitation, the armature excitation and PM excitation. In conventional doubly excited machines, like DC machines and synchronous machines, both excitations are arranged with an electric winding. With PM technology, extremely high efficiencies can be reached, since in a well-designed PM machine rotor

losses can be negligible. The magnets in PMSMs eliminate the need for a second winding and its power source. Moreover, copper losses in the second winding are not present. Often the design can also be made lighter and more compact compared to conventional doubly excited machines. On the other hand, controlling the air gap flux is more difficult. In conventional machines it can be done easily by changing the field winding current.

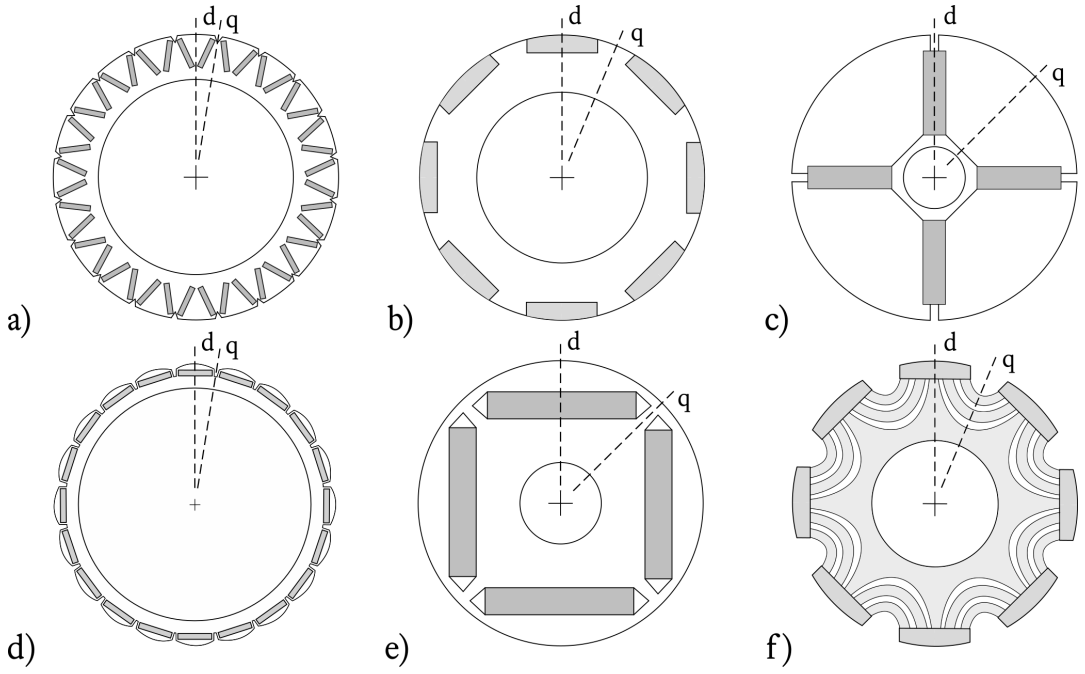

Figure 2.1. Different rotor configurations of PM machines. Constructions a), d) and e) use embedded magnets, f) uses surface magnets, b) uses inset magnets and c) is an I-type construction. The direct and quadrature axes have been marked for each configuration. (Pyrhönen et al., 2016)

Depending on the way the magnets are placed in the rotor, different rotor configurations have been developed. A coarse division can be made between surface-magnets and interior magnets. In surface-magnet type the magnets are mounted to the surface of the rotor, whereas in interior type they are inside the rotor core. Interior type configuration produces saliency, an inductance difference between the *direct* and *quadrature* axis of the motor. The magnetic flux produced by the magnets defines an axis radially through the center of the magnets, which is the direction of the maximum magnetic flux from the rotor, known as the direct axis. The quadrature axis is, in turn, defined as being orthogonal to the d-axis, so there is a 90 electrical degrees phase shift between them. The mechanical angle between d- and q-axis depends on the number of pole pairs in the motor. In a motor that has one pole-pair electrical and mechanical angles coincide. Because the permeability of the magnets is almost equal to air, the effective air gap is increased

on the d-axis, which results in higher reluctance than on the q-axis. In terms of inductance, the q-axis inductance is higher than the d-axis inductance. In a surface magnet machine like the configuration in Figure 2.1 f), the d-axis inductance is higher than the q-axis inductance.

2.2 Leakage flux of a PMSM

All electrical machines produce weak magnetic fields around them. The magnetic flux that they create is called a stray or leakage flux, since it does not contribute to the work that the machine is designed to be performing. Generally, it is favored to have a low leakage flux, since a high leakage directly reduces the output power of the motor. The leakage flux can be further divided into smaller components depending on which part of the motor they are present. The structure of a leakage flux in radial type PM motor is studied in this section.

The magnetic flux of an electrical machine is produced by the stator and rotor current linkages. In the stator, it is a product of the stator windings, whereas in the rotor it is a product of the rotor windings or, in the case of PMSMs, the magnets. The magnetic flux that is in the air gap produces torque for the machine. The flux in the air gap is always smaller than the total flux of the machine due to several leakage flux components.

As mentioned previously, there are two sources for the magnetic flux, the PMs and the stator winding currents. The part of the flux that links the stator and rotor is the main, useful flux. Any flux that originates from the magnets, but does not reach the stator can be considered leakage and is often called *magnet leakage flux*. Similarly, any flux that originates from the stator windings, but does not cross the air gap and reach the rotor is also considered stray flux. Part of the magnetic flux which makes it to the air gap can also be considered as leakage if it does not contribute to the main component of torque. These leakages are caused by harmonics in the air gap flux (Pyrhönen et al., 2009). A small part of the main flux also leaks outside the stator frame into the surrounding air.

Analytical models for leakage fluxes in different types of PMSMs have been proposed. A full model would consists of air gap, slot, end-winding and harmonic leakage fluxes. The air gap flux has by far the most effect on motor performance, since it determines the shape of the back-EMF. Regarding the air gap leakage flux, models have been developed for surface mounted PMs (Qu and Lipo, 2004) and embedded magnets (Tsai and Chang, 1999). Leakage flux in the

air gap has direct influence on the torque production of the machine. These models take into account the magnetic material properties and machine dimensions while attempting to provide an accurate prediction of torque. To get an understanding about how the leakage flux divides into different parts of the motor, an analytical model is presented for an IPMSM.

A simplified cross section of an IPMSM is presented in Figure 2.2. It shows the structure of a flux loop, traveling from one magnet to another through the air gap. The PMs are embedded inside the rotor steel. One section is sufficient for the whole analysis since the flux path repeats for every adjacent pole pair.

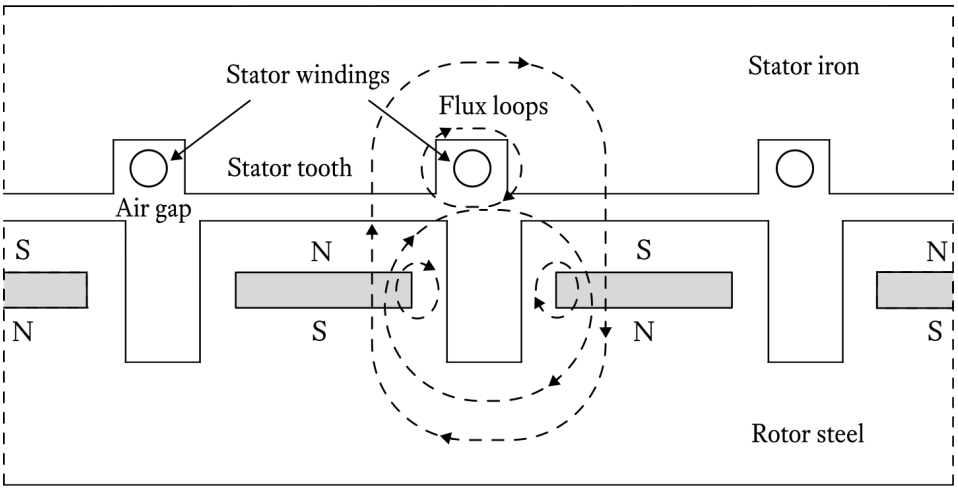

Figure 2.2. Flux loops in an interior type PM. Flux loops that do not cross the air gap are considered leakage flux. Here they are stator leakage and magnet-to-rotor leakage. Both magnets also produce magnet-end leakage.

Majority of the flux flows from the magnets across the air gap into the stator. The inner flux loops can be considered as leakage, since they do not cross the air gap. The stator winding produces stator leakage. Both magnets that are part of the flux loop also have their own magnet-end leakage flux.

A magnetic circuit formed by the structure in Figure 2.2 is presented in Figure 2.3. Magnetic circuits are analogous to electrical circuits, and Ohm's law and other circuit analysis tools can be used in their simplification. The magnetic circuit presented here consists of flux sources (corresponding to current sources in electrical circuits) and reluctances (corresponding to resistances). Different flux paths in the magnetic circuit have different reluctances, which affects the flow of the magnetic flux. Generally, a reluctance R_{m} is expressed as

$$R_{\mathrm{m}} = \frac{l}{\mu_0 \mu_{\mathrm{r}} A}, \tag{2.1}$$

where l is the length of the magnetic flux path, μ_0 is the permeability in vacuum, μ_{r} is the relative permeability of the material and A is the cross-sectional area of the circuit. To simplify the analysis, the magnetic field produced by the current in the stator windings is considered to be negligible compared to the flux produced by the PMs.

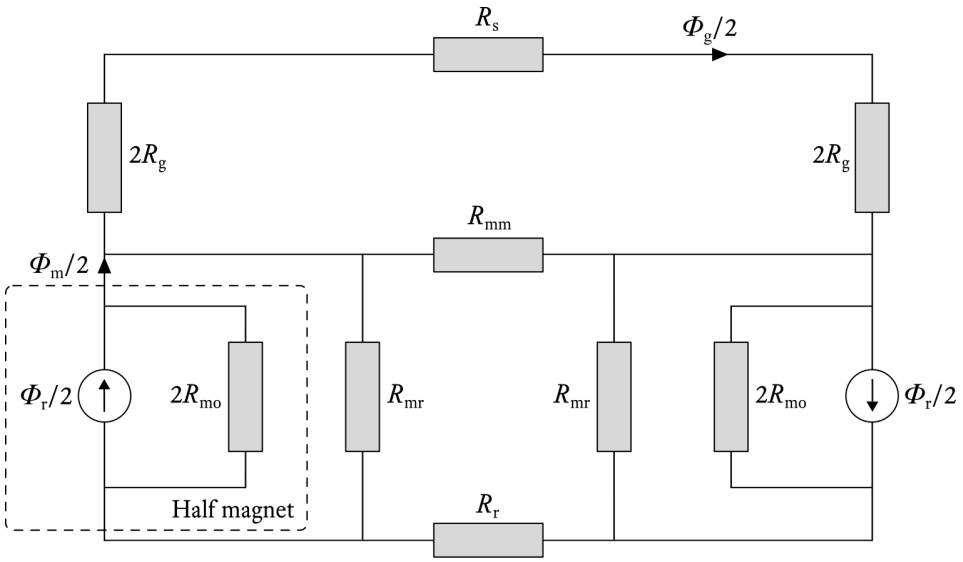

Figure 2.3. A magnetic circuit of an IPMSM. (Tsai and Chang, 1999)

The fluxes and reluctances are as follows:

Φ_{g}	air gap flux produced by one magnet pole
Φ_{r}	flux source of one magnet pole
R_{g}	reluctance corresponding to Φ_{g}
R_{ma}	reluctance of one magnet, corresponding to Φ_{r}
R_{s}	reluctance of the stator tooth and back iron
R_{r}	reluctance of the rotor back iron
R_{mr}	reluctance caused by magnet-to-rotor leakage flux
R_{mm}	reluctance caused by magnet-to-magnet leakage flux

The circuit shows how R_{mr} and R_{mm} are in parallel to R_{ma}. Each flux loop includes two magnet

halves from two adjacent magnets, and each half produces a flux equal to $\Phi_{\mathrm{r}}/2$ and has a reluctance of $2R_{\mathrm{ma}}$ in parallel to the flux source. Similarly, the air gap reluctance corresponding to the flux that is produced by a half magnet is $2R_{\mathrm{g}}$. The direction of the flux source indicates the magnet polarity, which is opposite for every adjacent magnet. The stator and rotor reluctances would introduce unwanted nonlinearities in the model due to their saturation effects, so they should be eliminated in order to reach an analytic solution. It is assumed that the stator and rotor steel are not saturated and they have much higher permeability than air, i.e. R_{s} and R_{r} are negligible compared to R_{g}. The simplified circuit is presented in Figure 2.4.

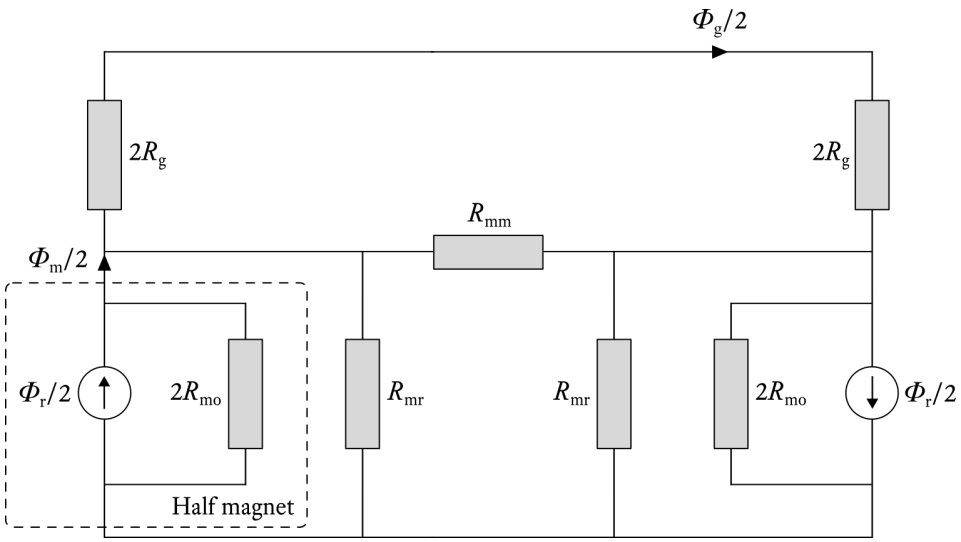

Figure 2.4. Simplified magnetic circuit. (Hwang and Cho, 2001)

The circuit can be further simplified by grouping the two half magnets together. From a electrical circuit point of view, the resulting magnet is found by determining the Norton equivalent circuit of the two magnet halves. One of the flux sources is shorted, and the equivalent reluctance of the two magnets is calculated. From physical perspective, having two half magnets in series is equivalent to a magnet material having twice the length. Therefore, the flux source remains unchanged but the reluctance is doubled from $2R_{\mathrm{ma}}$ to $4R_{\mathrm{ma}}$ since reluctance is directly proportional to material length. Two air gap reluctances in series are also combined to $4R_{\mathrm{g}}$. The resulting magnetic circuit is presented in Figure 2.5a. (Hanselman, 2006)

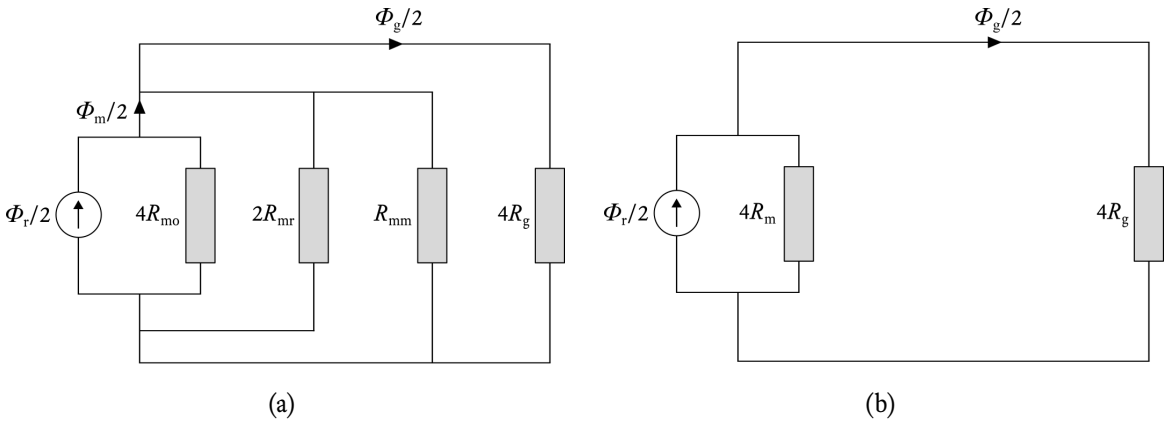

Figure 2.5. Magnetic circuits simplified further. (Tsai and Chang, 1999)

In Figure 2.5b, the resulting reluctance is R_{m} is defined as

$$R_{\mathrm{m}} = \frac{R_{\mathrm{ma}}}{1 + 2\eta + 4\lambda}, \tag{2.2}$$

where the leakage flux ratios are $\eta = R_{\mathrm{ma}}/R_{\mathrm{mr}}$ and $\lambda = R_{\mathrm{ma}}/R_{\mathrm{mm}}$. The dimensionless parameter η characterizes the magnet-end leakage flux and λ characterizes the magnet-to-magnet leakage flux. From the simplified circuit in Figure 2.5b, the relationship of the air gap flux to the total flux caused by the magnet can now be calculated.

$$\Phi_{\mathrm{g}} = \frac{R_{\mathrm{m}}}{R_{\mathrm{g}} + R_{\mathrm{m}}} \Phi_{\mathrm{r}} = \frac{1}{1 + \beta(1 + 2\eta + 4\lambda)} \Phi_{\mathrm{r}}, \tag{2.3}$$

where the reluctance ratio $\beta = R_{\mathrm{g}}/R_{\mathrm{ma}}$. From the equation it can be seen that the flux produced by the magnet is reduced by the air gap reluctance and the reluctance which depends on machine geometry.

In Figure 2.2, it can be seen that the leakage flux consists of two components, magnet-end leakage flux Φ_{mm} and magnet-to-rotor leakage flux Φ_{mr}, both of which can be derived from the magnetic circuit: (Hwang and Cho, 2001)

$$\Phi_{\mathrm{mm}} = \frac{2\beta\lambda}{1+\beta(1+2\eta+4\lambda)}\Phi_{\mathrm{r}}, \tag{2.4}$$

$$\Phi_{\mathrm{mr}} = \frac{\beta\eta}{1+\beta(1+2\eta+4\lambda)}\Phi_{\mathrm{r}}. \tag{2.5}$$

The flux leaving the magnet can now be calculated by adding the air gap flux Φ_{g} and the total leakage flux:

$$\Phi_{\mathrm{m}} = \frac{1+\beta(2\eta+4\lambda)}{1+\beta(1+2\eta+4\lambda)}\Phi_{\mathrm{r}}. \tag{2.6}$$

In terms of flux density, the flux in the air gap is expressed as

$$B_{\mathrm{g}} = \frac{A_{\mathrm{m}}/A_{\mathrm{g}}}{1+\beta(1+2\eta+4\lambda)}B_{\mathrm{r}}, \tag{2.7}$$

where B_{r} is the remanence flux density of the magnet in the rotor, A_{g} is the cross sectional area of the air gap for one pole and A_{m} is the cross sectional area of one magnet. The ratio $A_{\mathrm{m}}/A_{\mathrm{g}}$ can be thought as a *flux concentration factor*. Inside the magnet the flux density can be expressed as

$$B_{\mathrm{m}} = \frac{1+\beta(2\eta+4\lambda)}{1+\beta(1+2\eta+4\lambda)}B_{\mathrm{r}}, \tag{2.8}$$

which is analogous to Equation (2.6). With these equations, a machine designer can quickly get a general idea of how much of the main flux is going to different leakage flux components. Analytical calculation results obtained from the equations show that the magnet-end leakage flux is dominating in IPM designs. This means that in practice the magnet-end leakage flux ratio η is much larger than magnet-to-magnet leakage flux ratio λ. The result has also been verified by 2D FEM simulations (Tsai and Chang, 1999).

In general, a crucial aspect to be considered when designing an IPM machine is the part of the rotor that extends from the PM pockets towards the air gap. This *iron bridge* is interesting in

both electromagnetic and mechanical design perspectives since it has a major effect on the flux behavior. A thin iron bridge reduces the leakage flux and improves the electrical characteristics of the machine. On the other hand, the mechanical performance is compromised by a thin bridge, since centrifugal forces near the rotor edge will be more prominent. The iron bridge needs to be wide enough to support the rotor core laminations and the magnets against centrifugal load, but narrow enough to limit its involvement in the magnetic circuit. Iron bridges and flux barriers are shown in Figure 2.6.

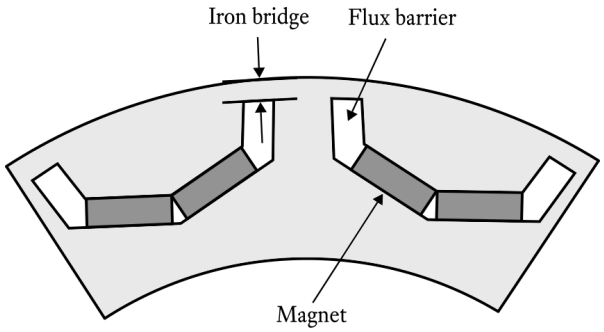

Figure 2.6. A cross-section of an IPMSM rotor illustrating the concept of iron bridges and flux barriers.

Another important design choice is the length of the flux barriers. In IPMSMs, they are for example air pockets next to the PMs that are mainly used to increase motor saliency, but can also limit the leakage flux through magnetic short-circuits between two adjacent magnets. A good flux barrier guides the flux to the direction of the air gap.

2.2.1 Magnet edge leakage flux

Up to this point the thesis has focused on the flux in the radial and tangential directions of the machine. However, in practice it might be difficult to measure the flux directly, since it is mostly flowing inside the stator and rotor iron. Another place to look for the leakage flux is the air gap, but since its length has a major impact on the machine performance, one might not want to modify it by adding a measurement device. In addition, air gaps are usually only a couple of millimeters long, so a physical sensor would be difficult to fit. The magnetic field density in the air gap is also often very high ($> 0.7\,\mathrm{T}$), saturating most small-scale measuring devices. As such, using the radial or tangential leakage flux for position and speed estimation purposes is not favorable.

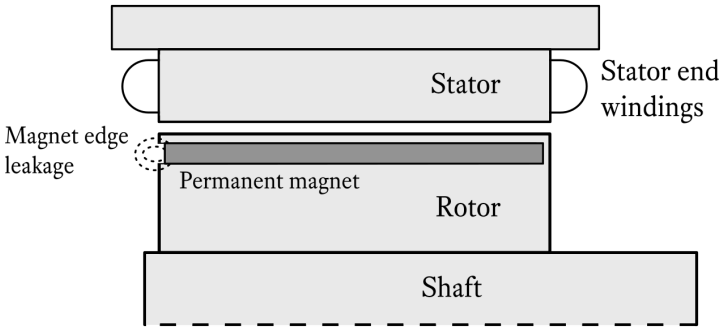

Figure 2.7. A cross-sectional side view of an IPMSM showing the location of the magnet edge leakage flux.

The stray flux from the magnet edge, on the other hand, reaches outwards from the machine and a sensor could be mounted on the flux path. The location of magnet edge leakage is shown in Figure 2.7. Using this edge leakage brings its own challenges. Since a magnet in an IPMSM has been polarized to the radial direction, its axial flux has considerably smaller magnitude, weakening quickly as the distance from the magnet increases. Futhermore, currents in the stator winding could induce a magnetic field which interferes with the magnet edge flux. Still, using the magnet edge flux is overall more feasible than the radial or tangential leakage flux, and it is thus used also in this study.

2.3 Finite element analysis

An analytical magnetic circuit for an electric motor provides a fast evaluation of the motor performance in steady-state. Still, the magnetic circuit is accurate only for motors which have a completely known structure. For new motor designs a finite element method (FEM) is often used. A FEM software can take into account for example nonlinearities in the used materials and complicated physical geometries. A FEM model of an IPMSM is therefore briefly discussed.

The flux distribution of a radial flux PMSM is presented in Figure 2.8. The simulation model had been constructed with the commercial FEM analysis software Flux 2D^{TM} by Cedrat. It shows the flux lines, each contour line representing a path where the flux value stays constant. Every PM has an opposite polarity compared to the adjacent one, represented by blue and yel-

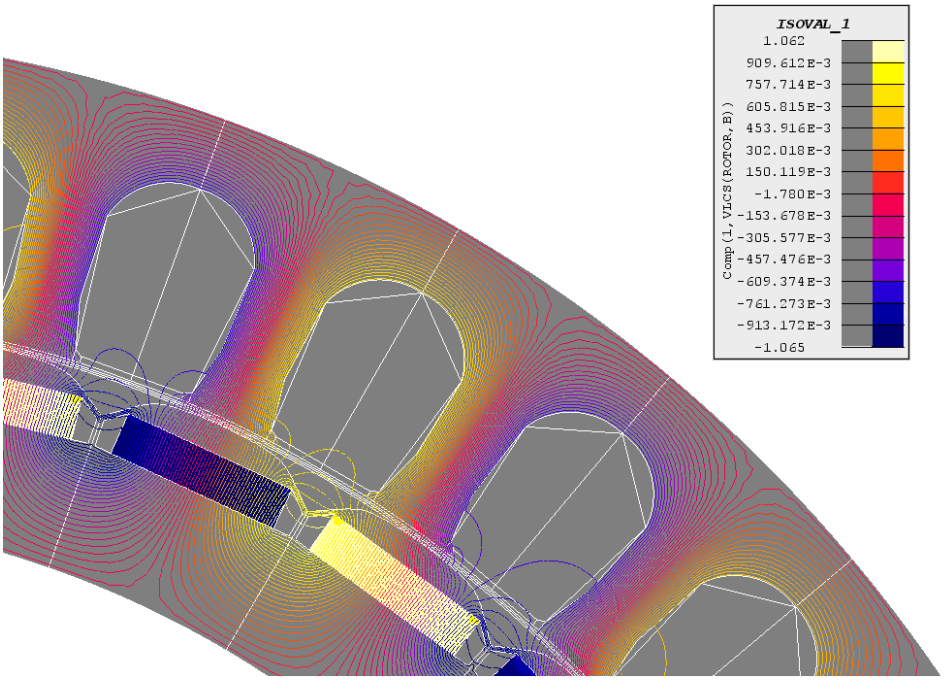

Figure 2.8. A 2D finite element analysis on a radial flux IPMSM.

low colors. Between adjacent magnets flux barriers and iron bridges have been designed. The bridges are needed to ensure the mechanical integrity of the rotor. The flux barriers are effective in preventing magnet-end leakage in the radial and tangential direction, since there is a large reluctance in the flux path. Some flux lines can be seen crossing the air gap between magnets. Other flux lines from the rotor are not linked to the stator, resulting in leakage. Despite some leakage flux, a large majority of the flux lines takes the desired flux path and crosses the air gap.

A 2D model of an axial flux machine is used to determine the strength of the magnet edge leakage flux. Although the construction does not match the radial flux machines used in this thesis, the magnet strength and produced flux density around the magnet are comparable. The result is presented in Figure 2.9. The simulation shows that the magnetic flux density reduces rapidly as the distance from the magnet increases. However, sufficiently close to the magnet the flux density is at easily measurable level. For instance, measured at a distance of 5 mm from the magnet edge, the flux density is still 100 mT. Measured at 15 mm from the magnet the flux density has dropped to 10 mT. A suitable magnetometer can easily detect a magnetic flux density at this level. Various means of measuring the flux are discussed in the next section.

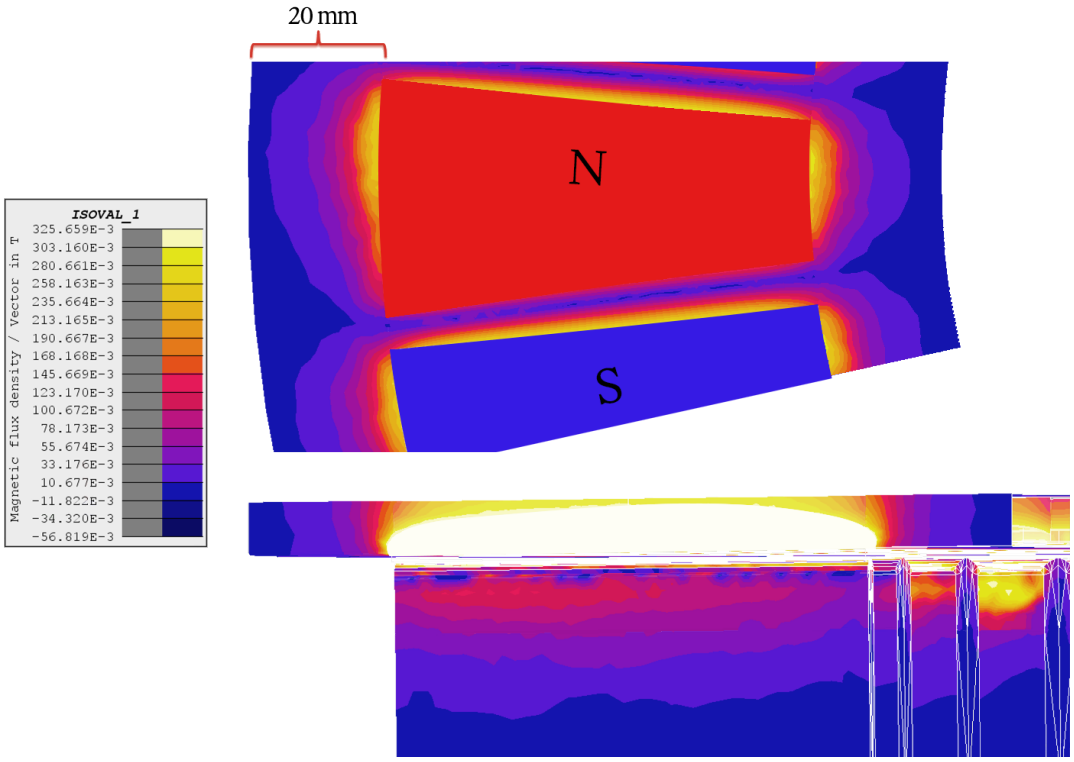

Figure 2.9. Magnet edge leakage flux in an axial flux machine. Front and top view.

2.4 Measuring the magnetic flux

Magnetic sensors can sense the position, velocity or directional movement of magnetic fields. Most sensors need little maintenance and can operate in harsh conditions with heavy vibration and high levels of dust and moisture. Sensing is performed without direct contact to the measurement target, which is beneficial if the target is moving. Magnetic sensors are available for a wide selection of applications and resolutions, ranging from nanoteslas to several teslas. Three types of magnetometers which are selected as most suitable for measuring a flux produced by PMs are presented in this section.

2.4.1 Hall probe

The Hall effect sensor is a very commonly used magnetic sensor. They output a so-called Hall voltage when the magnetic flux density around the sensor exceeds a certain threshold. The core of the sensor is a thin, rectangular shaped p-type semiconductor material like gallium arsenine

(GaAs), indium antimonide (InSb) or indium arsenine (InAs). A current is passed through the material, and it is placed perpendicularly to an external magnetic field, which deflects charge-carriers in the current to opposite sides of the material. One side is filled with electrons and the other with holes, meaning that a potential difference is produced across the material. This deflection is due to the Hall effect, which is a direct consequence from the Lorentz force. The produced Hall voltage is directly proportional to the strength of the magnetic field being measured. However, this voltage is usually very small, in the range of microvolts even in strong magnetic fields. In order to use the voltage as a reliable output, the Hall voltage needs to be amplified and regulated by external electronics. In advanced sensors digital signal processing is also used. In this way the sensitivity, hysteresis and output voltage of the sensor are improved, and it can detect a wider range of magnetic field strengths. The output grows linearly until it reaches saturation.

Many Hall effect sensors are also used as switches. In those cases the sensor is manufactured to have some preset threshold value for the magnetic field density. The output has only two possible values, ”on” and ”off”, depending on whether the measured field is above or below the threshold. Using this kind of output, any oscillation which happens as the sensor is about to enter or exit a magnetic field can be eliminated. To differentiate the sensors from linear Hall sensors, these variants are called discrete Hall sensors.

A common use for a Hall probe is position sensing. When a PM is attached to a moving shaft, a Hall probe can be used to track its movement. Hall effect sensors can also be used as proximity or current sensors, especially if the environment prevents the use of other sensor types. A disadvantage of a Hall effect sensor is that its accuracy is much lower than fluxgate magnetometers or magnetoresistor sensors.

2.4.2 Magnetoresistor

A magnetoresistor is a variable resistor that changes resistance when an external magnetic field is applied. This effect is called the magnetoresistive effect. The resistor is made of semiconductor material, which allows charge carriers to change their direction in the presence of an external field. As a consequence, when a field is being applied, the charge carriers travel a longer distance inside the semiconductor, and more energy is released in the form of heat. Only a small number of charge carriers take a straight route through the material, so the resistance of the material increases. The increase is linearly proportional to the external field density and its

direction.

Magnetoresistors share many of the same advantages as other magnetic sensors; they have a high sensitivity, good resistance to harsh conditions and they are capable of contactless measurement. In alternating magnetic fields, they can operate in wide frequency ranges with good reliability. However, they can suffer from temperature drift over time and very strong magnetic fields can damage the sensor permanently. Also the linear range of the measurement is quite limited.

2.4.3 Fluxgate Magnetometer

A fluxgate sensor uses highly permeable material which is wrapped inside two coil windings called the drive winding and the sensing winding. The arrangement of the material can be linear or circular depending on the shape of the sensor. By driving the first coil with an electrical current, the core is magnetically saturated in opposing directions. In linear-shaped sensor these directions can be produced by two rods of magnetic material wound in opposite directions, and in a circular shape by two halves of a magnetic circle. The axis determined by the two halves is then positioned in parallel to an external magnetic field, as in Figure 2.10.

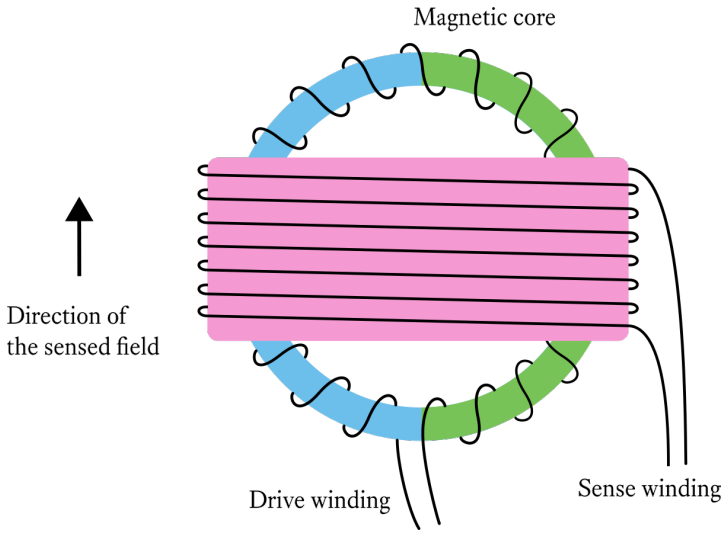

Figure 2.10. A circle-shaped fluxgate sensor.

If an alternating current is applied to the windings, the magnetic core will be periodically saturated and inversely saturated. The changing magnetic field will induce a current to the sensing

coil. If there is no external field, the two fields generated by the two halves of the magnetic material perfectly cancel each other out, and there is no voltage induced to the second coil. In an external field, the core is more easily saturated in alignment with the field and more difficult to saturate in opposition to the field. This means that the external field makes the core come out of saturation later when it is in alignment and earlier when it is in opposition. During the transition there is a net change in the flux in the sense winding, which induces a voltage. The change happens two times per transition in the drive winding, one with a rising edge and one with a falling edge. Therefore the frequency in the sense winding is twice the drive coil frequency. The related waveforms are shown in Figure 2.11. By measuring the phase and magnitude of these voltage spikes, the magnitude and direction of an external field can be calculated. (Imperial College London, 2008)

The affordability, compact size and low power consumption makes the fluxgate sensors popular in a wide variety of applications. By combining three different sensors along three perpendicular axes, a three-dimensional field can be measured. A fluxgate magnetometer is often selected when an extremely high resolution is needed. In practice, the resolution is limited by external noises induced to the coils.

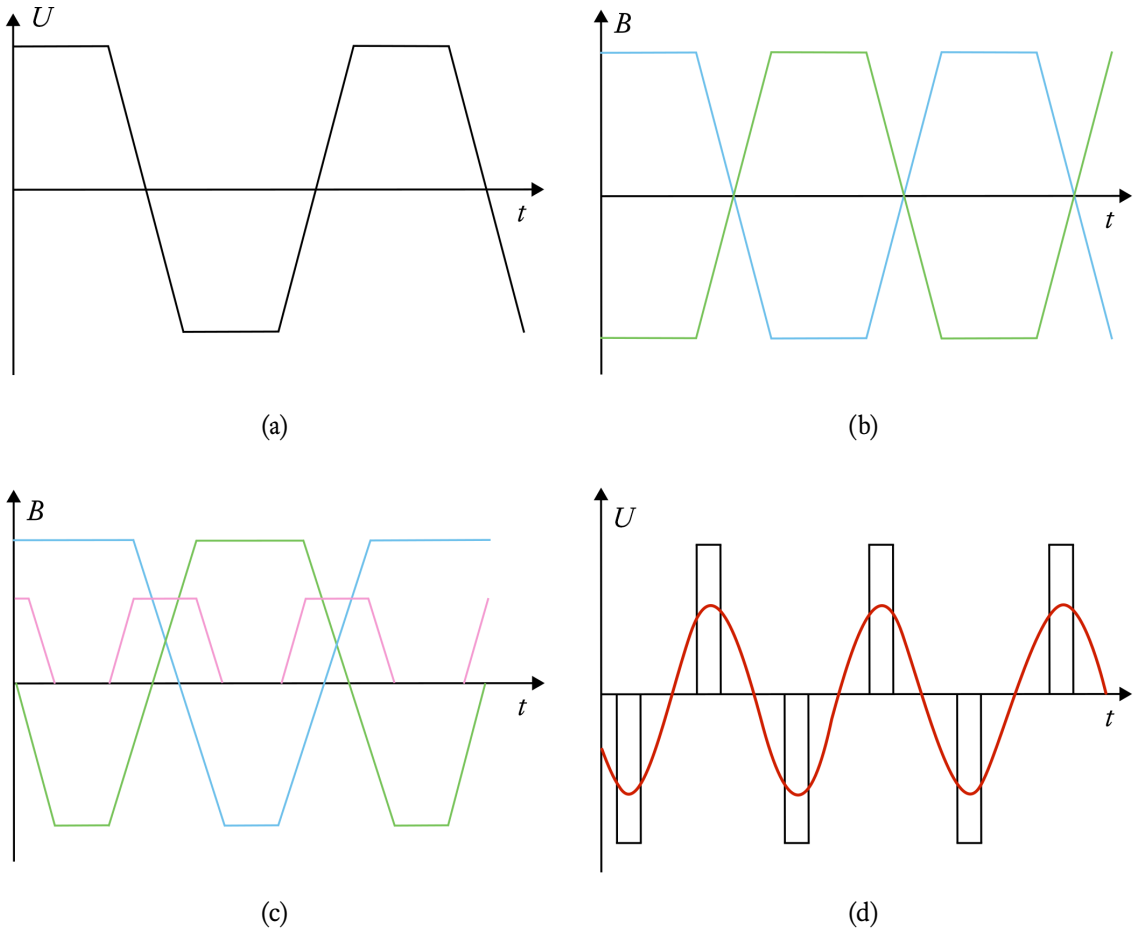

Figure 2.11. Waveforms in a fluxgate magnetometer. (a) The voltage fed to the drive winding. Here the slopes are exaggerated, in reality the waveform is more square. (b) Magnetic fields generated by the two half cores when no external field is present. The fields cancel each other out. (c) Magnetic fields when an external field is present. The half core that is generating a field to the opposite direction of the external field comes out of saturation sooner. It also reaches opposite saturation sooner at the end of the transition. As a consequence there is a net change in the flux (pink). (d) Changing flux induces a voltage to the sense winding. The voltage spikes appear at twice the frequency of the drive voltage. A capacitor can be used to make the output easier to detect (red). (Imperial College London, 2008)

Chapter 3

PMSM control

An elevator can be considered as a system with high requirements for speed and positional control. A sophisticated control is needed to achieve a ride experience that is fast, smooth, safe and accurate. The focus of this chapter is on the different methods of controlling a PMSM. In addition to a more general approach, speed and position control is discussed from an elevator system's perspective. Similarly to the previous chapter, measurement devices used in a real application are also introduced. Some performance requirements for existing speed detection systems specifically in elevator use are presented.

3.1 Speed and position feedback for PMSMs

The control methods of a PMSM are somewhat different from other machine types. The magnetic circuit of a PMSM differs from other machines since the PMs are part of it, significantly influencing the reluctance in the flux path. The relative permeability μ_r of the magnet material is close to one and similar to air, which makes the effective d-axis air gap very long. The d- and q-axis inductances are usually quite small compared to other machine types.

The PMs in a rotor can be arranged in many different configurations, as was shown in Figure 2.1, strongly affecting the magnetic circuit. Therefore designing a general control algorithm for PMSMs is difficult. As their name implies, they are synchronous machines by nature. As a consequence, the torque in PMSMs can only be predicted when the AC excitation current frequency is synchronized with the rotor rotation. This requirement is the fundamental princi-

ple of all control systems designed for synchronous machines. By implementing a continuous measurement of the absolute rotor angular position and feeding it to a controller, the machine currents can be controlled correctly. A direct measurement, also called *self-synchronization*, ensures that the machine does not go out of synchronism during operation. Figure 3.1 illustrates this concept.

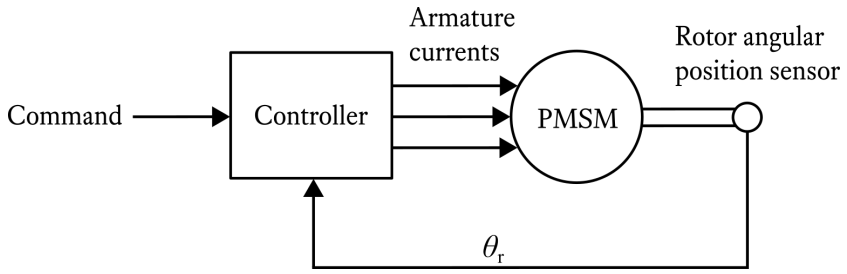

Figure 3.1. Simplified control scheme of a PMSM.(Perera, 2003)

In the figure it can be seen that the control uses a closed-loop system. In a closed-loop, feedback from the rotor position is fed back to the controller, improving performance. In addition to velocity control, the rotor angular position information can also be used in torque control. Torque production in PMSMs is a function of the stator currents, and the torque controller uses feedback information both from the stator currents as well as the rotor angular position. Speed control can be incorporated to the same structure outside the torque control loop, as shown in Figure 3.2. Both controllers can use the signal from the same rotor position sensor. (Perera, 2003)

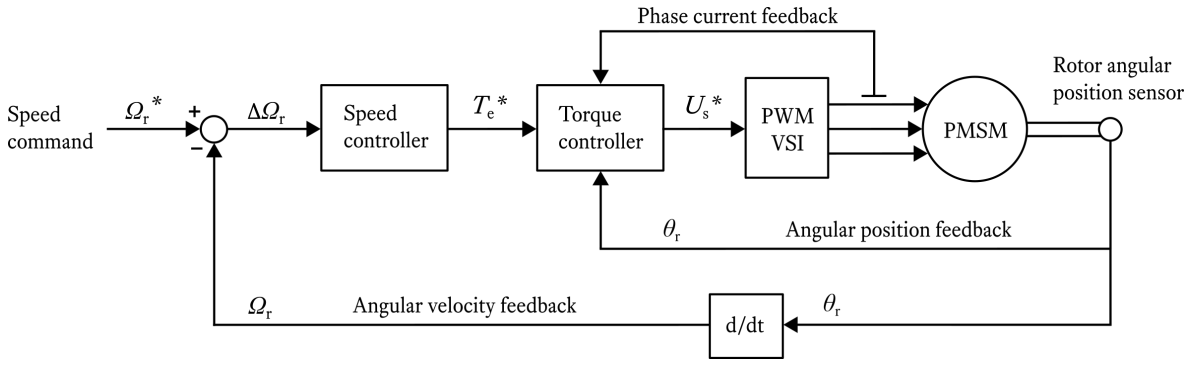

Figure 3.2. Control of a PMSM with speed and torque controllers.(Perera, 2003)

The basis for many PMSM control schemes is the torque equation. According to the cross-field principle, it can be expressed as

$$T_{\mathrm{e}} = \frac{3}{2}p[\,\Psi_{\mathrm{PM}} i_{\mathrm{q}} - (L_{\mathrm{mq}} - L_{\mathrm{md}}) i_{\mathrm{d}} i_{\mathrm{q}} + L_{\mathrm{md}} i_{\mathrm{D}} i_{\mathrm{q}} + L_{\mathrm{mq}} i_{\mathrm{Q}} i_{\mathrm{d}}], \tag{3.1}$$

where p is the number of pole pairs, Ψ_{PM} is the magnetic flux linkage produced by the PMs, i_{d} and i_{q} are the d- and q-axis currents, L_{md} and L_{mq} are the d- and q-axis magnetizing inductances, and i_{D} and i_{Q} are the damper winding currents. The torque consists of four different components. The fist component, $3p/2(\,\Psi_{\mathrm{PM}} i_{\mathrm{q}})$ is the most significant, and in many machine types the only torque producing component. The second term, $3p/2(L_{\mathrm{mq}} - L_{\mathrm{md}}) i_{\mathrm{d}} i_{\mathrm{q}}$, is prominent in machines with a large inductance difference between the d- and q-axis inductances. The last two components of the equation are related to damper currents, and are only remarkable during transients and in machines with clear rotor conductivity (e.g. damper windings).

3.1.1 Vector control of a PMSM

Current vector control is a widely used control principle for PMSMs. To produce torque, the magnetic fields produced be the stator and rotor must be kept in correct positions relative to each other. This can be done using vector control algorithms. In many PM machines, the electrical characteristics, like inductances, do not vary significantly during operation, and a current vector–based approach works well. A block diagram of current vector control is presented in Figure 3.3.

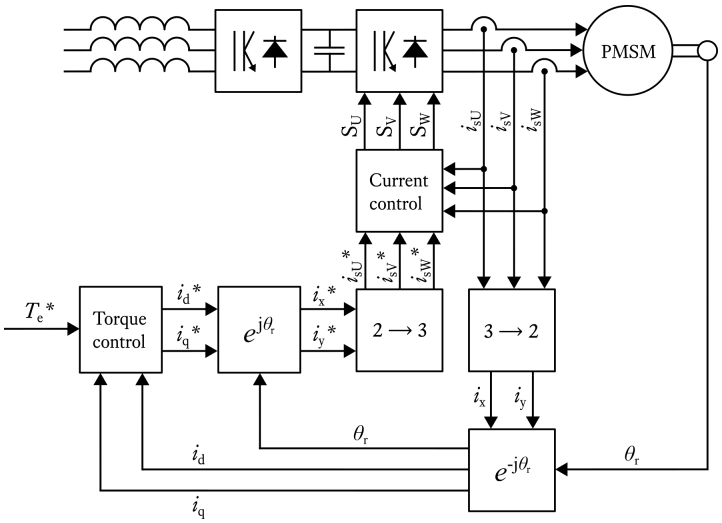

Figure 3.3. Current vector control of a PMSM.(Pyrhönen et al., 2016)

As seen in the figure, measured stator currents and rotor angle are used as a feedback loop, going through blocks that transform them to a coordinate system rotating with the rotor. This transformation to the rotor reference frame is beneficial since it greatly simplifies the equations needed in the control algorithm. A torque reference is fed to the torque controller, which calculates reference values for d- and q-axis currents. The method for the calculation is dependent on the configuration of the magnets in the rotor and the drive system. The figure also shows an implementation of regenerative braking, which feeds power back to the network in braking situations. During past years, the efficiency of elevator drives has partly improved by using regenerative braking.

The motivations behind the reference frame transformations are simple calculations and a fast processing time. For simplicity, let us consider a three-phase AC machine with a two-pole PM rotor. The control scheme introduced here is also valid for machines with more poles after the calculated angle values have been scaled according to the number of pole pairs. Two stator currents of the AC machine are measured directly and the third can be calculated from a vector sum of the first two. The currents flowing through each of the windings create a magnetic field at a specific angle, described by field vectors. In a three-phase machine, the stator windings are assembled so that these field vectors are distributed 120 degrees from each other, one vector per phase. The three-phase vectors produce one net stator field vector that rotates as a function these field vectors.

In order to produce torque, the magnetic field produced by the stator currents and rotor PMs needs to be perpendicular to the current vector produced by the rotor. To keep them perpendicular, the rotor position needs to be known. In most cases, the rotor angle is determined from an angle sensor, such as an encoder or a resolver, but also sensorless methods have been developed. By convention, this rotor angle is usually defined as the angle between the direct axis and the magnetic axis produced by one of the phase currents.

To understand the effect of different phase currents on the motor performance, the currents should be transferred to the dq-reference frame rotating with the rotor. In field-oriented terminology that is also called the Forward Park transform. To simplify the equations further, it is advisable to convert the three phase currents to two orthogonal current vectors before doing the Forward Park transform. The two new current vectors need to produce the same net current vector as the original currents. This process is also called the Forward Clark transformation, described in

$$
\begin{aligned}
i_{\mathrm{x}} &= \frac{3}{2} i_{\mathrm{sU}} \\
i_{\mathrm{y}} &= \frac{\sqrt{3}}{2} i_{\mathrm{sV}} - \frac{\sqrt{3}}{2} i_{\mathrm{sW}}.
\end{aligned}
\tag{3.2}
$$

The transformation to the rotor reference frame can now be done with the orthogonal stator currents and the rotor angle θ_{r}:

$$
\begin{aligned}
i_{\mathrm{d}} &= i_{\mathrm{x}} \cos\theta_{\mathrm{r}} + i_{\mathrm{y}} \sin\theta_{\mathrm{r}} \\
i_{\mathrm{q}} &= -i_{\mathrm{x}} \sin\theta_{\mathrm{r}} + i_{\mathrm{y}} \cos\theta_{\mathrm{r}}.
\end{aligned}
\tag{3.3}
$$

The result of the transformation is two current vector components: i_{d} is directly aligned with the rotor flux on the d-axis, and i_{q} is perpendicular to the rotor flux on the quadrature axis, see Figure 3.4. The sinusoidal currents have been transformed to DC-quantities, which are much easier to handle in the control. A controller is making adjustments directly to i_{d} and i_{q} by minimizing the error between the current values of i_{d} and i_{q} and their the desired values, resulting in reference values i_{d}^* and i_{q}^*. For example in $i_{\mathrm{d}} = 0$ control scheme, the i_{d} current is kept is at zero, since the PMs already produce flux on the d-axis. An independent controller could be implemented for both the d- and q-axis.

Now that the current references have been calculated, they need to be applied to the stator windings. This is done by executing the previous transformations backwards. First, the currents are transformed to the stator reference frame by the Reverse Park transform:

$$
\begin{aligned}
i_{\mathrm{x}}^* &= i_{\mathrm{d}}^* \cos\theta_{\mathrm{r}} - i_{\mathrm{q}}^* \sin\theta_{\mathrm{r}} \\
i_{\mathrm{y}}^* &= i_{\mathrm{d}}^* \sin\theta_{\mathrm{r}} + i_{\mathrm{q}}^* \cos\theta_{\mathrm{r}}.
\end{aligned}
\tag{3.4}
$$

The result is two stator reference currents i_{x}^* and i_{y}^* which, when added to the stator currents, yield the same effect as adding i_{d}^* and i_{q}^*. Note that the rotor angle θ_{r} is needed again to perform

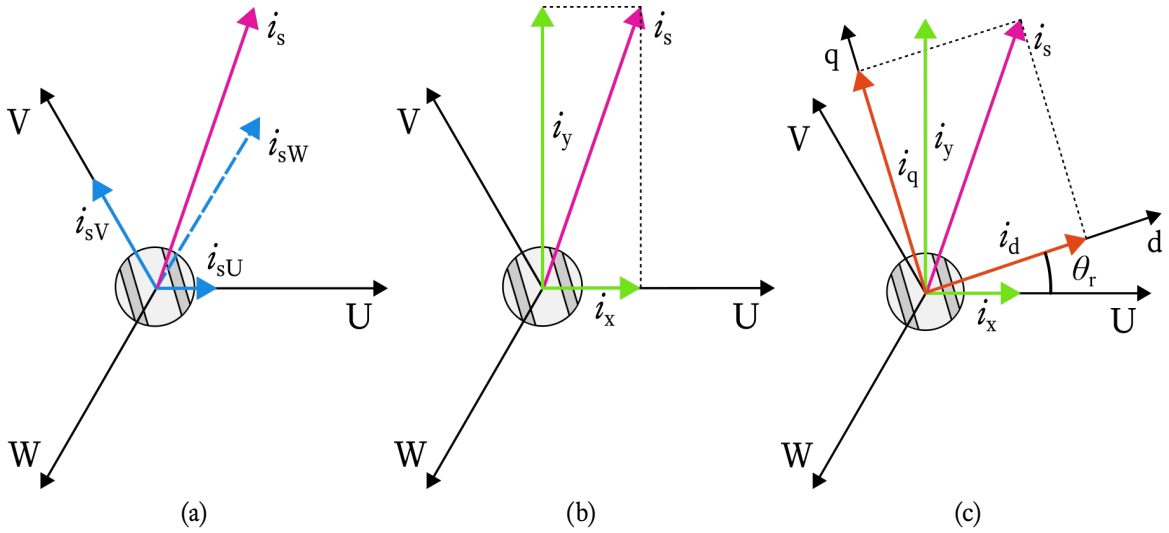

Figure 3.4. Field-oriented control of a PMSM. U, V and W create the stator reference frame. An embedded magnet rotor is illustrated in the background. (a) Two stator currents i_{sU} and i_{sV} are measured, and i_{sW} can be calculated since the currents equal to zero. i_s is calculated as an arithmetic sum of the phase currents. (b) Transformation from three-phase currents to two-phase currents i_x and i_y. (c) Transformation to the rotor reference frame (d- and q-axis). Currents i_d and i_q create the same stator current as i_x and i_y. The rotor angle θ_r is also marked.

the transformation. The final step of the process is to apply the Reverse Clark transform:

$$\begin{aligned} i^*_{sU} &= \frac{2}{3} i^*_x \\ i^*_{sV} &= \frac{1}{3} i^*_x + \frac{1}{\sqrt{3}} i^*_y \\ i^*_{sW} &= -\frac{1}{3} i^*_x - \frac{1}{\sqrt{3}} i^*_y. \end{aligned} \tag{3.5}$$

The resulting currents can now be applied to the stator windings by using a current controller, which adjusts switching function variables S_U, S_V and S_W by comparing the measured three-phase currents and calculated current references.

The whole process should be repeated with a sufficient frequency. If the time between two current samples is too long the field-oriented control will run poorly. One way to increase the frequency is to make use of the introduced transformations to make the equations needed in vector control as simple as possible so they contain only a few additions, multiplications and look-up table fetches (trigonometric calculations). With modern power electronics the sampling frequency can be in the range of 20 kHz, resulting in smooth field-oriented control.

3.1.2 PMSM control schemes

In salient-pole machine control both of the current references produced by the torque controller are non-zero. In contrast, for nonsalient-pole machines like rotor surface magnet machines, the d-axis current reference is usually kept at zero in cases when the field weakening range is not needed. In this so-called $i_{\mathrm{d}} = 0$ control, the q-axis current is used to produce torque and the d-axis current is used to control magnetization. It works well with machines that have d-and q-axis inductances approximately equal. It also provides the best possible energy efficiency. In order to achieve smooth operation, the rotor angle must be known real time. (Pyrhönen et al., 2016)

As seen in Equation (3.1), if a machine has a high inductance difference between L_{mq} and L_{md}, it produces reluctance torque that must be taken into account. The best control method in this case is the maximum torque per ampere (MTPA) control. When rotating speeds higher than the nominal speed of a machine are required, field weakening control and maximum torque per volt (MTPV) control can also be considered. However, for a PMSM, operating in the field weakening range can be problematic, since the back-emf of the machine is proportional to the speed of the machine. The frequency converter driving the machine must be able to withstand this back-emf, because in case a demagnetizing current on the d-axis is lost, the whole back-emf will be fed to the converter. Usually the components which dictate the overvoltage limit of the frequency converter are the DC link capacitors. Therefore if a machine is designed to operate partly in the field weakening, the capacitors of the frequency transformer should be chosen accordingly. (Pyrhönen et al., 2016)

3.1.3 Sensorless position estimation

A number of sensorless control methods eliminating the need for angular position sensors have been developed. The rotor position is estimated on-line using an estimator algorithm which calculates the position and angular speed of the rotor. Sensorless estimation can be categorized into three main groups: model based estimators, signal injection estimators and soft computing estimators.

Model based methods use a mathematical model of the machine and measurements of electrical quantities, like the stator currents, to determine the rotor position and speed. The control system can be based on an observer, flux linkage estimation or back-emf estimation. An ob-

server constructs the states of the system which can not be measured directly from the accessible states. For back-emf and flux linkage estimators a voltage model of a PMSM is needed. All model based methods are hindered by the fact that they need back-emf to track the rotor position. At standstill, the back-emf is zero, so the rotor position is unknown. In practice it is also problematic to use model based methods at low speeds since in that case the back-emf has a poor signal-to-noise ratio and the possibility for estimation errors increases.

To overcome these problems at low speeds, signal injection methods have been extensively developed. In signal injection, a high frequency voltage or current signal is injected into the motor, resulting in an output signal that can be used to determine rotor position and angle. The injection signal is usually added to the sinusoidal voltage reference signals of the machine. This way, the injection can be continuous and does not interfere with normal modulation operations. High frequency injection methods are based on the saliency of the motor and thus cannot correctly estimate machines with low saliency. A separate low frequency signal injection method can be used if the saliency ratio is close to unity. This method creates mechanical vibrations to the rotor if the position is not correctly estimated. The drawbacks of low frequency injection are slow responses in transient situations and poor performance with machines that have a high inertia.

The third group in sensorless estimation, soft computing, uses neural networks, fuzzy logic and genetic algorithms in rotor speed and position estimation. Neural networks can be trained with a training data set in order to learn the characteristics of a particular machine. The inputs for a neural network are for example the measured machine currents and voltages, and the outputs are the rotor position and speed. Neural networks are also capable of on-line operations. While effective, these soft computing methods are often complex by nature. (Eskola, 2006)

3.2 Position and velocity feedback devices

In a previous section, Figures 3.1, 3.2 and 3.3 showed that an angular position sensor is needed for most control methods used for PMSMs. In this section, different types of angular position sensors are described.

3.2.1 Incremental encoder

An encoder translates linear or rotary displacement to digital signals. Rotary encoders are used specifically to track the rotation of a motor shaft. There are two main categories of rotary encoders: incremental encoders and absolute encoders.

Incremental encoders get their name from their output, which detects a certain increment of rotation, sensing only the motion of the shaft, but not its angle. A disc inside the encoder has opaque and transparent sectors that divide its circumference into small sections. Light is passed through the slots and then detected with a light sensitive photosensor. As the disc rotates, light is interrupted by the opaque parts of the disc, which creates an alternating light-dark pattern on the photosensor, generating a digital square-wave signal. Decoding circuitry and a digital processor are then used to count the signal, each count corresponding to one state-change in the signal. Similarly, the frequency of the state-changes corresponds to the rotation speed of the disc. This kind of optical encoder is the most popular type of angular position tracking device. An optical encoder by Leine & Linde is illustrated in Figure 3.5.

Figure 3.5. An optical encoder by Leine & Linde. The housing of the encoder needs to be carefully sealed, since the photosensor is very susceptible to dust.

The resolution of an encoder is defined as counts per turn, referring to the number of slots on the disc. Often two separate slot rows are manufactured on the disc, accompanied by an additional light source and photosensor pair. A convex lens can be used to focus the light into two parallel beams. The second slot row is positioned to have a 90 degree phase shift compared to the first row, so the second square wave signal is also 90 degrees out of phase. This way, in

addition to speed, the encoder can also detect the direction of rotation by determining which signal is leading the other. Adding a second row also has other important benefit; the resolution of the encoder increases due to increase in edge translations in the signals.

The information obtained from the slots is fed to a processor that calculates the number of pulses, followed by the rotor speed and direction. Sometimes an additional row is added to the disc with only one slot. The signal generated by the slot is used to determine a zero position. Each time the encored is powered off, it begins counting from zero, so initial homing to a reference or zero angle is needed in all positioning tasks that need the absolute angle value.

A more advanced version of the two-row encoder is a differential encoder, which also produces inverse signals of both the original square waves. Comparing the inverse signals to the original signals, transmission errors can be effectively minimized, since every angle increment produces two state-changes independent from each other. (Eitel, 2014)

3.2.2 Absolute encoder

An absolute encoder has the ability to sense the absolute position of its shaft. It takes advantage of the same principles of producing signals via photodetectors as an incremental encoder, but the internal construction is more complex. Each slot row on the disc has its own light source and detector. The disc also has a special structure: the slots on it form an individual code for each detectable position of the disc. Therefore, the absolute angle value is immediately available after the encoder has been turned on and the first edge transition has been detected. Counting the angle increments is not necessary. Furthermore, an absolute encoder does not need homing or zero position for calibration, since it can start measuring immediately after start-up. The increased functionality compared to incremental encoders comes naturally with more manufacturing challenges and an extra cost.

The slots of an absolute encoder disc are laid out according to Gray code instead of normally incrementing binary numbers. Inevitable manufacturing errors in the slot widths cause the individual signals to switch at slightly different moment in time. This results in momentary combinations of signals that do not correspond to the correct angle value. If the encoder reads a value incorrectly in standard binary, the position of the disc is impossible to be determined. In Gray code, every successive value differs by only one bit from the previous value. This way the errors between two correct values are minimized. The number of Gray code values defines

the resolution of a specific encoder. An absolute encoder using Gray code is shown in Figure 3.6.

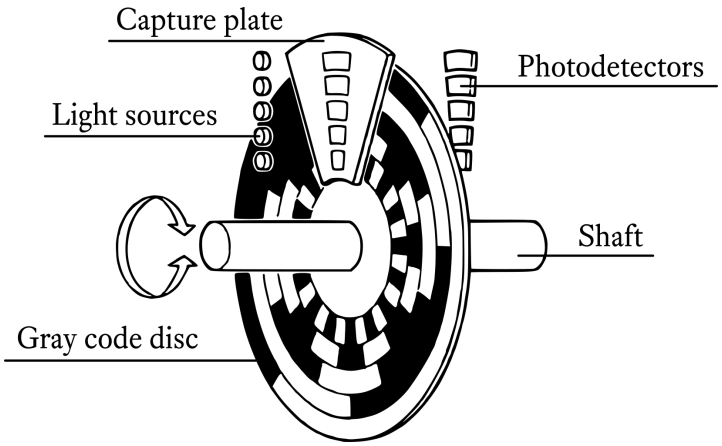

Figure 3.6. An absolute encoder with a Gray coded disc.

In addition to tracking an angle within a whole turn, absolute encoders can also track the number of whole turns. This is achieved by adding more coded discs to the encoder and connecting them with gears. The encoder electronics can then calculate the total number of turns by combining information from all the discs. The construction of this type of encoder is obviously quite complex.

The resolution and accuracy of an encoder should not be mixed. As mentioned previously, in an absolute encoder the resolution equals to the amount of different values produced by one revolution. Accuracy is defined by the number of the slots, the quality of their manufacturing and the stability of the encoder's mechanical installation. If there are too many slots on the disc, light passing through a single line can be too weak for the photodetector. Many thin slots too close to each other can also produce fringing and destructive or constructive interference, which can in turn affect other detectors and introduce crosstalk in the system.

In certain models the signal produced by the encoder is a sine wave rather than a square wave. This type of an encoder is called a sine or sinusoidal encoder. By processing the signal in a controller, additional position information can be obtained by interpolation. Strictly speaking this does not increase the encoder resolution since the values in between pulses are not exactly known positions. However, interpolation has been shown to produce reliable results as long as the interpolation factor is not too high. If too high resolutions or interpolation factors are used, the precision suffers due to possible misinterpretations and errors. Therefore it is important to set a limit for the interpolation circuitry to ensure error-free operation. A typical interpolation

resolution is 256 to 1024 position values per one sine wave. With 512 to 2048 sine cycles per revolution, an encoder might have a resolution in order of millions of pulses per revolution.

Even though the resolution of an interpolated encoder is superior to a non-interpolated one, if the application needs a high accuracy, it might be more beneficial to use a low resolution encoder with some interpolation rather than a device with a very high resolution. For high resolution encoders the mechanical and optical setup requirements are often very demanding. Poor environmental conditions can dramatically affect the accuracy of the signal. By using moderately interpolated encoders one can achieve a good balance between the signal quality and robustness of the assembly. (Hohner Automáticos, 2015)

In a rotary encoder, very low speeds cause long delays between state-changes in the measured signal. At start-up, since the distance between the light beams producing the output signal and the first slot edge is not known, the first state-change is not enough to determine reliable speed information. It can be done only after a second state-change is detected, which might take a long time from the perspective of the control system. Therefore using a rotary encoder can cause problems if the speed information is needed immediately after start-up from zero speed.

3.2.3 Resolver

A resolver is an analog angle and velocity feedback device. It has two separate cylindrical parts, a rotor and a stator. There are several windings: a reference winding in the rotor coupled with so-called sine and cosine windings in the stator. In operation, an AC signal is fed to the reference winding in the rotor through a rotary transformer. A signal is then induced in the sine and cosine windings through electrical coupling. The sine and cosine windings are constructed so that they have a sinusoidal variation around the resolver's circumference by changing the density of the wire turns that make up the winding. The two windings are placed 90 electrical degrees with respect to one another, hence the names sine and cosine.

When the angular position of the rotor is varied, the magnitudes of the voltages in the two other coils represent sine and cosine of any angular position. Therefore, by taking the arctangent function of the two voltages in the output windings, the angle of the rotor can be determined. In other words, there is a distinct pattern of outputs for every position of the rotor.

Two-pole resolvers have two magnetic poles, so their output is one complete sine wave and

one cosine wave over one mechanical rotation. A resolver can also have multipole capabilities, so that one mechanical rotation produces multiple sine and cosine cycles. Both of these approaches have their own benefits. A two-pole resolver provides absolute position feedback, but it may suffer from mechanical variations over time, decreasing accuracy. A multipole resolver has a better accuracy. For example a six-pole resolver has an output where a mechanical turn of 120 degrees produces one sine/cosine wave. The accuracy increases with the number of poles, and a multipole resolver might have as many as 32 poles, although a high number of poles means increased complexity and a higher cost. One approach is to combine the characteristics of two- and multipole resolvers into one device by incorporating them into a single package. Both an absolute position sensing capability and a high accuracy can then be realized in one device.

As an analogue device, a resolver can be thought to have infinite theoretical resolution, limited only by the voltage measurement capabilities. Due to its simple design and lack of electronics it can operate in harsh environments, where for example a rotary encoder would suffer from dirt and dust covering the photodetector. However, because a resolver is essentially an angle sensor, using it as a speed sensor might prove difficult. A frequency converter using a resolver as a feedback sensor would also need additional electronics to feed and measure the resolver. (Prentice, 2018)

3.2.4 Tachometer

One way to measure the rotational speed of a shaft is to use a tachometer. It acts as a DC generator by rotating a rotor in a magnetic field produced by PMs. The rotating motion generates an electromotive force that is measured with a voltmeter. Since the generated magnetic field is constant, the voltage depends only on speed. A tachometer can be of AC or DC type. In DC type, commutator and brushes must be used. An AC type tachometer uses a rectifier to turn the generated AC voltage into DC, so commutation is not needed. The output is also often filtered through a capacitor to reduce ripple.(Rajput, 2009)

Tachometers are designed so that they produce a voltage that changes very linearly as a function of speed in their operational area. The output also has a low phase lag. In spite of these advantages, tachometers are disappearing from modern high-performance control systems due to their numerous shortcomings. Most prominent of those is simply a high cost. Furthermore, because of their fundamental structure it is impossible to use them as position sensors.

This means that most control systems would need to use an another sensor in addition to a tachometer. DC tachometers also need periodic maintenance as their carbon brushes need to be replaced. In a very low-speed application a tachometer can be a good choice, since similarly to a resolver, as an analog device it has no theoretical resolution limits. Therefore it can produce a reliable and high-quality signal at low speeds. In broader range of applications, many control systems take advantage of both position and velocity feedback, and as a consequence tachometers have become increasingly uncommon. (Ellis, 2002)

3.3 Speed calculation in an elevator system

The drive system in an elevator calculates the motor speed from signals given by an angular position sensor, usually an encoder. If *quadrature encoding* (see section 4.2.1) is used, the output produces two signals A and B, possibly together with their inverse signals. Ideally A and B have a 90 degrees phase shift between them. Both signals are sampled at points in time separated by a time interval Δt, which is determined by the sampling frequency. Δt could be for example in the range of one millisecond. The amount of rising and falling edges in the quadrature signal is calculated during every time interval. The mechanical rotor angular speed Ω is then calculated and quantized with

$$\Omega = \frac{\theta}{\Delta t} \approx \frac{\text{pulse count}}{\Delta t}. \tag{3.6}$$

There is an uncertainty in how close the previous and next edge would be to the calculation window. This will result in quantization error in the speed estimate. A speed controller can amplify the error even further, which results in noticeable torque ripple in the motor output.

A resonance frequency in the mechanical system can also cause unwanted vibrations. A quantized signal contains inherently all frequencies, so an external system driven by a quantized signal can easily begin to resonate. Considering the ride comfort of an elevator, this is highly unwanted. The quantization error can be mitigated by measuring the time between the rising edges and the calculation window, as illustrated in Figure 3.7. Equation (3.6) can then be changed to

$$\Omega \approx \frac{\text{pulse count}}{t_1 + \Delta t - t_2}. \tag{3.7}$$

By using this more sophisticated approach, the quantization error can be nearly eliminated, given a high sampling frequency is used.

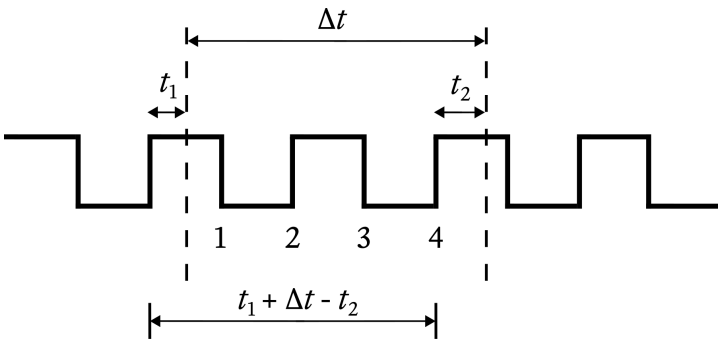

Figure 3.7. Speed calculation from a quadrature signal. Four pulses are taken into each time interval.

With an ideal encoder, the algorithm would produce perfect speed estimates. Unfortunately, in reality also the encoder causes nonidealities to the approximation. A phase shift between the A and B channels is assumed to be always 90 degrees, but in reality it can vary as much as 90±20 degrees. This kind of a large variation will again produce noticeable torque ripple.

Another error source affecting the speed estimate is the variation of the quadrature signal's duty cycle. In an ideal quadrature signal the duty cycle is 50 %, meaning that in average, the signal is in "high" state the same amount of time as in "low" state. To counter duty cycle variations, it is ensured that four pulses are detected in each calculation window before moving on to the next time step. The method is based on the assumption that the rising edges of the A and B signals are not affected by the phase shift or duty cycle variation. In low rotation speeds, waiting for four pulses to arrive in each time step is not feasible, which means that the method is only usable at relatively high speeds.

In addition to speed, the electrical angle of the rotor needs to be calculated from the encoder signals. The angle is used to synchronize the machine during operation. Like errors in speed estimation, also angle estimation errors can result in unwanted behavior. As discussed in section 3.1.2, in $i_\mathrm{d} = 0$ control, i_q is used to produce torque and i_d is used to control magnetization. In case there is an angle error, some of the current that is meant for the q-axis goes to the

d-axis instead, which is harmful for the magnetization and reduces produced torque. Excess current in the negative d-axis can start to demagnetize the machine, further reducing torque. A reduced torque results in a reduced speed, so a speed controller builds up an error signal and requests for more torque. Consequently an even bigger error is produced, and the performance and efficiency of the motor deteriorate quickly as more current is fed to the motor.

If the angle error stays constant, the frequency transformer feeds a constant excess current to the motor, reducing its lifetime. Excess current turns into excess heat, which in turn causes the motor winding insulation to deteriorate quickly. In the worst case, the motor may not be able to follow speed references given by the control system during acceleration, resulting in a fault. In case the angle error fluctuates around the correct angle, it can cause a fluctuating torque component. A fluctuating torque can in turn resonate with the whole mechanical system and additionally be amplified by the speed controller. For these reasons, a constant angle error is more desirable than a constantly fluctuating one. A constant error could be more easily detected and compensated by the control algorithm. Unfortunately, having a constant error is rare since the error often changes depending on the operating point. For example, it will likely increase during acceleration and deceleration. (Jokinen, 2018)

3.3.1 Performance requirements for position feedback

Ride comfort is an important focus point in an elevator industry, and a motor control system together with mechanical installations plays a major role in achieving good ride comfort. The final goal of elevator speed control is to develop a system that results in smooth speed changes. Any fluctuations should be unnoticeable to the passengers. Multiple feedback loops in the control system are usually exploited. PMSMs are widely used in elevator applications since they provide high torque at relatively low angular speeds. Synchronous motors have a flat torque-speed curve up to their maximum output power. Traditional PMSM control methods can only be improved if the rotor position is known with a high accuracy.

In addition to constant speed, special attention is given to the low-speed phases at the beginning of acceleration and at the end of deceleration, as the passengers are especially alert for any disturbances in the system during those times. Coincidentally, in many PMSM control techniques the low-speed operation is the most challenging speed region. During low-speed operation, high resolution of a speed measurement system is the most beneficial. At high speeds, many control systems can operate even without the angular position information. Therefore

the amount of pulses fed to the frequency converter could be decreased as the speed increases. The requirements for a speed measurement system are often demanding. It should have not only a good accuracy at low speeds, but also be able to handle high speeds.

In an elevator system, the accuracy of a position measurement is directly related to the ride comfort. In low-speed region, the position of the car is always derived from the motor, which provides it further to the control system. At start-up, the angle of the rotor is needed for the acceleration of the machine. If the angle is incorrectly estimated, the machine might operate with poor efficiency. If there is a risk of going out of synchronism, the machine might not start at all. A small error in the position estimation would result in a slight unwanted movement of the car at start-up because the needed torque was incorrectly estimated. Usually a small error is acceptable as long as passengers in the car cannot feel it.

To illustrate the concept of speed and position resolution in elevator systems, let us consider a motor which is driven with an incremental encoder attached on its shaft. The resolution of an encoder is given as *pulses per revolution*, or ppr. The unit describes how many state-changes or pulses the encoder outputs during one full rotation. In an elevator with 1-to-1 roping, the elevator car moves at the same speed as the traction sheave of the elevator. If the encoder has for example 16 000 ppr and the traction sheave diameter d_{tr} is 0.5 m, the position of the car has an accuracy of

$$\frac{d_{\mathrm{tr}}\pi}{ppr} = \frac{0.5\,\mathrm{m} \times \pi}{16\,000} \approx 0.098 \times 10^{-3}\,\mathrm{m} \approx 0.10\,\mathrm{mm}. \tag{3.8}$$

Many small elevators use 2:1 roping, which means that the elevator car moves half the speed of the traction sheave, and the accuracy is further halved to 0.05 mm. In an elevator using 1:1 roping, a large traction sheave diameter compensates for the worse accuracy. In modern elevators the floor landing is highly accurate to increase safety and prevent tripping to the doorstep, so the pulse count needs to be relatively high. (Wenlin, 2018)

One design specification for a position feedback system is the allowed calculation time for each angle update. It describes the time that any signal processing circuitry has before it needs to send a new angle update to a control system. One way to formulate a design specification is to tie it to the number of angle updates per one full electrical cycle of the motor. An electrical angle of a machine relates to the mechanical angle as described by

$$\theta_{\mathrm{e}} = p\theta_{\mathrm{mech}}, \tag{3.9}$$

where θ_{e} is the electrical angle, p is the number of pole pairs in the machine and θ_{mech} is the mechanical angle of the rotor. For example, a requirement of two angle updates per one electrical degree might be used. In other words, the control system needs to receive at least 720 angle updates per one electrical cycle. The maximum speed of the motor determines the allowed calculation window for each angle update, which can be calculated with

$$\Delta t = \frac{1}{m \times (n/60) \times p \times 360}, \tag{3.10}$$

where m is the required number of updates per one electrical degree and n is the maximum allowed speed of the machine in revolutions per minute. The requirement for m comes ultimately from the maximum speed that a rotating system is allowed to have.

In summary, the angle measurement device should satisfy two important performance requirements. It should:

- allow highly accurate elevator car positioning by producing enough distinct angle values during one rotation of the motor shaft
- produce angle updates with a frequency that is sufficient for the control system even during maximum speed of the machine

As mentioned previously in this section, the requirements are demanding, therefore limiting the choice of suitable angle measurement systems and often requiring design trade-offs.

Chapter 4

Speed estimation using rotor leakage flux

A disadvantage of most of the control systems mentioned in the previous chapter is the need for an angular position sensor. In general, using a shaft-mounted sensor is not desirable for several reasons. They increase the size of the system and have a need for periodic maintenance. Assembling the sensor on the shaft requires special mechanical structures and electrical wiring. Many high-resolution sensors, despite their high cost, can suffer from measurement drift over time or accuracy deterioration in high temperatures. Despite these shortcomings, especially encoders are still widely used because of their superior resolution.

The previous chapter also described several sensorless control methods that aim to get rid of the need for angle measurement. While effective, they also have some disadvantages. A model based method cannot operate at low speeds because it needs a measurable back-emf for the speed estimation. Signal injection methods have been shown to perform well at low speed range, but they work only with machines that have q- and d-axis inductance differences. Although saliency is needed, higher harmonics caused by the saliency can produce periodical estimation errors. Load-dependent estimation errors have also been reported. Finally, signal injection can cause acoustic noise, which is especially unwanted in elevator motors. Any noises generated by the motor are likely to be amplified by the elevator system.

Sensorless methods related to soft computing have shown promising results. However, tuning and optimal structure selection of a neural network requires profound expertise, since no general rules are available. In fuzzy logic algorithms, parameters must be selected by time-consuming trial and error. Simple estimation algorithms are preferred over more complex ones, even though complex methods might also be more effective. At present, the compu-

tation time needed in soft computing methods is too long for on-line systems. In the future this might change due to the development of integrated circuits. However, the spread of new integrated circuits might take a long time since low-cost components are usually preferred in the industry.

In this chapter, an alternative method for a PMSM speed estimation is introduced. In literature, the basis of the method has been described by (Jung et al., 2010) and further developed by (Jung and Nam, 2011) and (Lee et al., 2017). The leakage flux method can be thought as another sensorless control method, since angular position sensors are not used. The term pseudo-sensorless has also been used due to the inclusion of magnetic sensors.

4.1 Magnet edge leakage flux waveforms

The stray flux of an IPMSM is easiest to be measured in front of the magnets embedded in the rotor where they are exposed to air. Since the magnets in the rotor are placed in an alternating north-south pattern, the edge magnetic flux varies nearly sinusoidally over the rotor circumference. The maximum and minimum values of the stray magnetic flux are around the center of the north and south magnets, respectively. The zero cross-over happens in between the two adjacent magnets. The leakage flux shape is presented in Figure 4.1a.

The edge field of the magnets can be measured by any suitable magnetometer, like a Hall sensor or a fluxgate magnetometer. In this case linear Hall sensors should be used, since the output of discrete Hall sensors is not suitable for the post-processing applied later. As seen in Figure 4.1a, one pole pair creates one full leakage flux cycle. Therefore the angle of the leakage flux is the same as the electrical angle of the rotor. Magnetic sensors are placed in front of the magnets so that they have an electrical angle of 90 degrees between them, which would equal to nine mechanical degrees on a ten-pole-pair machine. The sensors are marked as black squares in Figure 4.1a. One of the sensors ends up on the d-axis and another on the q-axis. With this configuration, as the rotor turns, one of the sensors produces a sine signal and the other gives a cosine signal. The resulting waveforms are shown in Figure 4.1b. Choosing a correct distance for the sensors from the magnet edge is critical in order to achieve sinusoidal signals. If the sensors are placed too close to the magnets, they will saturate, creating square wave signals. As the distance increases, the magnitude of the flux density will decrease rapidly. At the same time, the signal to noise ratio gets worse.

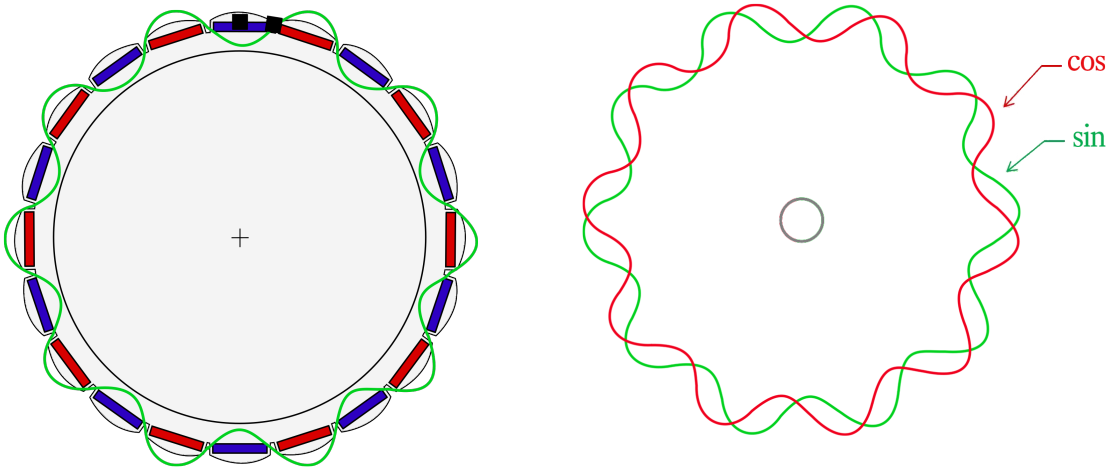

(a) (b)

Figure 4.1. (a) The pattern of the magnet edge leakage flux around a 10-pole pair IPMSM rotor. Note that in reality the leakage flux lines are traveling mostly in the axial direction. (b) The signals measured by two magnetic sensors set magnetically 90 degrees apart.

Because the outputs of the sensors can be considered sine and cosine, a rotor angle estimation can be calculated with

$$\hat{\theta} = \tan^{-1}\left(\frac{x_\beta(t)}{x_\alpha(t)}\right), \tag{4.1}$$

where x_β is the sine signal and x_α is the cosine signal. In reality, the signals are not ideal sine and cosine, since higher order harmonics are also present. In particular, a large third harmonic component has been reported, caused by the shape of the magnets and the dispersion of their magnetic field. The sine and cosine signals containing higher order harmonics can be expressed with

$$\begin{aligned} x_\alpha(t) &= \sum_{n=1}^{\infty} A_n \sin\left[n\left(\omega_0 t + \frac{\pi}{2}\right)\right] \\ x_\beta(t) &= \sum_{n=1}^{\infty} A_n \sin(n\omega_0 t). \end{aligned} \tag{4.2}$$

The summation of a harmonic component to a fundamental is illustrated in Figure 4.2. The harmonics introduce errors in the rotor position calculation, making the result unusable for control algorithms. Therefore a lot of effort has been put into filtering them out from the signal. High order harmonics can be effectively eliminated by using a low-pass filter. However, eliminating the third harmonic with a low-pass filter is problematic. As the cut-off frequency of the filter is close to the frequency of the useful signal, filtering operations can also distort the shape of the leakage flux. Especially a phase delay will be introduced. A large phase delay will be harmful for a control system which is designed to work in real time, since the signal used for position feedback will be delayed. Therefore, different correction algorithms based on mathematical models and signal processing techniques have been developed.

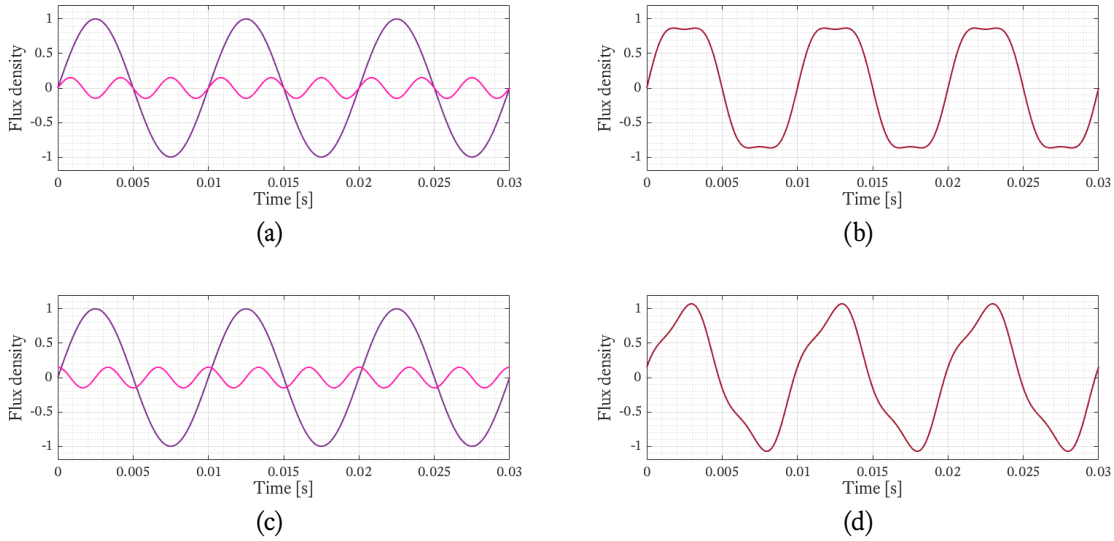

Figure 4.2. Leakage flux waveforms. The shape of the waveform depends largely on the phase of the third harmonic: (a) fundamental harmonic and the third harmonic, no phase shift; (b) the resulting sum wave from a); (c) fundamental harmonic and the third harmonic with 90 degrees phase shift; (d) the resulting sum wave from c).

In a correction algorithm developed by (Jung et al., 2010), a correction factor is applied to the signal depending on its phase. At angles of 0°, 90°, 180° and 270°, the signal deviates most from the true angle, so a maximum correction factor is applied. At angles 45°, 135°, 225° and 315° no corrections are made. The in-between values are corrected with a linear function. The effectiveness of the correction algorithm was reported to be dependent on choosing the right correction factor. As a result the control method was demonstrated to be working, but in the end it was concluded to be suitable only for applications which do not require precise position control. As such, it is not studied further in this thesis. A more promising signal processing

method is presented instead in section 4.4.

4.2 Inverse tangent method

Speed measurement devices used in feedback loops are required to provide good accuracy, reliable output and fast operation. To realize this, measurement signals are sent to post-processing electronics before being used elsewhere in the system. In post-processing, the final angle value is calculated for example by a digital signal processor (DSP). The post-processing circuitry can also contain error-correcting algorithms which try to compensate inevitable manufacturing defects or eliminate signal noise. Naturally, each type of device uses an algorithm that is best suited for that particular device.

The leakage flux measured from PMs around the motor has ideally a sinusoidal shape. When measured with two magnetometers like described in section 4.1 and filtered to eliminate the harmonics, a pattern that is similar to the output of sinusoidal encoders can be read. It is useful to study methods that are used to extract angle information from the output of a sinusoidal encoder, since many of them could be used by a stray flux–based measurement system.

A typical layout for the post-processing electronics of a sinusoidal encoder is presented in Figure 4.3.

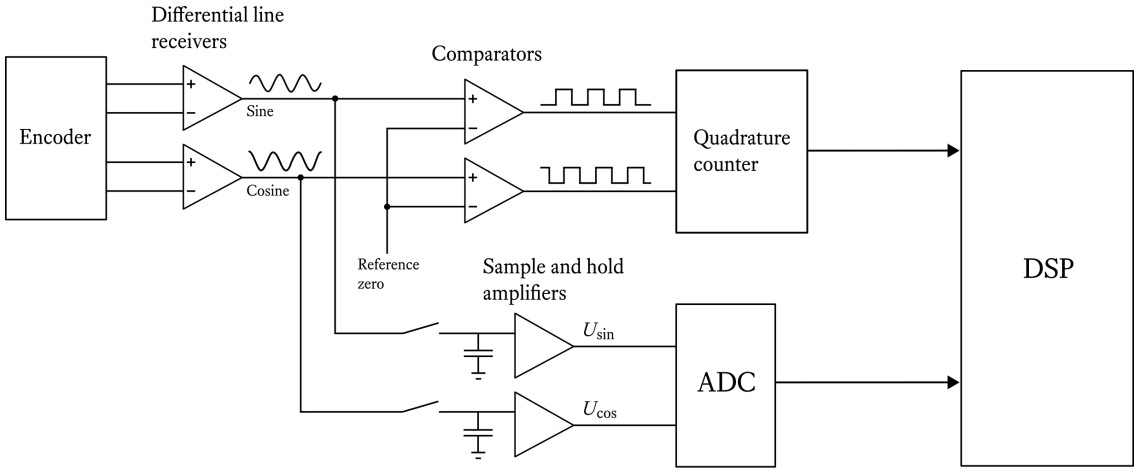

Figure 4.3. Typical sinusoidal encoder interface. (Sick Stegmann, 1999)

The encoder has four outputs. Two of the signals are the sine and cosine used in the angle calculation. Two other signals are the inverses of the first signals, which are used for signal correction. All signals are fed to differential noise amplifiers. In addition to blocking noise, they can be used to amplify and level shift the signals to make them better suited for further processing. One differential amplifier receives a signal and its inversion. Because of the amplifier, the output amplitude will be double compared to the input signal. At this point, the signal is fed into two separate sections. One section is responsible for calculating a coarse angle value while the other calculates a fine angle value that has a better resolution.

4.2.1 Coarse angle calculation

The signals are fed to an analog-to-digital converter (ADC) stage, which prepares the signals for digital processing. At first, the signals enter two comparators. As the name suggests, they compare their input to some preset value (like zero), effectively turning the sine and cosine signals into square wave signals with a 90 degrees phase shift. A square wave is preferred in signals carrying information since they are less susceptible to noise.

Next, both signals are fed to a quadrature counter. Using the quadrature method is a great advantage, as it provides four times the resolution over direct pulse count. Basically the counter feeds both signals through a logical XOR-port. The truth table of a XOR-port is shown in Table 4.1 and the signal input and output waveforms in Figure 4.4. As seen from the output waveform, the number of state changes has doubled compared to the input signal.

Table 4.1. Truth table of a XOR-port.

Input A	Input B	Output
0	0	0
0	1	1
1	0	1
1	1	0

The quadrature counter also takes into account the direction of rotation. Whenever the counter receives an edge in the signal and signal A leads signal B, it increments its value by one. When the direction is reversed, signal B leads A and the counter is decremented by one at each edge.

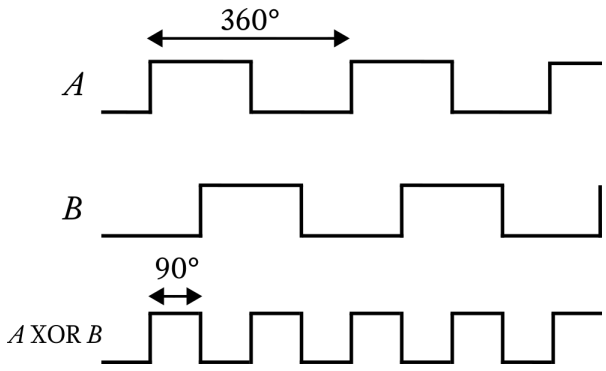

Figure 4.4. Quadrature encoding.

The direction of the encoder shaft can then be determined based on whether the counter is rising or falling.

In order to detect state changes, the signals sampled at the current time step A_n and B_n and the signals sampled at the previous time step A_{n+1} and B_{n+1} are both stored in memory. The counter action is determined based on Table 4.2.

Table 4.2. Quadrature counting.

A_n	B_n	A_{n+1}	B_{n+1}	**Counter**
0	0	0	0	No action
0	0	0	1	+1
0	0	1	0	-1
0	0	1	1	Invalid
0	1	0	0	-1
0	1	0	1	No action
0	1	1	0	Invalid
0	1	1	1	+1
1	0	0	0	+1
1	0	0	1	Invalid
1	0	1	0	No action
1	0	1	1	-1
1	1	0	0	Invalid
1	1	0	1	-1
1	1	1	0	+1
1	1	1	1	No action

”Invalid” refers to a state transition that should not happen in quadrature encoding during normal operation. If a counter receives an invalid state, there has been a fault and an error is given. Naturally, the counter should have a higher sampling rate than the bandwidth of the sine and cosine signals in order to not miss any pulses. The output of the counter produces a crude position estimate and its resolution is determined by the number of sine periods on the encoder ring. Usually this coarse resolution is not sufficient for speed control loops. For finer resolutions, a single sine period needs to be broken down into smaller parts.

4.2.2 Fine angle calculation

In order to calculate a more accurate angle value, the sine and cosine signals from the differential amplifiers are interpolated by an analog-to-digital converter (ADC). In principle, the resolution of the angle estimation is limited only by the quality and resolution of the ADC and signal noise. In Figure 4.3, the sine and cosine signals are fed to sample and hold amplifiers (SHA) before being passed to an ADC. A SHA consists of an operational amplifier, capacitor and a switch, such as a transistor. It samples the voltage of an analog input and holds its output at the sampled level for a specified period of time. This kind of pre-processing eliminates errors from the conversion process of an ADC. The bandwidth of the ADC should be at least twice the maximum sine and cosine frequency to avoid signal aliasing.

The exact method for fine angle calculation varies from protocol to protocol. Most methods rely on the arctangent function at some point in the calculation process. The method described here is used by the Hiperface®-interface and provides a good balance between speed and complexity.

A sine/cosine period is divided into eight octants according to Table 4.3 and Figure 4.5a. Based on the octant, the signals are then transformed into x and y coordinates according to Table 4.4. The transformation results in the graph 4.5b.

The algorithm continues by calculating $T(\theta) = x(\theta)/y(\theta)$, shown in Figure 4.5c. The advantage of this step is that it results in T which always has a value between zero and one. This is favorable for the next step, the arctangent function calculation. Different methods have been proposed in literature to calculate an arctangent such as:

Table 4.3. Determination of the octant.

$V_{\sin} \geq 0$	$V_{\cos} \geq 0$	$\lvert V_{\sin}\rvert < \lvert V_{\cos}\rvert$	Octant
True	True	True	0
True	True	False	1
True	False	False	2
True	False	True	3
False	False	True	4
False	False	False	5
False	True	False	6
False	True	True	7

Table 4.4. A sine/cosine transformation.

Octant	X	Y
0	$V_{\sin}$	$V_{\cos}$
1	$V_{\cos}$	$V_{\sin}$
2	$-V_{\cos}$	$V_{\sin}$
3	$V_{\sin}$	$-V_{\cos}$
4	$-V_{\sin}$	$-V_{\cos}$
5	$-V_{\cos}$	$-V_{\sin}$
6	$V_{\cos}$	$-V_{\sin}$
7	$-V_{\sin}$	$V_{\cos}$

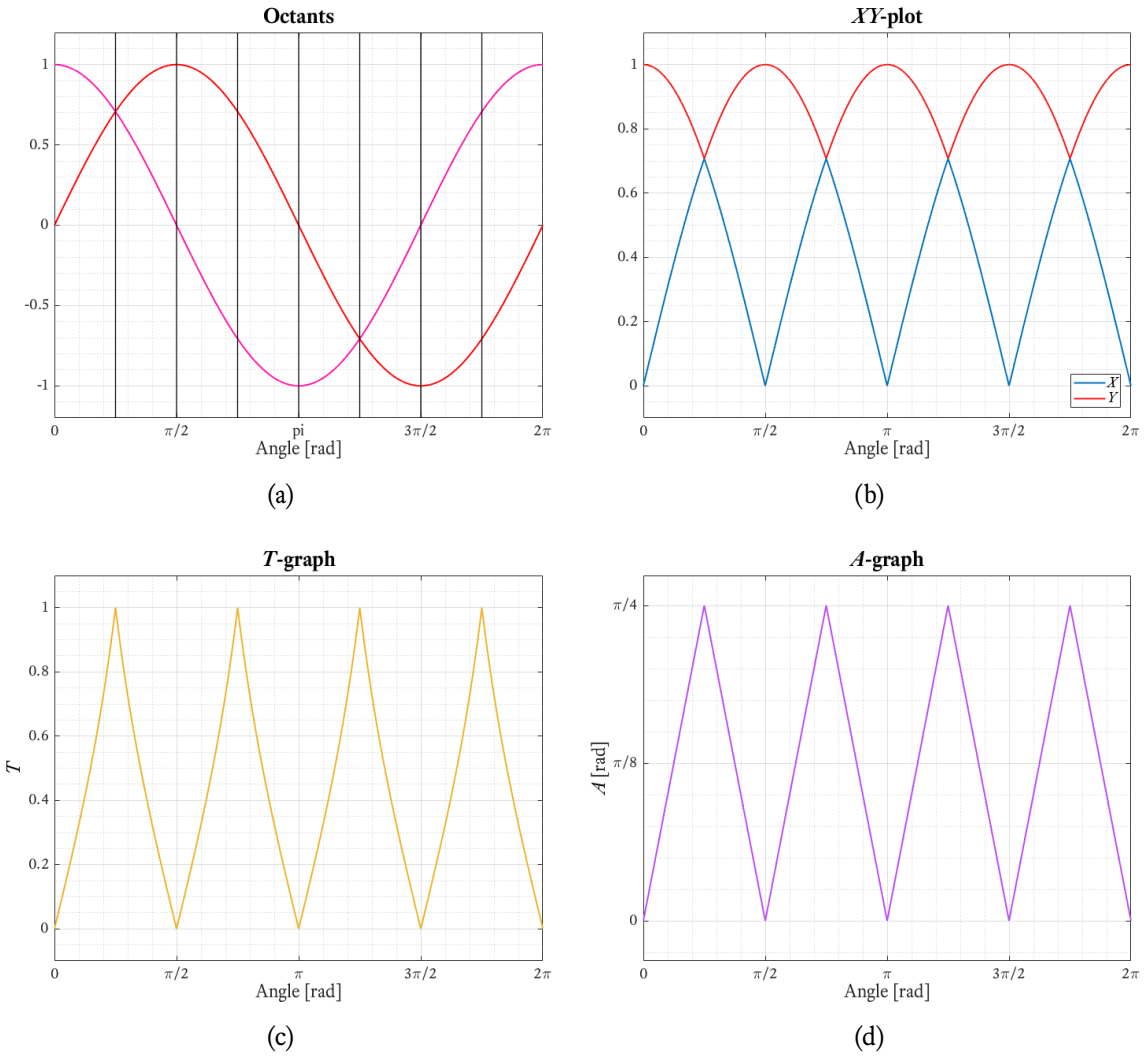

Figure 4.5. The calculation of a fine angle from a sine/cosine period: (a) division to eight octants; (b) transformation to an xy-graph; (c) calculation of $T(\theta)$; (d) calculation of the arctangent function.

- A look-up table
- Newton-Raphson iteration with an iterative function (Hu et al., 2012)
- Taylor series expansion (Burke et al., 2000)

In the interface presented here, a look-up table is used. Values of $\tan^{-1}$ have been precalculated into the memory of a DSP, and it can fetch the correct values with a very low latency. In the subsequent Figure 4.5d, $A = \tan^{-1}(T)$ has been calculated. Finally, A is transformed to a fine angle $0° \leq \theta < 360°$ by using Table 4.5. (Sick Stegmann, 2016)

Table 4.5. Fine angle calculation.

Octant	θ
0	A
1	$90° - A$
2	$90° + A$
3	$180° - A$
4	$180° + A$
5	$270° - A$
6	$270° + A$
7	$360° - A$

4.2.3 Total angle calculation

The total final angle is calculated by adding the coarse and fine angle together in the DSP. The resolution of the coarse angle is determined by the number of sine and cosine cycles at the encoder ring. An encoder with 512 cycles can count up to 2047 during one revolution using quadrature counting $(4 \times 512 - 1)$. In other words, its resolution is 11 bits or $360°/2047 \approx 0.176°$. Similarly, a 1024-line encoder can reach 4095 counts per revolution and a 12-bit resolution. By adding the result of the fine angle calculation, the resolution can be increased. Every position within the sine/cosine period has an unique combination of signals, which means that in principle, the resolution is again limited only by the ADC. Therefore the fine angle resolution depends on the quality of the ADC used. If the resolution of the ADC is for example 12 bits, the final angle resolution can reach 24 bits with a 1024-line encoder. To

illustrate the concept, a 5-bit resolution is used for fine angle calculation in Figure 4.6. (Sick Stegmann, 1999)

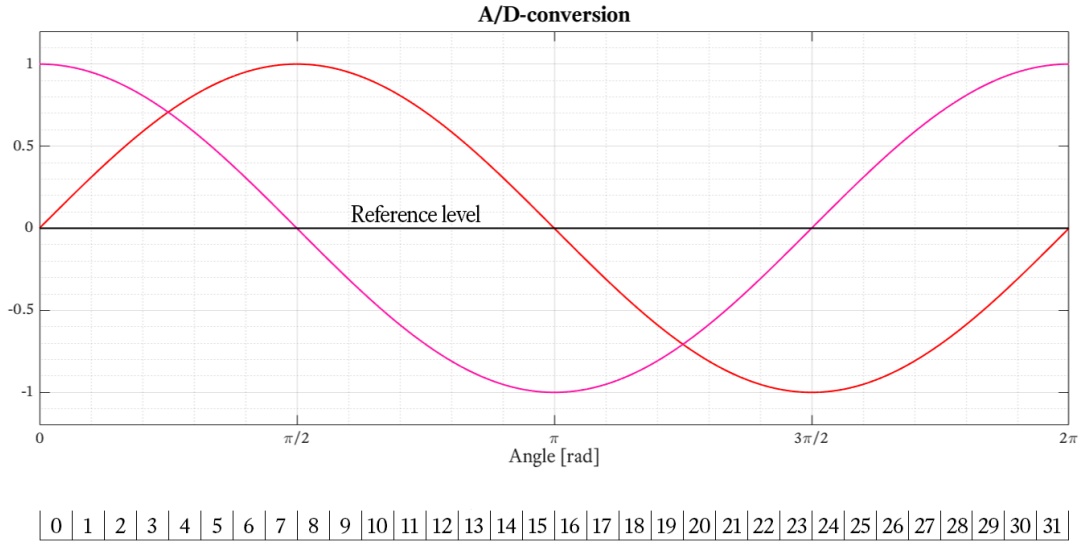

Figure 4.6. Sine and cosine sampled with 5-bit resolution. (Sick Stegmann, 2016)

In a real system there are always error sources. Large errors can cause substantial jitter in the output signals and the fine angle interpolation will produce incorrect results. Potential sources of error include: (iC Haus GmbH, 2014)

- Poor magnetization of the encoder ring
- Signal reading errors regarding amplitude and offset of the signal
- Errors in sensor alignment
- Analog-to-digital interpolation and signal conditioning errors

A small angle jitter at the output of the measurement system is acceptable, since there is always inertia in the mechanical system that is controlled with a position feedback loop. The inertia of the machine will absorb any high-frequency errors. Any jitter inside the measuring system is still highly unwanted. The error sources that were listed can be presented in the arctangent function

$$\theta = \tan^{-1}\left(\frac{A_{\sin}F_{\sin}(\theta_{\sin}+\theta_{\sin,\mathrm{err}})+O_{\sin}}{A_{\cos}F_{\cos}(\theta_{\cos}+\theta_{\cos,\mathrm{err}})+O_{\cos}}\right). \tag{4.3}$$

$A_{\sin}$ and $A_{\cos}$ are coefficients representing an amplitude error. It is defined as any difference between the sine and cosine amplitudes. $\theta_{\sin,\mathrm{err}}$ and $\theta_{\cos,\mathrm{err}}$ represent phase error, defined as any difference between the actual phase shift of the sine and cosine and the ideal 90 degrees phase shift. $O_{\sin}$ and $O_{\cos}$ are offset errors with respect to the reference level. $F_{\sin}$ and $F_{\cos}$ are functions approximating sine and cosine waves, but they also include some nonidealities like higher frequency harmonics.

It is important to know which of these errors are the most harmful in the angle calculation. A system designer could then identify errors that should be corrected and errors that can be ignored. In Chapter 6, the leakage flux–based method will be evaluated using the error sources presented here. A leakage flux method would rely more heavily on the fine angle calculation than a sinusoidal encoder, since the number of full sine/cosine periods is limited to the number of pole pairs. In general, PMSMs in elevator applications have a large pole pair number in order to produce a smooth torque, but compared to a sinusoidal encoder some resolution would still be lost. Thus, correcting the most harmful errors would be even more important.

4.3 Inverse sine method

Instead of using two Hall sensors to measure the sine and cosine of the leakage flux, three sensors could be used and placed 120 electrical degrees apart from each other. The output of the three sensors is similar to any three-phase electrical system. A block diagram of the position detection is shown in Figure 4.7. (Chang and Tzou, 2007)

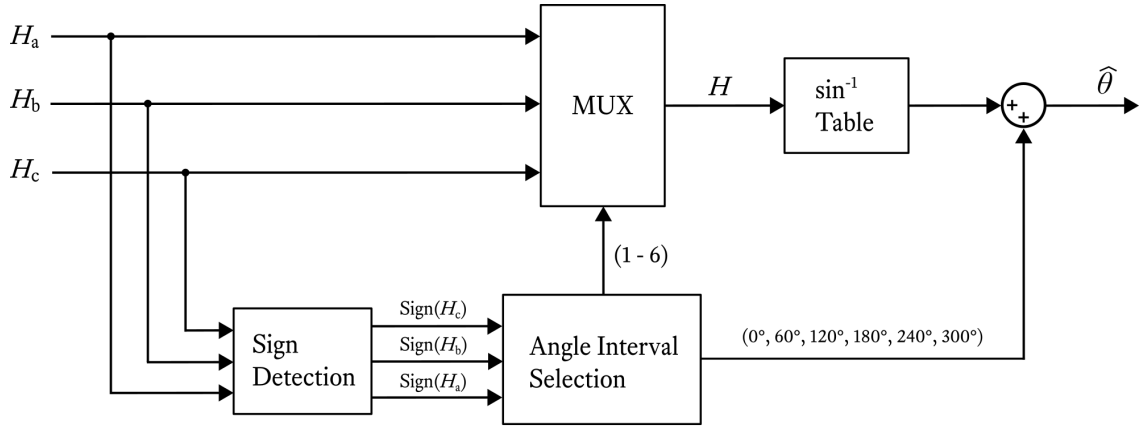

Figure 4.7. Angle calculation with three Hall sensors. (Chang and Tzou, 2007)

A full sine period is divided into six intervals, each of which is 60 degrees wide. First, the current section is determined by the signs of the Hall signals according to Figure 4.8 and Table 4.6. In sections 2, 4 and 6 the sign of the signal is switched from negative to positive, resulting in function $T(\theta)$.

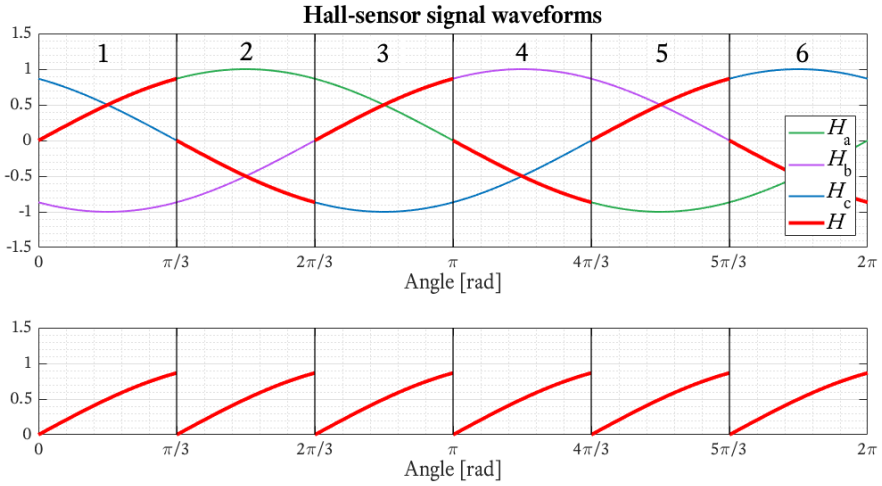

Figure 4.8. The leakage flux waveform obtained from three Hall sensors. Below is the sign-corrected signal $T(\theta)$ which is fed to an arcsine function. (Chang and Tzou, 2007)

Table 4.6. Angle interval selection (left) and final angle calculation (right).

H_a	H_b	H_c	Interval
$+$	$-$	$+$	1
$+$	$-$	$-$	2
$+$	$+$	$-$	3
$-$	$+$	$-$	4
$-$	$+$	$+$	5
$-$	$-$	$+$	6

Interval	θ
1	A
2	$60° + A$
3	$120° + A$
4	$180° + A$
5	$240° + A$
6	$300° + A$

Next, the fine angle is calculated by arcsine-function as $A = \sin^{-1}(T)$ using a look-up table. The resolution of the angle calculation is again dependent on the analog-to-digital converter and the size of the look-up table. In a 12-bit ADC, two least significant bits could be cut out to reduce the influence of signal noise.

4.4 ANF-PLL filter method

In their current form, the inverse tangent and sine methods do not include any filtering for the input signals. Any harmonics would introduce substantial errors in the angle calculation. Unlike applications like fans or pumps, which run mostly on constant speed, elevators have a variable speed. A linear filter is not sufficient to eliminate the third-order harmonic from the measurement signal, since the motor speed is variable. Therefore, the filter needs to be able to eliminate harmonics across a large speed range. A combination of an adaptive notch filter (ANF) and a phase-locked loop (PLL) can be constructed in order to achieve this. Both of them are introduced in this section. In Chapter 5, they are combined into one filter and evaluated in simulations. The model is based on research done by (Jung and Nam, 2011) and (Lee et al., 2017).

4.4.1 Adaptive notch filter

A notch filter is a bandstop filter. It passes most frequencies unaltered, but strongly attenuates frequencies in its designed bandstop. Notch filters have a high *Q-factor*, enabling them to have a narrow bandstop region. For a normal notch filter, the bandstop region lies on a constant frequency range. For an adaptive notch filter, the bandstop region can be adjusted during operation by control software. This characteristic makes them applicable for electric motor applications, where the operational frequency changes as the motor accelerates or decelerates. (Luo and Hou, 1995)

The circuit diagram of an ANF is presented in Figure 4.9. It contains two integrators $1/s$ and two gains σ. The coefficient σ is the inverse of the Q-factor, and determines the sharpness of the filter. The signal fed to the ANF is the measurement signal from one of the Hall sensors, shown in

$$x(t) = A\cos\omega_0 t + A_\mathrm{h}\sin\omega_\mathrm{h} t + B_\mathrm{h}\cos\omega_\mathrm{h} t. \tag{4.4}$$

In this case it is a cosine signal, but a similar sine signal is also fed to an another ANF. It contains the fundamental amplitude coefficient A, the fundamental frequency ω_0, harmonic amplitude coefficients A_h and B_h and the harmonic frequency ω_h. One of the harmonic components

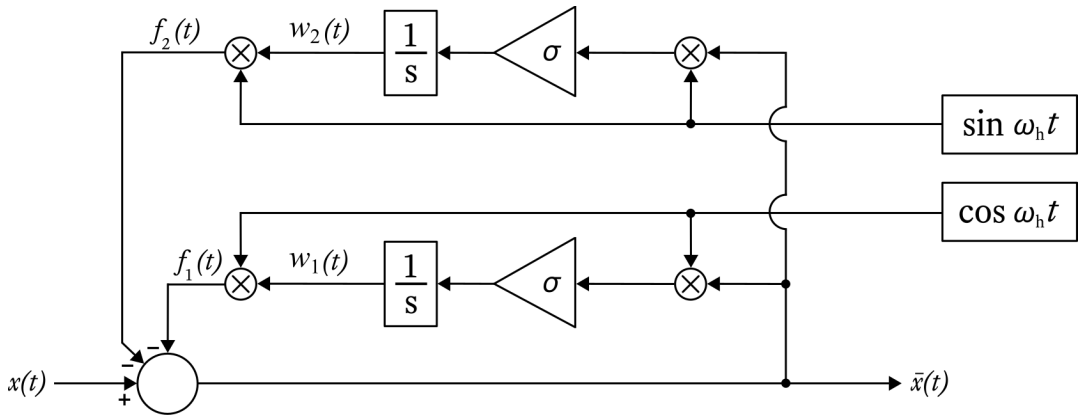

Figure 4.9. A circuit diagram for an adaptive notch filter. (Jung and Nam, 2011)

($B_\mathrm{h} \cos \omega_\mathrm{h} t$) has no phase shift compared to the fundamental wave, while the other ($A_\mathrm{h} \sin \omega_\mathrm{h} t$) has a phase shift of 90 degrees. The output of the filter is denoted as $\bar{x}(t)$. When the filter is operating correctly, it can be approximated as $\bar{x}(t) \approx A \cos \omega_0 t$. The two feedback signals feeding into the filter contain harmonic components $\sin \omega_\mathrm{h} t$ and $\cos \omega_\mathrm{h} t$.

The filter can be modeled analytically by deriving a transfer function for it. The final system makes use of two ANFs, one for each measured signal from the Hall sensors. The analysis is similar for both of them. From Figure 4.9, the signal $w_1(t)$ can be expressed as

$$w_1(t) = \int \left[\bar{x}(t)\sigma \cos(\omega_\mathrm{h} t)\right] dt. \tag{4.5}$$

According to Euler's formula, $\cos(\omega_\mathrm{h} t)$ can also be expressed as

$$\cos(\omega_\mathrm{h} t) = \frac{1}{2}(e^{j\omega_\mathrm{h} t} + e^{-j\omega_\mathrm{h} t}). \tag{4.6}$$

In order to derive a transfer function, a Laplace transform of the signal needs to be taken. Let $W_1(s) = \mathcal{L}(w_1)$ and $\bar{X}(s) = \mathcal{L}(\bar{x})$. By substituting 4.6 to 4.5 and taking a Laplace transform,

$$W_1(s) = \mathcal{L}\left[\int \left(\bar{x}(t) \cdot \frac{\sigma}{2}(e^{j\omega_\mathrm{h} t} + e^{-j\omega_\mathrm{h} t})\right) dt\right] = \frac{\sigma}{2s}\bar{X}(s - j\omega_\mathrm{h}) + \frac{\sigma}{2s}\bar{X}(s + j\omega_\mathrm{h}). \tag{4.7}$$

Here a Laplace transform is taken by using the identity

$$\mathcal{L}\left\{e^{at}f(t)\right\} = F(s-a). \tag{4.8}$$

The signal is also passed through an integrator, which was taken into account in Equation (4.7) by multiplying the signal with the Laplace transform of an integrator, $1/s$. Signal $f_1(t)$ from Figure 4.9 is a product of $w_1(t)$ and the feedback $\cos(\omega_\mathrm{h} t)$. Its Laplace transform $F_1(s)$ can be calculated as

$$\begin{aligned}
F_1(s) &= \mathcal{L}\{w_1(t) \times \frac{1}{2}(e^{j\omega_\mathrm{h} t} + e^{-j\omega_\mathrm{h} t})\} \\
&= \frac{1}{2}[W_1(s - j\omega_\mathrm{h}) + W_1(s + j\omega_\mathrm{h})] \\
&= \frac{1}{2}\Big\{\frac{\sigma}{2(s - j\omega)}\bar{X}(s - j\omega_\mathrm{h} - j\omega_\mathrm{h}) + \bar{X}(s + j\omega_\mathrm{h} - j\omega_\mathrm{h}) \\
&+ \frac{\sigma}{2(s + j\omega)}\bar{X}(s - j\omega_\mathrm{h} + j\omega_\mathrm{h}) + \bar{X}(s + j\omega_\mathrm{h} + j\omega_\mathrm{h})\Big\} \\
&= \frac{\sigma}{4(s - j\omega_\mathrm{h})}[\bar{X}(s - 2j\omega_\mathrm{h}) + \bar{X}(s)] + \frac{\sigma}{4(s + j\omega_\mathrm{h})}[\bar{X}(s + 2j\omega_\mathrm{h}) + \bar{X}(s)].
\end{aligned} \tag{4.9}$$

Similarly, a Laplace transform can be calculated for $f_2(t)$:

$$\begin{aligned}
F_2(s) = &\frac{\sigma}{4(s - j\omega_\mathrm{h})}[\bar{X}(s) - \bar{X}(s - 2j\omega_\mathrm{h})] \\
&+ \frac{\sigma}{4(s + j\omega_\mathrm{h})}[\bar{X}(s) - \bar{X}(s + 2j\omega_\mathrm{h})].
\end{aligned} \tag{4.10}$$

The total feedback signal for the ANF is

$$f(t) = f_1(t) + f_2(t), \tag{4.11}$$

and its Laplace transform

$$\begin{aligned}\mathcal{L}\{f(t)\} &= F(s) = F_1(s) + F_2(s) \\ &= [\frac{\sigma}{2(s - j\omega_\mathrm{h})} + \frac{\sigma}{2(s + j\omega_\mathrm{h})}]\bar{X}(s) \\ &= \frac{2\sigma s}{2s^2 + 2\omega_\mathrm{h}^2}\bar{X}(s) = \frac{\sigma s}{s^2 + \omega_\mathrm{h}^2}\bar{X}(s).\end{aligned} \tag{4.12}$$

The feedback coefficient $G(s)$ is defined as a ratio of the feedback signal to the output signal:

$$G(s) = \frac{F(s)}{\bar{X}(s)} = \frac{\sigma s}{s^2 + \omega_\mathrm{h}^2}. \tag{4.13}$$

Now the transfer function $H(s)$ for the ANF can be defined:

$$H(s) = \frac{\bar{X}(s)}{X(s)} = \frac{1}{1 + G(s)} = \frac{s^2 + \omega_\mathrm{h}^2}{s^2 + \sigma s + \omega_\mathrm{h}^2}. \tag{4.14}$$

The transfer function is equivalent to an ideal second-order notch filter. When the input frequency ω is equal to ω_h, the gain of the filter becomes zero, $|H(j\omega)| = 0$. Therefore the harmonic frequency will be greatly attenuated. Also, when $\omega \gg \omega_\mathrm{h}$ or $\omega \ll \omega_\mathrm{h}$, $|H(j\omega)| = 1$, so other frequencies than the harmonic can pass the filter unaltered. The center frequency for the attenuation depends only on the harmonic frequency of the input. Consequently the characteristics of the filter are independent of the parameter variations of the individual components, which might happen due to aging or temperature variations.

The bandwidth of the notch filter in Equation (4.14) is

$$\Delta\omega = \sigma^2, \tag{4.15}$$

so it can be controlled by setting an appropriate value for the gain σ. Signals $w_1(t)$ and $w_2(t)$ correspond to the estimates of the harmonic coefficients. When the output of the integral stops increasing or decreasing, the system reaches a steady-state. At this point the estimates should be equal to the real harmonic coefficients, $w_1(t) \rightarrow B_\mathrm{h}$ and $w_2(t) \rightarrow A_\mathrm{h}$. The system will automatically track any variations in the harmonic frequency, ensuring the filtering effect. This

kind of behavior is especially useful in real time measurement systems, and a key reason why it was chosen for this study.

4.4.2 Phase-locked loop

A phase-locked loop is a phase-tracking system. It synchronizes an output signal to an input signal in frequency and phase. The output is generated by an internal oscillator. In a locked state, the phase error between the oscillator's output signal and the reference input signal is zero, or alternatively some constant value. If an error in the phase is detected, the oscillator is controlled in order to make the error zero again. The internal phase is therefore "locked" to the reference phase. PLLs are widely used in electrical equipment such as AC/DC converters, UPS's and active power filters. In electrical machine applications a PLL is used to filter out harmonics. A PLL is constructed with three subcomponents: a voltage-controlled oscillator (VCO), a phase detector (PD) and a loop filter (LF). Different parts are marked to Figure 4.10.

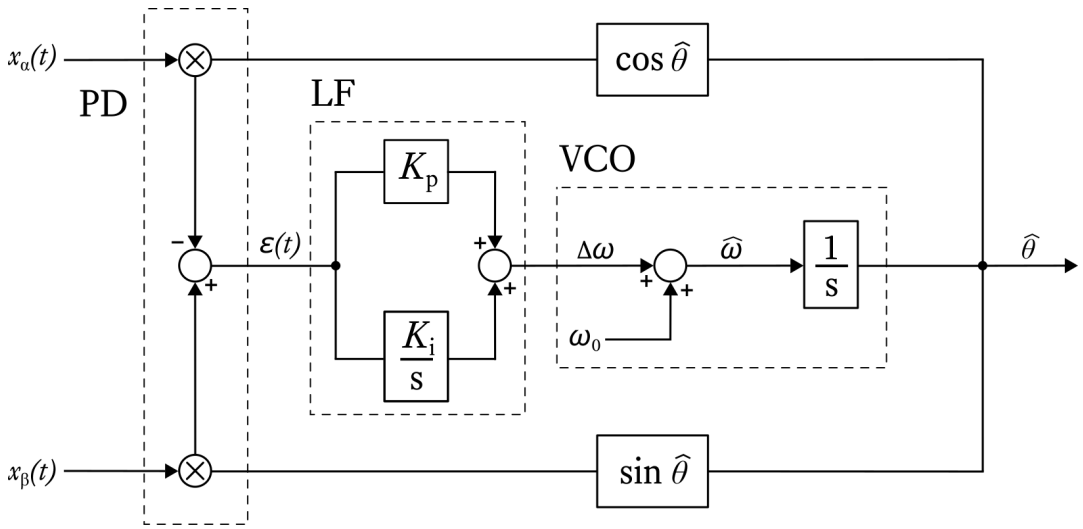

Figure 4.10. A circuit diagram for a phase-locked loop. K_p and K_i are coefficients for a PI-controller, $\epsilon(t)$ is the phase error signal, ω_0 is the internal oscillator signal, $\Delta\omega$ is the input frequency to the VCO, $\hat{\omega}$ is the frequency estimate and $\hat{\theta}$ is the angle estimate. (Jung and Nam, 2011)

The output of the VCO and the reference signal are compared in the phase detector, which outputs an error signal $\epsilon(t)$ to the loop filter. The loop filter in turn controls the operating frequency of the VCO. If the input frequency is increased by $\Delta\omega$, the phase of the input signal starts leading the phase of the output signal. The phase detector will detect this and start

outputting a non-zero signal. The integral in a PI-controller starts building up a phase error and its output will begin to rise. This will cause the VCO to increase in frequency. The phase error starts to decrease, and after some time the VCO will oscillate with the same frequency as the input signal. In the process the phase error has been reduced to zero or some finite value. (Best, 2007).

Electrical machines and AC/DC converters make use of an orthogonal PLL. It can handle two orthogonal signals, like sine and cosine. As a motor controlled with a PLL accelerates or decelerates, the base frequency of the system is changed. A normal PLL would produce second-order harmonics as a result of the sine and cosine multiplication in the phase detector, but in an orthogonal PLL these are not present. However, if the input signals contain harmonics higher than second order, they are still transmitted to the PLL. The harmonics would have a negative effect on the PLL performance. The input signals containing third-order harmonics can be expressed as

$$\begin{aligned} x_\alpha(t) &= \sum_{n=1}^{\infty} A_n \sin\left[n\left(\omega_0 t + \frac{\pi}{2}\right)\right] \approx A\sin(\omega_0 t + \frac{\pi}{2}) + A_\mathrm{h}\sin(3\omega_0 t + \frac{3\pi}{2}) \\ &= A\cos\omega_0 t - A_\mathrm{h}\cos 3\omega_0 t \\ x_\beta(t) &= \sum_{n=1}^{\infty} A_n \sin(n\omega_0 t) \approx A\sin\omega_0 t + A_\mathrm{h}\sin 3\omega_0 t. \end{aligned} \tag{4.16}$$

As shown in Figure 4.10, the error signal produced by the phase detector would then be

$$\begin{aligned} \epsilon(t) &= x_\beta(t)\cos\hat{\omega}t - x_\alpha(t)\sin\hat{\omega}t \\ &= A(\sin\omega_0 t\cos\hat{\omega}t - \cos\omega_0 t\sin\hat{\omega}t) + A_\mathrm{h}(\sin 3\omega_0 t\cos\hat{\omega}t + \cos 3\omega_0 t\sin\hat{\omega}t) \\ &= A(\sin(\omega_0 - \hat{\omega})t) + A_\mathrm{h}(\sin(3\omega_0 + \hat{\omega})t). \end{aligned} \tag{4.17}$$

It can be seen from Equation (4.17) that if the PLL is operating in steady-state and $\omega_0 \approx \hat{\omega}$, the harmonics would change from third order to fourth order, expressed as $A_\mathrm{h}\sin 4\omega_0 t$. The harmonics would be fed to the loop filter, and its performance would deteriorate, especially at low speeds. If the phase tracking system would be used with an IPMSM, the input signals would contain a large amount of third-order harmonics. Therefore, using a notch filter to remove

the harmonics before feeding them to the PLL is essential in order to make the measurement system robust and accurate.

A transfer function of the PLL is also constructed to help the design process. First, the filter is linearized by modeling all the remaining harmonics from the ANFs as $\epsilon(t)$. Now the error signal to the PI-controller becomes $e(t) = \epsilon(t) + \tilde{\theta}$, where $\tilde{\theta} = \theta - \hat{\theta}$. The linearized system is presented in Figure 4.11.

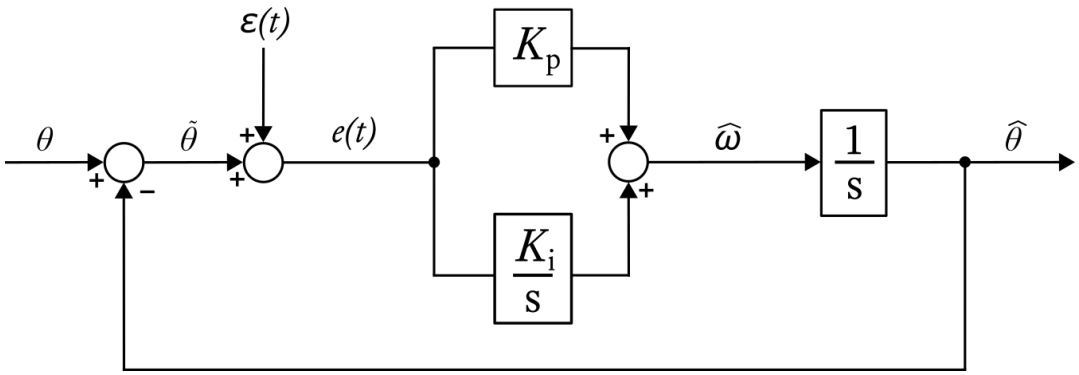

Figure 4.11. A linearized PLL. (Jung and Nam, 2011)

A transfer function from $\epsilon(t)$ and $\tilde{\theta}(t)$ can be defined by setting all other inputs to zero and reducing the block diagram to one block. First, K_p, K_i/s and $1/s$ are combined to $G(s)$,

$$G(s) = \frac{K_\mathrm{p}}{s} + \frac{K_\mathrm{i}}{s^2}. \tag{4.18}$$

The feedback loop can be taken into account by

$$\frac{\tilde{\theta}(t)}{\epsilon(t)} = \frac{G(s)}{1 + G(s)} = \frac{K_\mathrm{p}s + K_\mathrm{i}}{s^2 + K_\mathrm{p}s + K_\mathrm{i}}, \tag{4.19}$$

which gives the final transfer function. The transfer function has a characteristic polynomial $s^2 + K_\mathrm{p}s + K_\mathrm{i}$, so the poles of the PI-controller can be placed freely by properly choosing gains K_p and K_i. To avoid oscillations and achieve robustness, the poles should be placed on the real

axis, $s = -\rho$, where ρ is a positive constant. Therefore the gains should be chosen as

$$\begin{aligned} K_{\mathrm{p}} &= 2\rho \\ K_{\mathrm{i}} &= \rho^2. \end{aligned} \tag{4.20}$$

The poles have an effect on the bandwidth of the PLL. Using for example the bandwidth()-function in MATLAB, the bandwidth of the transfer function can be calculated as 2.48ρ. Since any harmonics higher than the third order present in the PLL input should be filtered, the bandwidth should be less than four times the fundamental frequency. On the other hand, a too narrow bandwidth will cause a large phase delay. In a leakage flux–based feedback system, this also means that the location of the PI-controller poles should be chosen according to the possible fundamental frequencies in the system.

Chapter 5

Modeling the leakage flux measurement

This chapter focuses on simulations of the adaptive notch filter and the phase-locked loop. The simulation model is built with the numerical computing software packages MATLAB and Simulink by MathWorks. In order to test the ANF-PLL filter performance, different test cases are designed. All simulations are based on situations which might occur in elevator use. Special attention is paid to the input signal so that it would match a leakage flux waveform from a real machine in all the test cases.

5.1 Simulation model

Each section in the model is built using function blocks from the standard library of Simulink or the Digital signal processing system toolbox. The overall structure of the model is presented in Figure 5.1. The input for the filter is composed in the block named ”Leakage flux measurement”. The ”Reference speed” block is used to calculate the error between the commanded reference speed and the actual speed value given by the ”ANF-PLL filter” block. By integrating the reference speed, an angle error can also be calculated. Based on Equation (4.4), Hall sensor signals consisting of the fundamental frequency and a large third-order harmonics are modeled as

$$\begin{aligned} x_\alpha &= A\cos\omega_0 t + A_{3\alpha}\sin 3\omega_0 t + B_{3\alpha}\cos 3\omega_0 t \\ x_\beta &= A\sin\omega_0 t + A_{3\beta}\sin 3\omega_0 t + B_{3\beta}\cos 3\omega_0 t. \end{aligned} \tag{5.1}$$

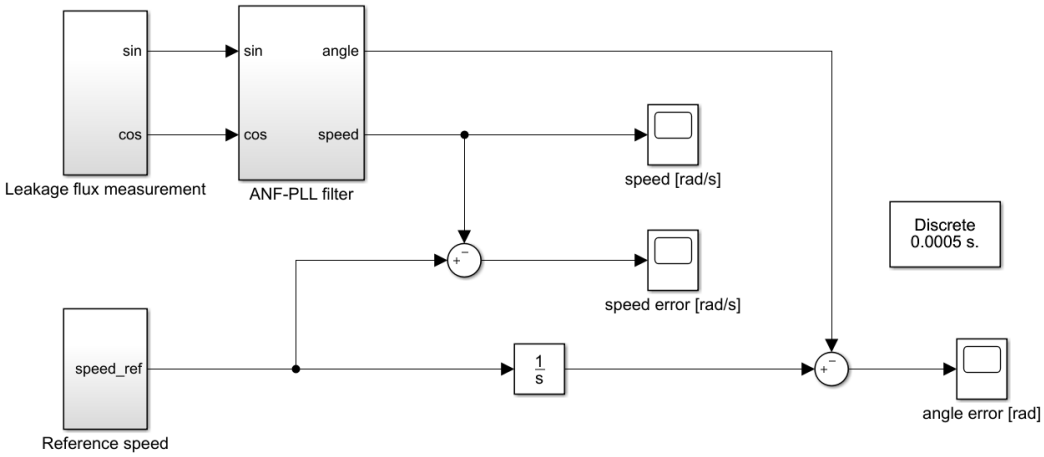

Figure 5.1. Overall structure of the simulation model.

Sine and cosine signals are constructed separately using sine wave blocks. A constant frequency sine is sufficient for modeling constant speed, but whenever the elevator speed chances, the frequency of the measured signal should also change. Every speed change profile can be modeled as a series of linear ramp signals. Even if the speed has a lot of variation, by using infinitesimally short ramps, the true speed can be followed. Step-like changes are not possible, since all rotating bodies have inertia. A chirp signal is a signal that increases linearly in frequency. With it, leakage flux signals resulting from linear speed changes can be modeled.

Third order harmonics that are present in the measured signal can be simulated by adding them to the sine and cosine waveforms. One of them has the same phase as the fundamental frequency, represented by a sine component in the sine wave and a cosine component in the cosine wave. The other has a 90 degrees phase shift. The amplitude of the harmonics is governed by gains $A_{3\alpha}$, $B_{3\alpha}$, $A_{3\beta}$ and $B_{3\beta}$. With a switch block the frequency can be changed from a chirp signal to a constant frequency. The whole block set can also be chained together with other block sets to achieve other ramps and frequencies. A basic building block for a signal is presented in Figure 5.2. Both sine and cosine signals are generated independently. The resulting waveform is shown in Figure 5.3a.

The generated signal has a linear increase in frequency from zero to five hertz during one second. After one second it continues as a five hertz signal. To convert this to the speed of the rotor in rounds per minute, electrical degrees are converted to mechanical degrees and the resulting value is converted to rounds per minute, as in equation

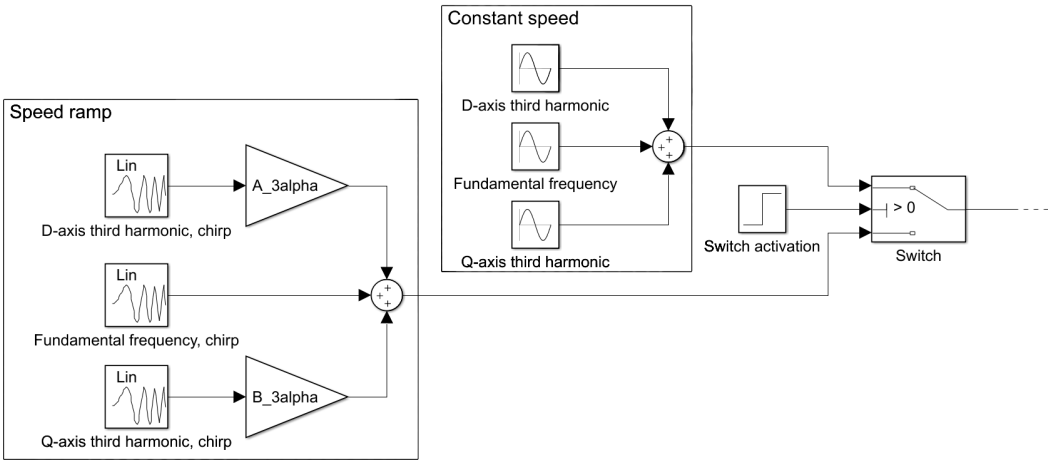

Figure 5.2. A simulation block set for signal generation

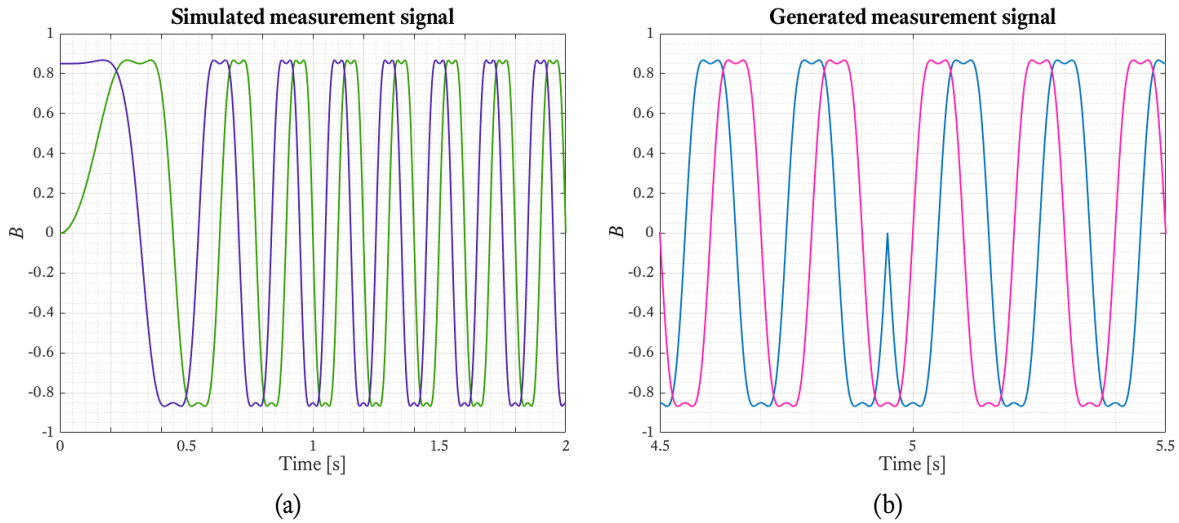

(a) (b)

Figure 5.3. (a) The generated Hall sensor signal from Figure 5.2. (b) A rotation direction change at t = 4.95 s.

$$n = \frac{30}{\pi p}\omega. \tag{5.2}$$

Since one pole pitch represents 180 electrical degrees, information about the pole pair number p is needed. For a machine with 16 pole pairs and a five hertz output signal the above equation yields 18.75 rpm. In most cases a motor running at nominal speed would produce a signal at a much higher frequency.

An elevator motor needs to run in both directions. When measuring the leakage flux, a change in direction can be detected in the two Hall signals. In particular, there is going to be a 180 degrees phase shift in both of the signals, as can be seen in Figure 5.3b. The direction can be detected based on which of the two signals is leading the other. In the simulation, a phase shift is added to all components of the signals whenever the direction is changed.

A Hall sensor signal was constructed according to a speed profile that starts with acceleration from standstill to the nominal speed of a motor, followed by constant speed. After some time, the signal performs a deceleration to standstill. This is done in both positive and negative directions, representing normal elevator use.

Measurement signals are fed to the ANF-PLL filter as inputs. First of all, the third harmonic components are filtered out by the ANFs. A block diagram of one of the ANFs is presented in Figure 5.4. The sine and cosine signals are fed through separate ANFs since the harmonic components are likely different in separate measurement locations.

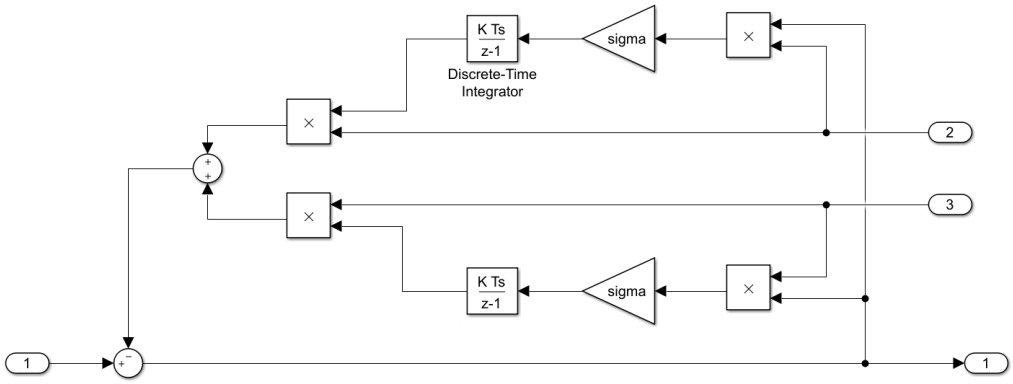

Figure 5.4. An adaptive notch filter constructed in Simulink.

The input labeled 1 receives $x_\alpha(t)$ or $x_\beta(t)$ modeled in Equation (5.1). Both ANFs need also the frequency that is supposed to be filtered as reference signals $\sin \omega_\mathrm{h} t$ and $\cos \omega_\mathrm{h} t$. The fundamental frequency of the system is generated in the output of the PLL, and from there it is turned to $\sin 3\theta$ and $\cos 3\theta$ and fed to the ANFs as reference. In other words the ANFs act as a feedback path for the PLL. The filtered output signals of the ANFs are $\bar{x}_\alpha \approx A \sin \omega_0 t$ and $\bar{x}_\beta \approx A \cos \omega_0 t$. The ANF output is fed to the PLL as an input, as shown in Figure 5.5.

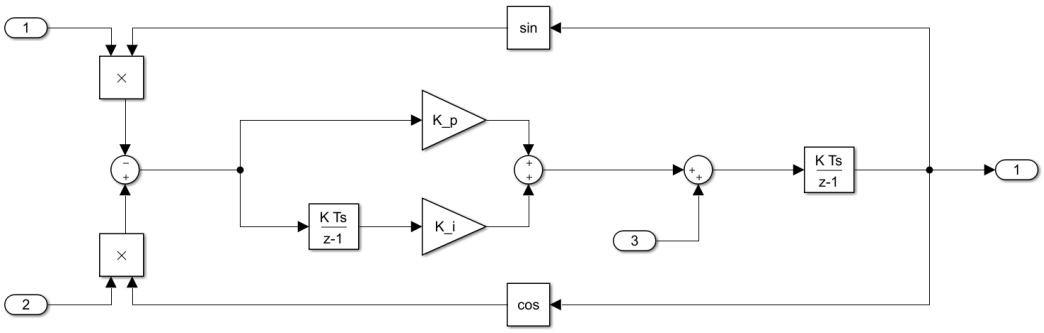

Figure 5.5. A phase-locked loop constructed in Simulink. Inputs 1 and 2 come from the ANFs and input 3 is the fundamental frequency ω_0.

The PLL requires also the fundamental frequency of the measurement signal ω_0 as an input. It needs to be calculated from the Hall signals. A block diagram of the process is shown in Figure 5.6.

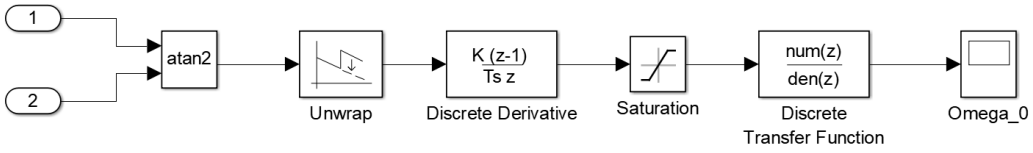

Figure 5.6. Filtering of the fundamental frequency.

To begin with, the sine and cosine signals are fed to an atan2()-function, which calculates a four-quadrant inverse tangent of its inputs. Since the output of atan2-function is bound to $[-\pi, \pi]$ and has a discontinuity every 2π radians, it needs to be unwrapped to produce a continuous signal. The unwrap-function from the DSP System Toolbox does this by adding multiples of 2π to the output every time the input signal experiences a phase jump which exceeds a certain tolerance value. Since in this case the phase jump is 2π, a tolerance of π is sufficient.

The angle values are then differentiated in order to produce a frequency signal. A numerical

derivative can result in large spikes in the output signal if a division is done with a nearly zero value. To make the simulation more stable, a saturation block is added.

The sine and cosine signals used as inputs are largely unfiltered. This results in large oscillation in the speed signal, so it needs to be subjected to a lowpass filter. A butterworth-type filter is selected because of its ability to produce minimum ripple to the passband. Butterworth filters also have a slower roll-off to the stopband compared to other filter types like Chebyshev I and II, but in this case a flat passband is more desirable. The roll-off slope can be improved by designing a higher-order filter. On the other hand, the order should not be too high since it introduces unnecessary complexity. A third order filter is seen as a good balance between roll-off and complexity.

The filter is designed using butter()-function from the Digital signal processing toolbox. A low cut-off frequency should be used, since the output signal represents motor speed that ideally does not have a lot of ripple. In the simulation a cutoff frequency of 10 Hz is selected. The filter is then implemented as a discrete time transfer function with a structure as in

$$H(z) = \frac{\text{num}(z)}{\text{den}(z)} = \frac{b_0 z^m + b_1 z^{m-1} + ... + b_m}{a_0 z^n + a_1 z^{n-1} + ... + a_n}, \tag{5.3}$$

where the coefficients are determined as shown in Table 5.1.

Table 5.1. Transfer function coefficients.

i	a_i	b_i
0	1	3.757×10^{-6}
1	-2.937	1.127×10^{-5}
2	2.876	1.127×10^{-5}
3	-0.939	3.757×10^{-6}

The zeros of the third order Butterworth filter are placed on the negative real axis. The poles contain a small imaginary part and are placed on the positive half-plane, as can be seen from Table 5.2. If a higher sampling frequency is used in the filter design, the poles move closer to $1 + 0j$.

An important parameter that affects the performance of the filter is its sample time. The model

Table 5.2. Poles and zeros of the Butterworth filter.

Zeros	Poles
$-1+0j$	$0.984+0.0268j$
$-1+0j$	$0.969+0j$
$-1+0j$	$0.984-0.0268j$

was first verified using continuous time. In order to implement the model to a digital signal processor, it needs to be discretized. Every continuous simulation block, like integrator, derivator and transfer function block, was replaced by its discrete counterpart. A common sample time was used with all of the blocks, and the simulation solver was chanced from continuous to a fixed-step, discrete type. Equation (3.10) was used in sample time selection. Considering a motor with 16 pole pairs running at nominal speed of 371.36 rpm, the equation results in

$$\begin{aligned}\Delta t &= \frac{1}{m \times (n/60) \times p \times 360} = \frac{1}{2 \times (371.36\,\mathrm{rpm}/60) \times 16 \times 360} \\ &= 1.4025 \times 10^{-5}\,\mathrm{s}.\end{aligned} \tag{5.4}$$

A full presentation of the filter simulation diagram can be found in Appendix A1.1.

5.2 Simulation results

The model was tested using different test scenarios. A speed estimation system should be able to handle at least the following situations, which were used as guides when designing the tests: (Kivimäki, 2005)

- Zero speed
- Low constant speed
- Zero-crossing
- Stopping from a constant speed to zero speed
- Acceleration from zero speed to a constant speed

The coefficients for the harmonic components in the input signals are set to $A_{3\alpha} = 0$, $B_{3\alpha} = -0.15$, $A_{3\beta} = 0.15$, $B_{3\beta} = 0$. These values are similar in real stray flux measurements. The PLL PI-controller poles are placed to -150 on the real axis. The sharpness of the ANF σ is set to two.

The performance of the adaptive notch filters can be studied by comparing the frequency contents of their input and output signals. A fast Fourier transform function in MATLAB was used to shift the signals into frequency domain. The result is presented in Figure 5.7.

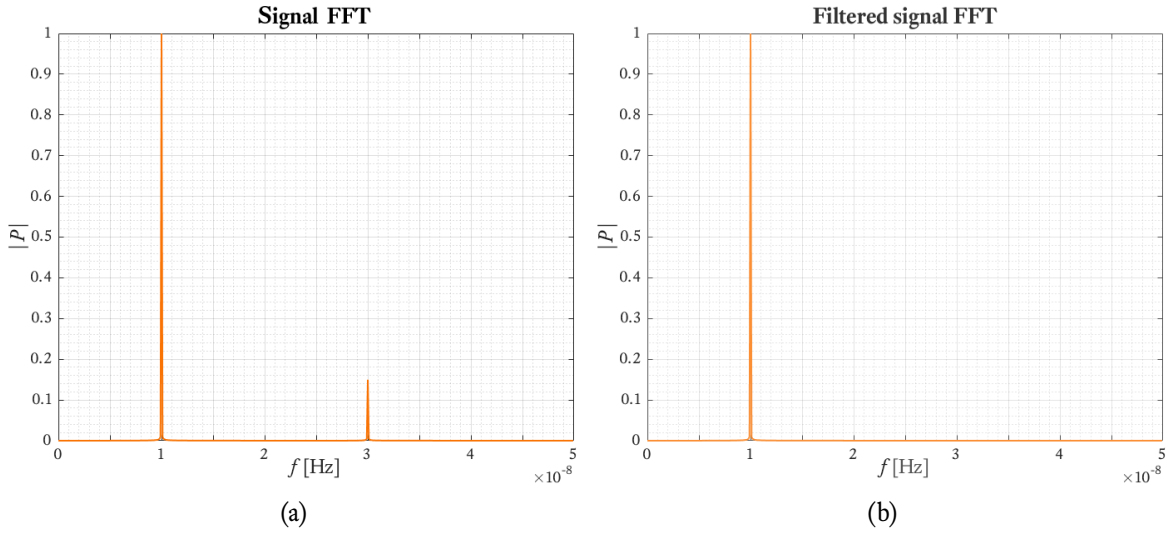

Figure 5.7. A fast Fourier transform: (a) ANF-PLL filter input; (b) ANF-PLL filter output.

As expected, before filtering harmonic components are present and the total harmonic distortion (THD) is 15 %. THD reflects the choices that were made for $B_{3\alpha}$ and $A_{3\beta}$. After filtering, the third harmonic component has disappeared completely. Some very high harmonics have appeared, but their amplitudes are small (not visible in the figure). Since the signal fed to the filter was designed to contain only one harmonic, the filter seems to be working very well.

An angle estimate is calculated with $\tan^{-1}(\sin\theta/\cos\theta)$ from both the unfiltered and filtered signal, presented in Figure 5.8. The unfiltered angle estimation contains great variation from the real angle, and is unusable for position feedback. On the other hand, the filtered signal looks very clean and stable enough to be used as a feedback signal.

As discussed earlier in section 4.4, signals w_1 and w_2 for the sine and cosine correspond to the harmonic component coefficiets $A_{3\alpha}$, $B_{3\alpha}$, $A_{3\beta}$ and $B_{3\beta}$. These coefficients are plotted in

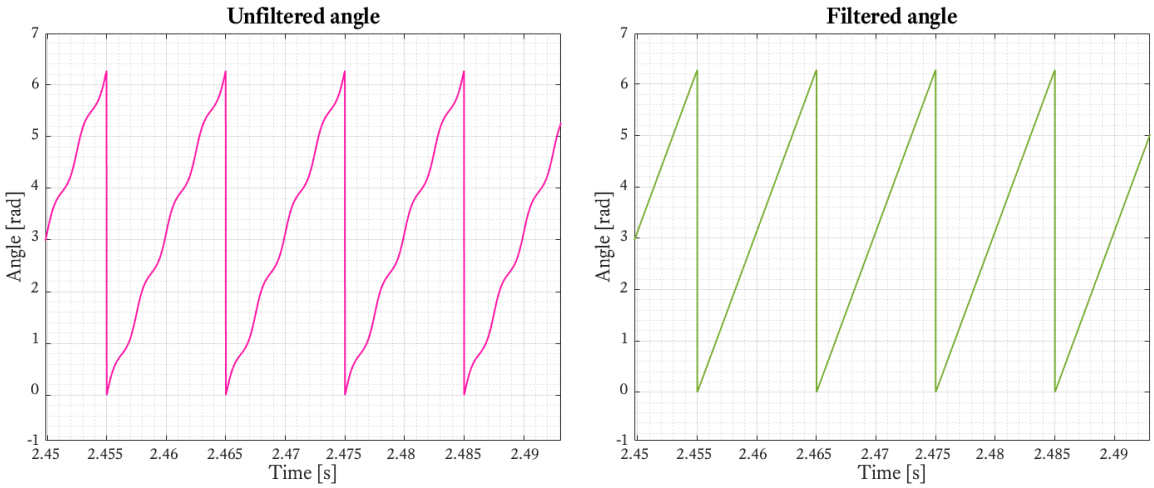

Figure 5.8. The calculated angle: (a) unfiltered; (b) filtered.

Figure 5.9 from the start of the simulation. All coefficients start from zero, and are then driven to their steady-state values. Comparing them to the real values set before the simulation, it can be concluded that they converge to their respective values correctly. The convergence takes about five seconds.

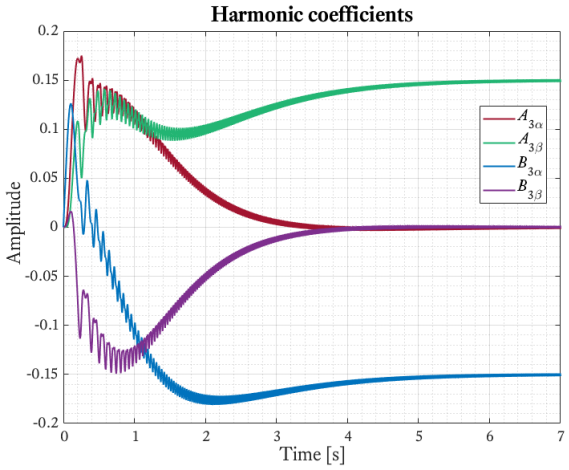

Figure 5.9. Harmonic coefficients in the filter input.

A speed profile shown in Figure 5.10a is simulated. The output of the simulation is shown in Figure 5.10b. At the start of the simulation, when the harmonic coefficients have not yet converged, there is a large speed error. After five seconds, the simulated speed follows the reference accurately.

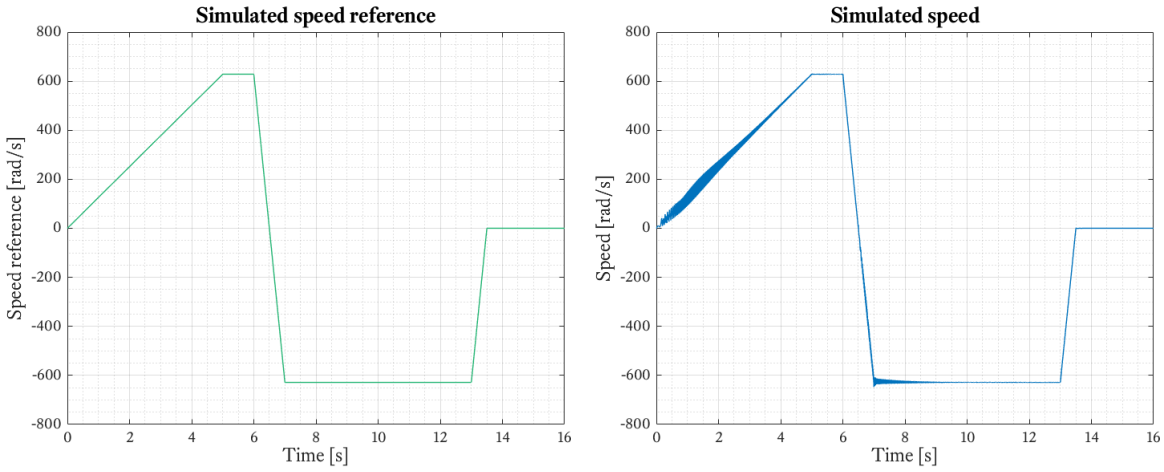

(a) (b)

Figure 5.10. (a) The reference speed. (b) The simulated speed.

Special attention should be given to the zero crossing, since any speed estimation system can easily generate errors at that point. In this case, the filter loses the information about the leakage flux coefficients for a while, and the coefficients start diverging until the leakage flux is measured again. The zero crossing happens at $t = 6.5\,\mathrm{s}$ in the simulation. As the speed increases to the negative direction, the coefficients stabilize again, which can better be seen in Figure 5.11b. Although the zero crossing causes a small error, the filter begins to adjust itself accordingly immediately afterwards, and the error begins to attenuate. The filter seems to handle the situation well, since there are not any large error spikes at the zero crossing instant. It should also be noted that in normal elevator use fast zero crossings should not happen.

At the start of acceleration and deceleration, small error spikes are are present, as can be seen from Figures 5.11a and 5.11b. However, they disappears quickly as the motor runs in steady-state or constant acceleration. At zero speed the input signals are zero, which leaves a small angle error at the end of the simulation. All in all, the filter seems to be following the correct rotor angle very accurately.

In real-life applications, heavy oscillation at the start of the simulation would be a serious problem. The model needs quite a long time to reach steady-state, approximately five seconds. During that time, the speed and angle estimates are not accurate and cannot be used for position feedback. The oscillation is a consequence of the harmonic coefficients being inaccurate in the beginning. The time that it takes for the coefficients to converge can be adjusted by tuning the PI-controller in the PLL to be more aggressive. However, a controller that is too aggressive results in a large overshoot, so the adjustment time cannot be completely eliminated. More-

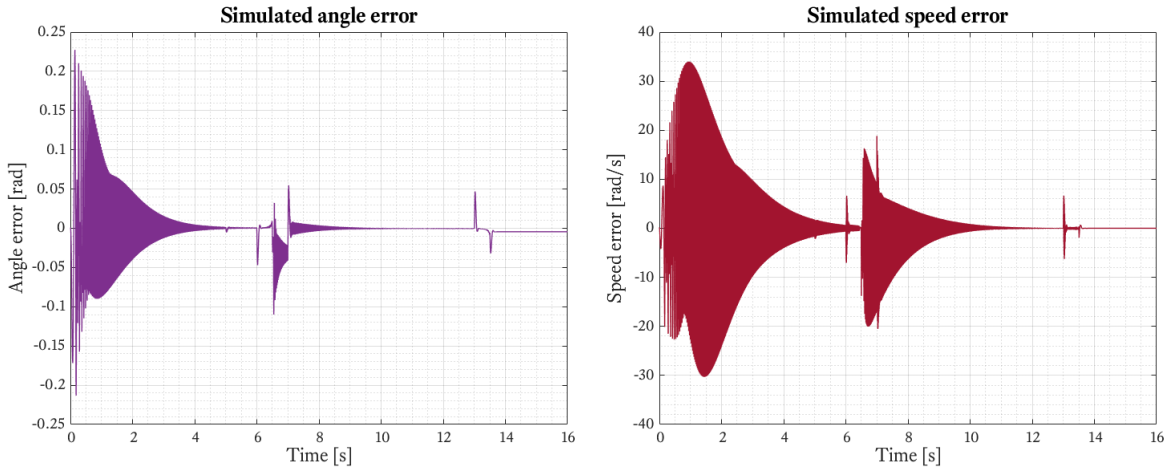

(a) (b)

Figure 5.11. Simulated (a) angle error in electrical degrees; (b) speed error.

over, the adjustments to the harmonic coefficients need to be done every time the motor starts from standstill, so every time the elevator starts a new ride. Zero-crossings would also be a problem, since an angle error is present for some time after a zero crossing.

This is not feasible, so a different approach must be taken. One option would be to perform an ID-run at the commissioning phase of a new elevator. The harmonic coefficients obtained from the ID-run would be stored in the control software. The sensing algorithm would then be turned off and replaced by the stored constant values. This approach would require a rigid body for the sensor attachment, since the harmonic coefficients change with respect to the distance to the magnet, and the fixed values would not be updated if the sensor position changes for some reason. Still, a rigid body for the sensors could be considered feasible to realize. The ID-run could then be repeated periodically in case the harmonic coefficients have changed over time.

The method was validated by a simulation. The result in Figure 5.12 shows that at the first start-up there is a heavy oscillation as the model converges to the right coefficients. This corresponds to the ID-run. By using initial guesses for the coefficients, they would not start from zero, and the oscillations would be smaller. When all coefficients have reached their steady-state value, they are locked to those values and the automatic sensing is turned off. Note that the second start-up is very smooth and no oscillations are present. The angle error is at maximum during accelerations to both directions. There are short spikes in the speed whenever the speed profile has a sharp transition, but they disappear immediately at the next calculation step. The speed error varies around two radians per second. The proposed method seems to be working as

expected.

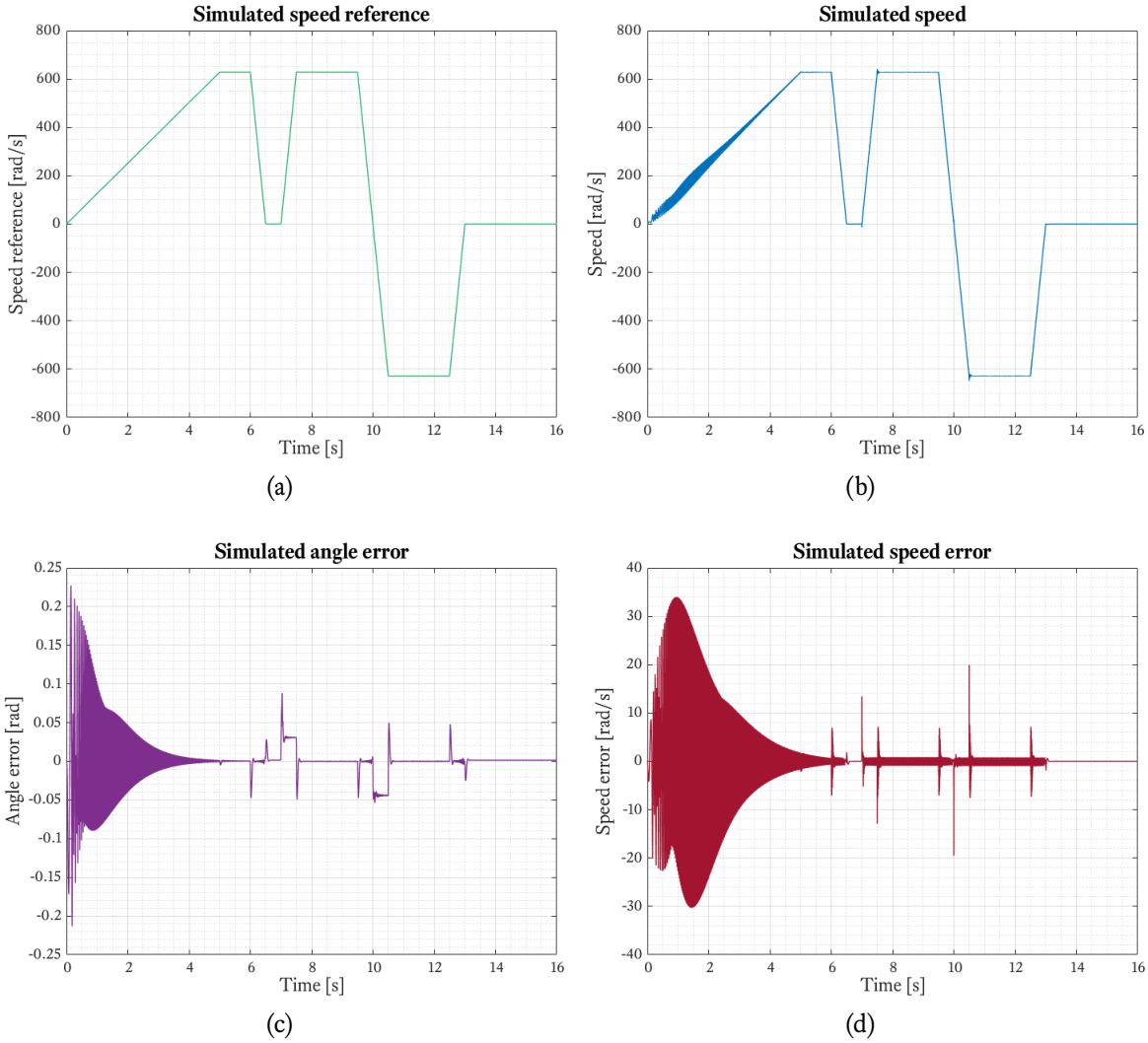

Figure 5.12. Simulated speed with an ID-run: (a) the reference speed; (b) the simulated speed; (c) angle error; (d) speed error.

To further test the suitability of the filter in elevator use, a test case with a faulty magnet was prepared. It represents a situation where the ability of one magnet to produces magnetic flux has deteriorated and would produce an anomaly in the leakage flux waveform. In order to run a simulation, a small amplitude was periodically subtracted from the normal measurement signals. The period depends on the pole pair count of the machine, in this case the subtraction occurs every 16th pole pair. The flux density amplitude was decreased to 75 percent from a normally functioning magnet. The resulting waveform can be seen in Figure 5.13a. A speed profile starting from standstill and accelerating to a constant speed in 0.5 seconds was used.

Locked harmonic coefficients described in the previous paragraph were also implemented.

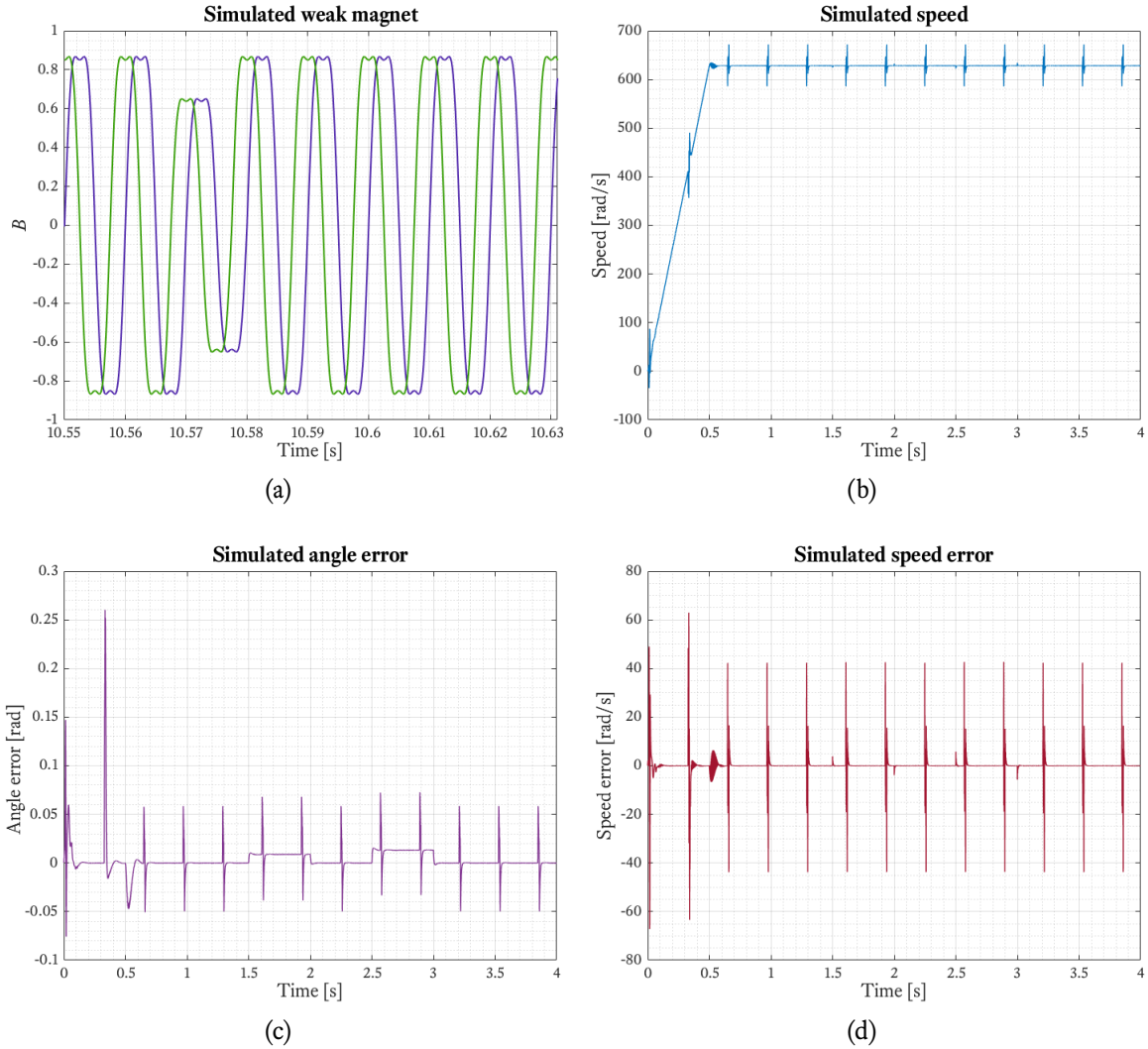

Figure 5.13. Simulated speed with a weak magnet: (a) generated signals; (b) the simulated speed; (c) angle error; (d) speed error.

The simulation shows that the magnetic defect produces a periodic error in the angle estimate. This error translates also to the calculated speed. The amplitude of the error is proportional to the amount of the magnetic defect. A 25 percent decrease in flux density produces an angle error of ±0.05 radians. The error increases significantly if the defected magnet is measured during acceleration or deceleration, as seen at t = 0.3 s. The effect of a single magnet defect is corrected very quickly by the filter, but if multiple magnets have considerably varying amplitudes, the angle output would become more distorted.

Chapter 6

Experimental procedure and analysis

Understanding the behavior of the magnetic leakage flux is essential for a successful speed measurement system development. Concrete measurements give a better understanding on how the shape of the leakage flux changes during different speed and torque profiles. In IPMSMs, the stator winding is often located near the rotor magnets. As the current in the windings increases, it starts to affect the shape of the stray flux. Correct locations for the magnetic sensors are also essential for accurate position estimation.

This chapter focuses on analyzing the results of several stray flux measurements. The ANF-PLL method of turning the measured leakage flux into useful speed information is also tested with real measurement signals. Two different radial flux machines are used, both of them manufactured by KONE. The different designs are referred to as machine 1 and machine 2.

6.1 Measurement system

The leakage flux is measured with a Wuntronic Koshawa 5–magnetometer that allows accurate real-time measurements. Its sensing probe can be switched according to the flux direction. One of the probes measures the flux parallel to the probe tip, and the other measures perpendicular flux. Each probe has a range up to 0.2 teslas. In this case a probe with a parallel head gives generally better results.

A zero calibration needs to be performed to the magnetometer. The probe is placed inside

a zero chamber, where the magnetic field is extremely small in all directions. The measured value is then calibrated to zero.

The magnetometer has an analog output capable of 20 kHz sampling frequency. It is connected to a Dewe43-A data acquisition unit from Dewesoft. The unit allows recording and analysis of the measured data by transferring it to a computer via USB. Its analog inputs are capable of up to 200 kHz sampling frequency and have a 24-bit resolution. The corresponding software is called Dewesoft X3, which provides real-time visualization, post-processing, filtering tools and calculations for the imported signals. The measurement instruments are shown in Figure 6.1.

Figure 6.1. Instruments used in the measurements: a Wuntronic Koshawa 5–magnetometer (left) and a Dewe43-A–unit (right)

Since the output of the magnetometer is a voltage signal in the range of ±800 mV, a correction factor where 800 mV corresponds to 200 mT is used. In this way the magnetometer display and the Dewesoft X3 software both give approximately the same reading. A small difference between these values depends mainly on factors such as:

- Noise signals induced to the measurement
- Filtering operations applied on the raw signals
- Time delay
- Sampling frequency

Dewesoft X3 provides a number of methods for reducing the noise of the measeured signals. The default noise-reduction filter is a anti-aliasing IIR filter. The input sampling frequency is

preferred to match the sampling frequency of the magnetometer to reduce sampling bias. It is set to 20 kHz. The setup is verified by placing a magnet on a rotating body and measuring its magnetic flux from several directions.

6.2 Machine 1

Machine 1 uses an embedded magnet topology with laminated pole shoes and magnet pockets similar to Figures 2.1d and 2.8. The goal of this configuration is to produce constant torque by shaping the rotor poles so that they resemble poles of a salient-pole machine. The magnetic flux produced in the air gap would then be sinusoidal under no external load. The configuration enables a quiet and smooth operation at low speeds with a good efficiency and power factor. Some key figures of the machine are listed in Table 6.1.

Table 6.1. Machine 1 characteristics.

Rotor diameter	0.35	m
Number of poles	32	
Rated power	9.3	kW
Rated speed	371	rpm
Rated torque	240	Nm
Rated current	18.1	A

The first step of the measurement process is to rotate the rotor by hand in order to eliminate the effect of stator end-winding currents on the measured signal. The measurement probe is placed in front of the magnets with a stand that allows adjustments to the distance from the probe tip to the magnets. Normally a brake prevents the rotor from rotating, so it is opened manually. A picture of the setup is presented in Figure 6.2.

The main goal of this measurement is to determine the shape of the leakage flux signal. Based on literature presented in section 4.1, it is assumed that the measured signal will contain a large third order harmonic. The second goal is to determine the effect of the distance between the probe and the magnet. The range of the magnetometer is wide enough to prevent saturation near the magnets, but this might not be true when using inexpensive measurement devices. On the other hand, if the distance is too long, it is difficult to use the signal for reliable speed estimation due to poor signal to noise ratio.

Figure 6.2. Measuring the PM edge flux from an IPMSM.

The distance is carefully increased in 2 mm intervals, starting from 2 mm. In Table 6.2 and Figure 6.3, it can be seen how the magnetic flux density decreases exponentially as the distance increases. Still, even at a relatively long distance the flux density shape is still clear. If the distance is increased even further, the signal becomes distorted and noisy. The probe is able to pick up a sinusoidal waveform even at 80 mm distance, however, at that point there is already a large amount of noise.

Table 6.2. The magnet edge leakage flux density peak values as a function of distance to the magnets.

l [mm]	$B_{\max}$ [mT]	$B_{\min}$ [mT]	l [mm]	$B_{\max}$ [mT]	$B_{\min}$ [mT]
2	78.7	-72.1	20	4.3	-6.4
4	41.0	-42.9	22	2.6	-4.9
5	26.0	-27.7	24	2.3	-4.6
6	21.8	-24.5	26	1.2	-3.5
8	18.1	-20.1	28	1.1	-3.3
10	13.9	-15.7	30	1.0	-3.2
12	9.7	-11.8	32	0.4	-2.6
14	7.7	-9.9	34	0.3	-2.5
16	7.4	-9.9	36	0.04	-2.3
18	4.7	-7.0			

The shape of the stray flux is presented in Figure 6.4a. In this case, the distance from the probe to the magnet is 5 mm, which results in a peak magnetic flux density of approximately 24 mT. The signal resembles a sine wave, but is somewhat skewed. It is expected to contain harmonics, so a Fourier transform is calculated in MATLAB. The result is presented in Figure

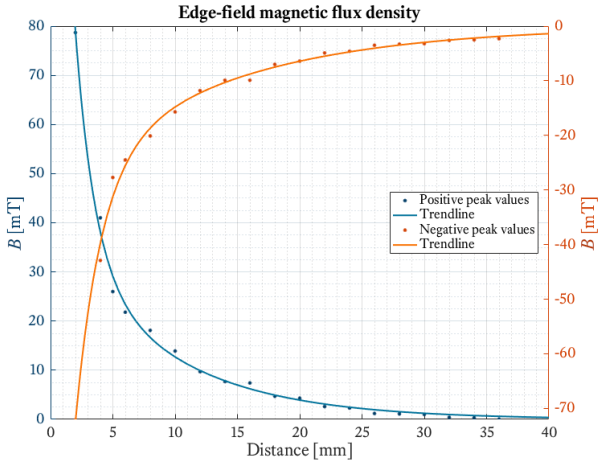

Figure 6.3. The magnet edge leakage flux density peak values as a function of distance to the magnets.

6.4b. Like initially suspected, a third order harmonic component can be seen. In addition to the fundamental frequency and the third harmonic, there are sideband frequencies around them. They appear mostly because the rotation speed is not constant when rotating the rotor by hand, and the frequency spectrum gets wider.

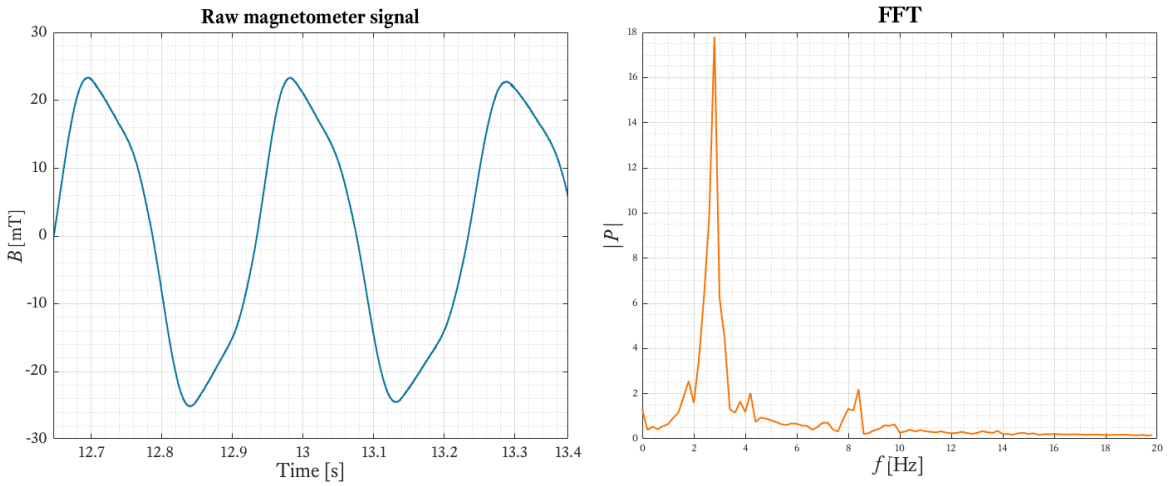

Figure 6.4. (a) Shape of the leakage flux measured at 5 mm distance from the rotor. (b) Power spectrum of the leakage flux signal. The frequency of the fundamental is 2.8 Hz and the frequency of the third harmonic is 8.4 Hz.

An ANF-PLL filter should be effective in removing the third harmonic. However, at this stage the speed of the rotor is too low and unstable to effectively test the filter. Moreover, at this point it is not yet reasonable to determine the optimal position for the measurement probe

in the radial or tangential direction, since the stator end-winding currents are not taken into account.

A follow-up test is conducted in order to determine the behavior of the leakage flux when the machine is producing torque. The machine is installed to a test setup where it is possible to apply load with a generator. The purpose of the measurement is to determine the shape of the leakage flux under different speed and load profiles. The currents flowing in the stator winding induce their own magnetic field, which interferes with the leakage field of the magnets. Thus it is investigated how the leakage changes under the influence of different amounts of stator current. Also the position of the probe has an effect on the measured flux shape. Over the course of several measurements, the position of the probe tip is changed to different locations. Specifically, the following positions are considered:

1. In front of the rotor under a stator tooth
2. In front of the rotor under a stator slot
3. Near the stator winding
4. Far from the stator winding

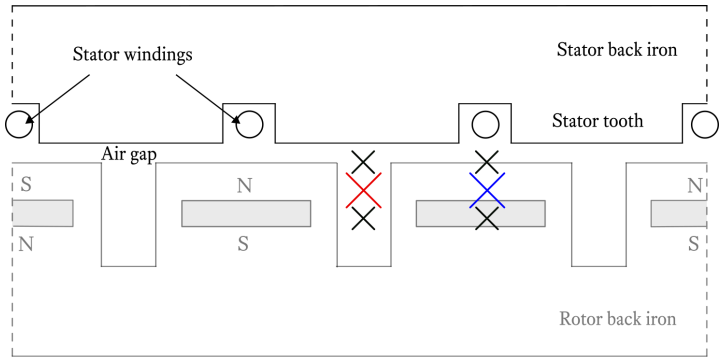

Figure 6.5. Probe locations in the measurement setup. Since the rotor is moving, all locations are relative to the stator.

The locations of the magnetic probe are pictured in Figure 6.5. Most of the experiments are conducted at the PM edge (red and blue cross in the figure). In order to see the effect of the stator winding, the probe tip is first aligned to a stator tooth and then moved to the area between two teeth. Also the radial distance from the stator winding is varied. The axial distance from the magnet is kept approximately at 5 mm in all cases.

The results shown in Figure 6.6 are from a probe that was positioned under a stator tooth. The motor was accelerated to its rated speed of 371 rpm and different load torques up to the rated torque were applied, increasing the stator current. Figure 6.6c represents a situation where the motor is accelerating while a load has been applied. In this situation the motor experiences a current that is larger than the rated current, so the distorting magnetic field from the stator is also stronger. The situation is common in elevator use. In this case the current is 150 % of the rated current. The increased current has a clear effect on the amplitude of the leakage flux. The shape of the sinusoidal signal also gets more distorted.

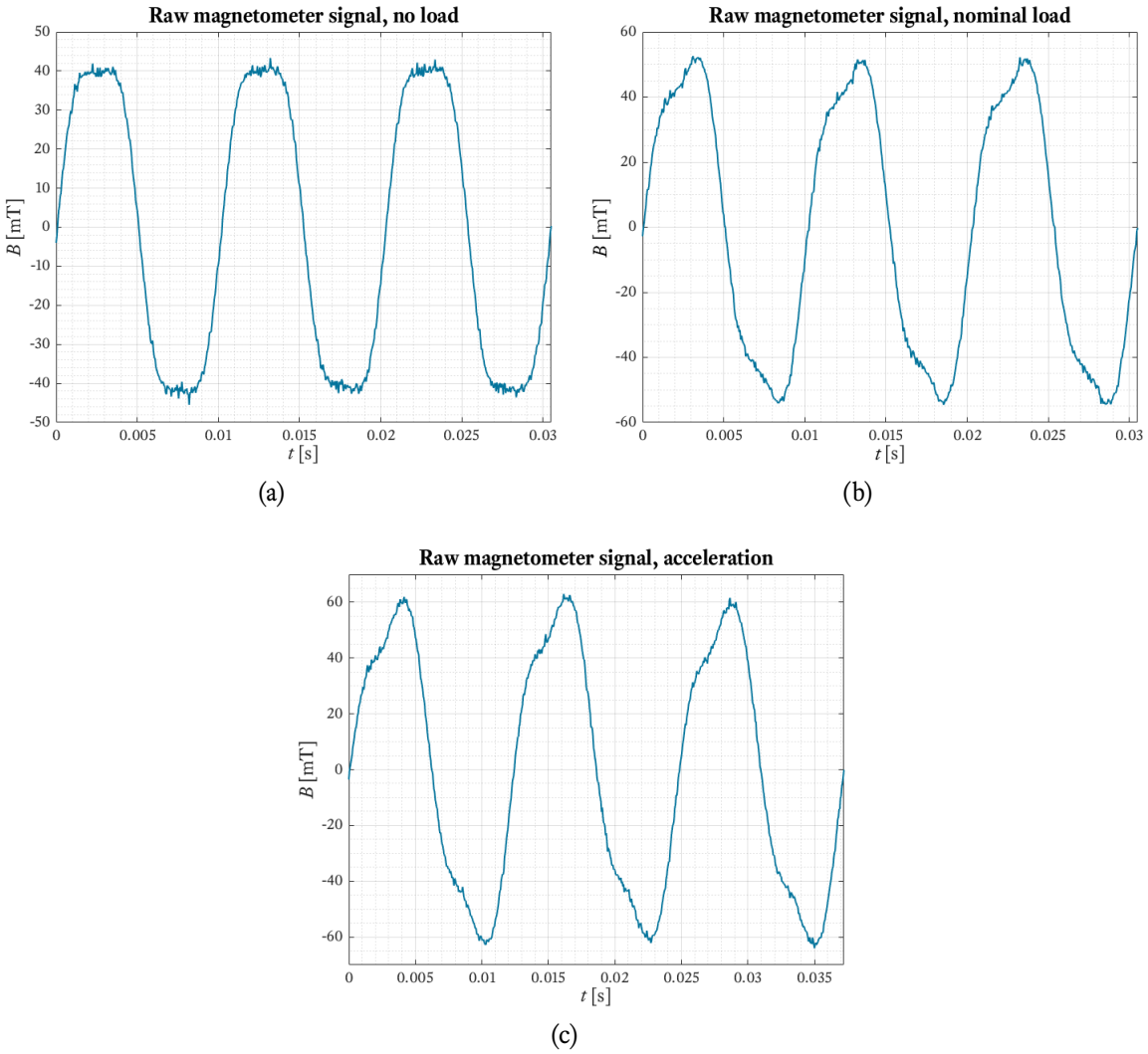

Figure 6.6. The leakage flux waveform at nominal speed measured under a stator tooth: (a) no-load current; (b) nominal current; (c) acceleration current.

In a following measurement, the probe tip is placed under a stator slot, and the same speed and

torque profile is applied to the motor. In Figure 6.7, the amplitude of the flux density is clearly not as affected by the stator currents as in the previous measurement. The third harmonic also has a different phase shift with respect to the fundamental harmonic.

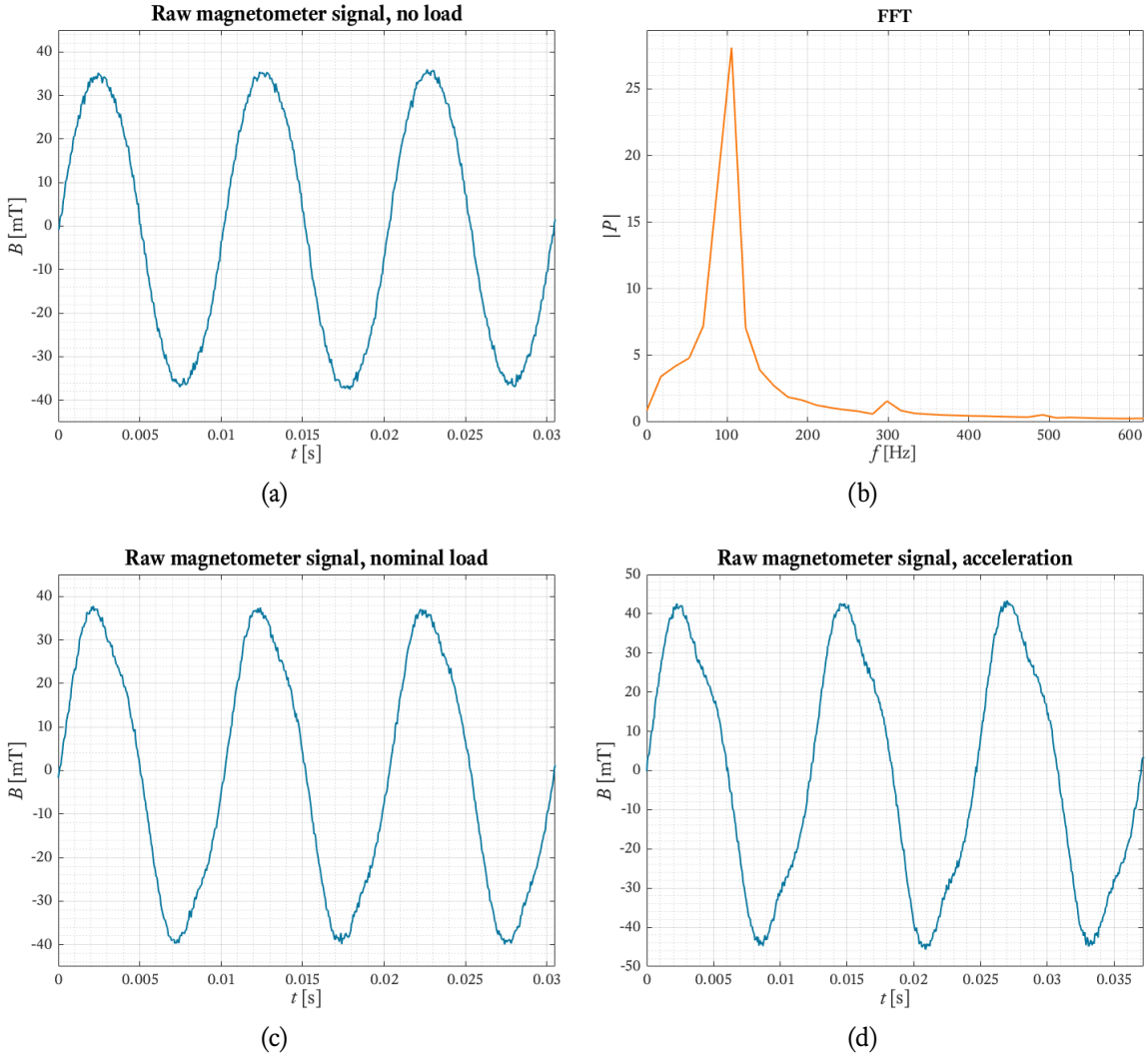

Figure 6.7. The leakage flux waveform at nominal speed measured under a stator slot: (a) no-load current; (b) FFT of a); (c) nominal current; (d) acceleration current.

The effect of the radial distance from the rotor is demonstrated by placing the sensor right next to the stator winding and in a subsequent measurement next to the rotor. In this case the probe is directly under a stator tooth. As seen in Figure 6.8, the flux amplitude has almost doubled near the stator. This probably happens because the magnetic flux is fringing from the air gap, affecting the magnet edge flux together with the end-winding currents.

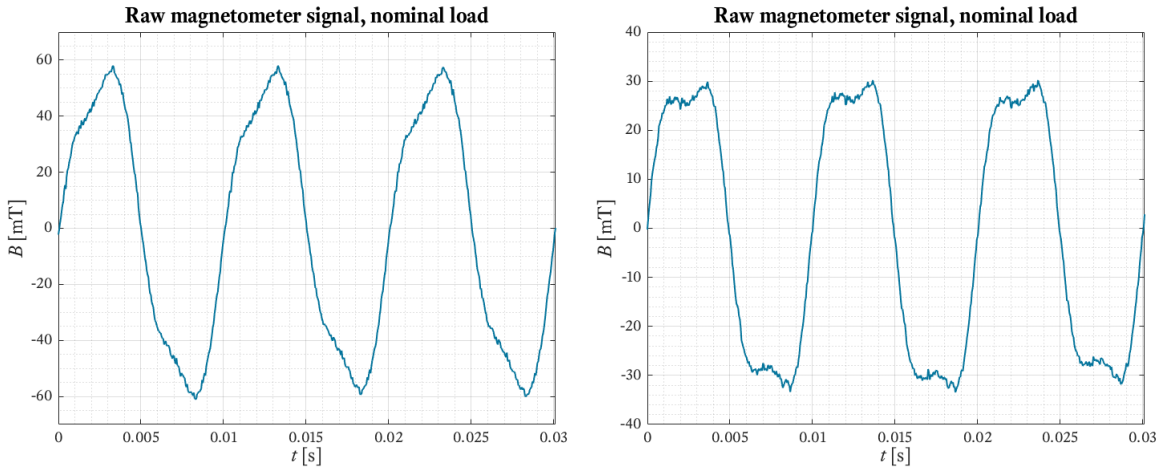

(a) (b)

Figure 6.8. The leakage flux waveform at nominal speed measured under a stator tooth: (a) next to the stator winding; (b) next to the rotor.

6.3 Machine 2

A major difference between the first and the second machine is that the second machine has an outer rotor structure. The rotor diameter is also much longer, 0.945 m. The rotor is equipped with embedded PMs and 40 pole pairs. A magnetometer probe is placed at the same distance from the magnets as with the previous machine, although in this case the machine also has a 2 mm non-magnetic metal sheet on top of the magnets. At first, the motor is rotated by hand. The measurement results are presented in Figure 6.9. The results are similar to machine 1, with a clear third harmonic component present.

Next, the motor is rotated with a frequency converter but without applying external load. Leakage flux is measured in the same manner as with machine 1. The best results are obtained when the probe is placed under a stator slot. The signals are presented in Figure 6.10. When the machine is driven at a constant speed, the Fourier transform shows only one frequency peak at the fundamental frequency and one at the third harmonic. The shape of the graph is much cleaner compared to 6.9b.

The leakage flux shows a clear periodicity in the amplitude of the flux, as shown in 6.11. It has a period of 40 sine cycles, therefore it occurs once per mechanical rotation. This is probably due to increase in the distance between the sensor and the magnet, so the rotor seems to have some structural deformation or axial run-out.

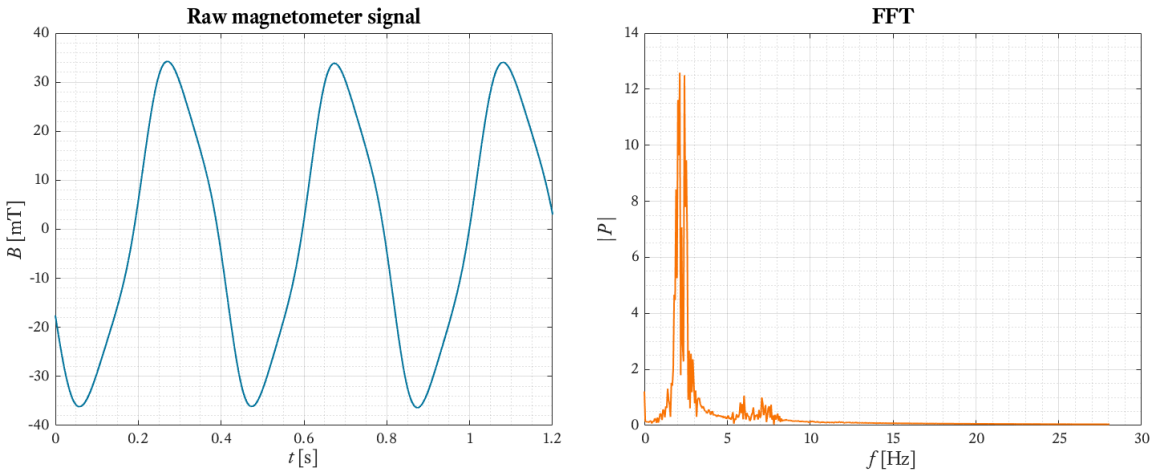

(a) (b)

Figure 6.9. The leakage flux waveform, rotated by hand: (a) shape of the leakage flux signal; (b) Fourier transform of the leakage flux signal.

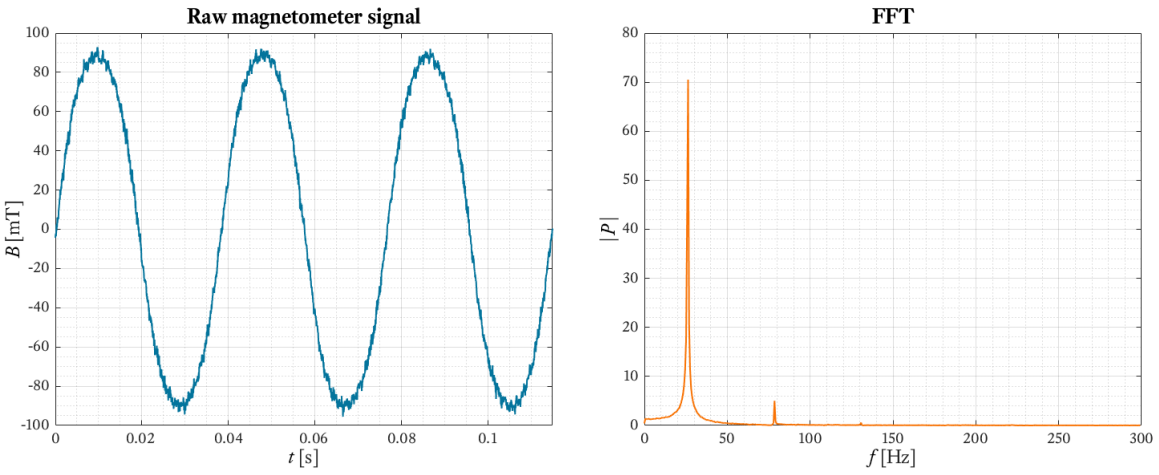

(a) (b)

Figure 6.10. The leakage flux waveform, rotated with a frequency converter: (a) shape of the leakage flux signal; (b) Fourier transform of the leakage flux signal.

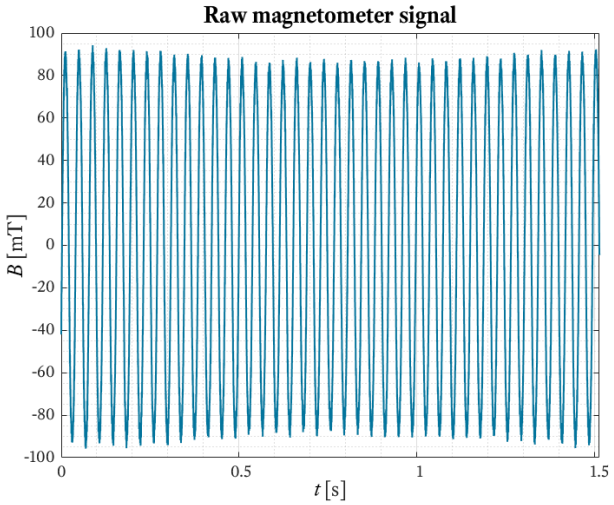

Figure 6.11. The leakage flux waveform, rotated with a frequency converter over one mechanical rotation.

Variations in the leakage flux amplitude are also studied. The machine is driven at its rated speed of 190 rpm for 17 seconds and the leakage flux is recorded. In post-processing, every full cycle in the stray flux signal is plotted to the same window. This way the variations in the flux magnitude over different parts of the sinusoidal period can be studied. The result is presented in Figure 6.12a. It contains approximately 2150 different sine periods. The variation is at maximum at the sine peaks, around 15 mT. This variation would have to be taken into account in the filtering system.

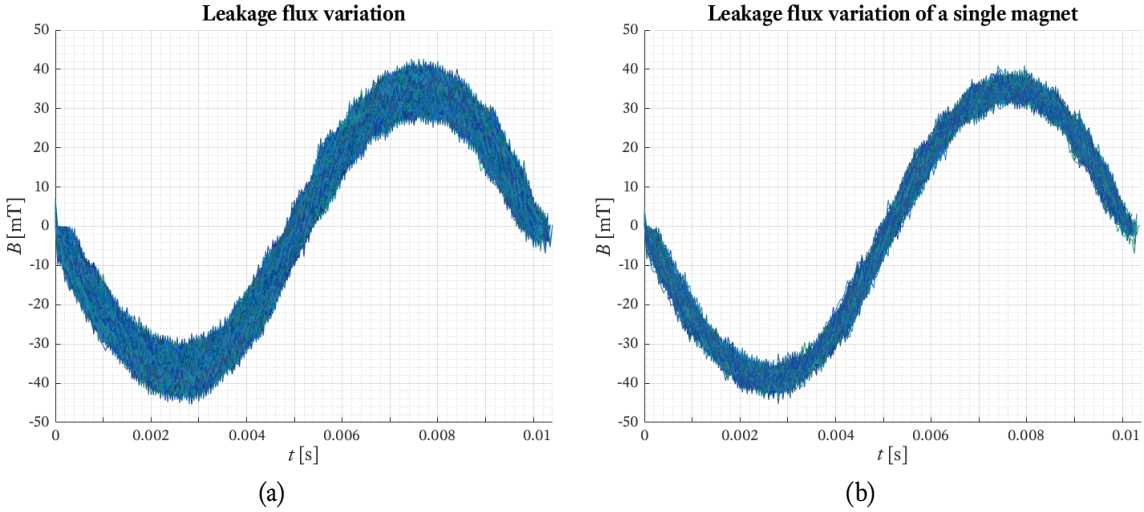

Figure 6.12. Variations in the leakage flux density waveform: (a) all magnets; (b) a single magnet.

In Figure 6.12b, a single magnet is picked from the motor diameter, and its leakage flux is plotted over several rotations as it passes the magnetometer. In practice this is possible by plotting every 40th sine period. As expected, the variation is smaller, approximately 10 mT at the sine peaks. Over constant speed, the sinusoidal waveform is still clearly recognizable and no outlier points are detected, which suggests that the flux follows a predictable pattern. The fluctuation shows clearly any deformations in the rotor structure.

6.4 Simulations with measured signals

The performance of the ANF-PLL filter is tested with the measurement results from Machine 1. The signals are transferred from Dewesoft X3 to MATLAB and fed to the simulation model. The experiment also models the effects of different nonidealities and error sources that are present in a real-world measurement system. In order to achieve this, the measurement results are filtered in different ways. A simple way to filter them is to apply a lowpass filter, which eliminates any ripple from the signal. The filtering is done with a third-order Butterworth filter, and its cut-off frequency is set so that the third harmonic is not removed.

The amplitude of the sine cycles in the leakage flux signal fluctuates. This is probably due to axial run-out of the rotor and slightly varying strengths of the magnets. The speed estimation accuracy can be improved if this fluctuation is corrected before further processing. The simulation model is unaffected by the absolute amplitude value, as long as the ratio of the fundamental to the harmonics stays the same. It is therefore possible to normalize all amplitudes to one and eliminate the amplitude error. A MATLAB script was written for this purpose and applied to the measured signals. Also, a test case correcting both the amplitude and ripple errors was created.

The two final tests include a case where no correction or filtering is performed, and a case where the signal is heavily corrected to almost sinusoidal by filtering it with a low-pass filter and applying the amplitude correction. In this case the third harmonic is also removed. The location of the PI-controller poles is set to a suitable value for each test. To summarize, different test cases are presented in Table 6.3.

The speed output is simulated in two cases: in no-load and with the rated load applied. In Figure 6.13, the filtered input signal for the simulation is presented on the left side and the speed

Table 6.3. Different correction factors.

	Amplitude correction	Ripple correction	3rd harmonic correction
Case 1	-	-	-
Case 2	X	-	-
Case 3	-	X	-
Case 4	X	X	-
Case 5	X	X	X

output is presented on the right side. The true rotor speed is measured with an incremental encoder and also plotted.

Looking at Figure 6.13b, it is obvious that some form of pre-filtering is needed before feeding the signal to the ANF-PLL filter; the resulting speed error can reach up to ±10 rad/s and it includes fast fluctuations from side to side. When correcting all amplitudes to the same level, the result is already significantly improved, the speed error being approximately ±2 rad/s or 0.5 %. It could be assumed that an elevator system can tolerate up to one percent errors in its electrical angular speed calculation. Therefore amplitude normalization would already bring the speed estimate to an acceptable level. However, although effective, this kind of normalization can be hard to realize in an online system, since the maximum and minimum values of one period are needed in the calculation.

Filtering out the high-frequency ripple has a similar effect to the estimated speed signal as amplitude normalization. It brings the error to a similar level. In this case the oscillations are also far less severe, resulting in a more confined output. Moreover, since the required low-pass filter has a high cut-off frequency, the inevitable phase shift on lower frequencies can be kept small.

In the next simulation, both the ripple and the amplitude correction is implemented. The speed output shows further improvement, bringing the error down to ±0.5 rad/s, as in Figure 6.14b. The third harmonic in the input signal is still fully present, so the ANF-PLL structure seems to filter it out successfully. In Figure 6.14c, the coefficients for the harmonic coefficients can be seen. According to the filter, the largest harmonic components are approximately 11 % of the fundamental harmonic. If the third harmonic is filtered before feeding the signal to the simulation, the speed output is further improved. With close to an ideal signal, only a ±0.2 rad/s

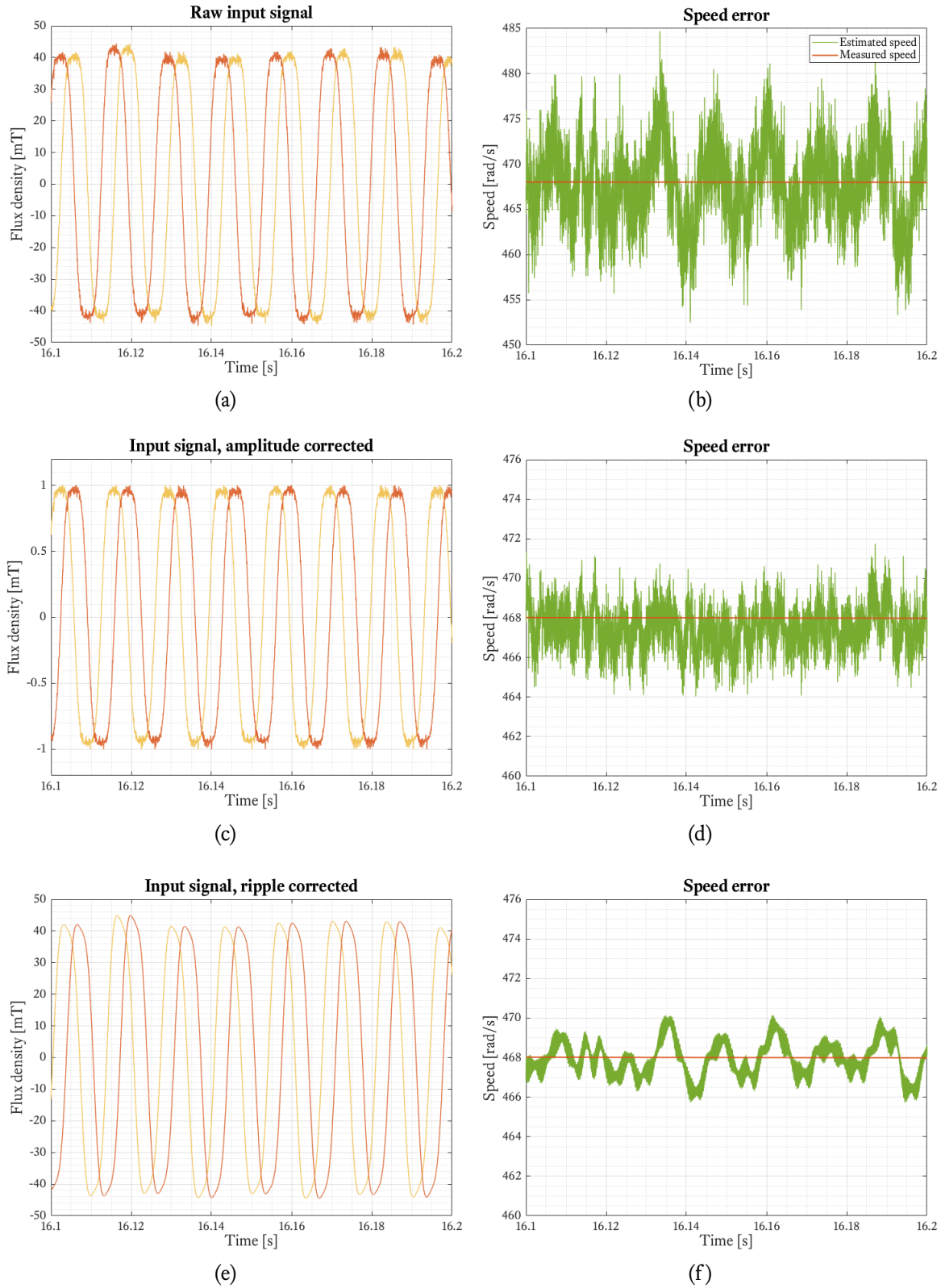

Figure 6.13. Simulated speed errors at no-load: (a) a raw input signal; (b) speed error with the raw signal; (c) an amplitude-corrected input signal; (d) speed error with the amplitude correction; (e) a ripple-corrected input signal; (f) speed error with the ripple correction.

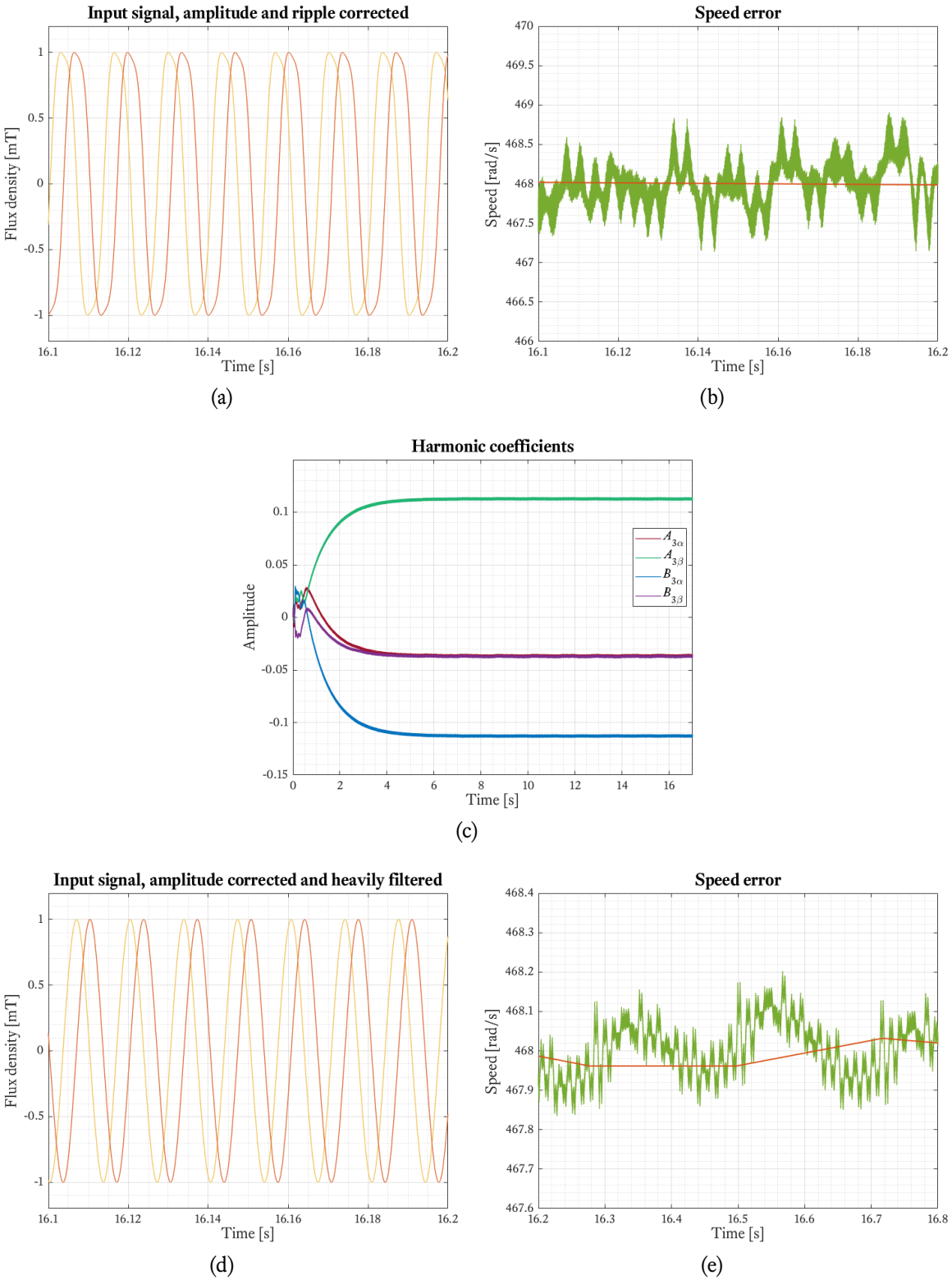

Figure 6.14. Simulated speed errors at no-load: (a) an amplitude- and ripple-corrected input signal; (b) speed error with the amplitude and ripple correction; (c) harmonic coefficients with the amplitude and ripple correction; (d) an amplitude-corrected and heavily filtered input signal; (e) speed error with the amplitude correction and heavy filtering.

error is expected. However, as discussed in previous sections, this kind of heavy filtering also creates a large phase delay.

In all cases the speed error is distributed evenly in both sides of the true speed. This is an encouraging result, and raises the possibility for some kind of averaging that would bring the error closer to zero. However, given that the speed measuring system is very time-critical, such averaging might be too time-consuming.

As seen in section 6.2, the leakage flux shape changes when current is applied to the stator winding. Next, the error analysis is repeated with measurements obtained from applying 1.5 times the nominal current to the stator winding to see if it has an effect to the error. Under normal operating conditions, the maximum current occurs when the motor is acceleration under load.

In general, the speed errors are on the same level as without the stator current. See Figures 6.15 and 6.16. A large current has most notably an effect on the third harmonic, which the ANF-PLL setup filters effectively. Other error sources like the amplitude fluctuation or signal ripple are on the same level, and the speed error reflects that.

Besides amplitude- and harmonic-related nonidealities, a phase error between the magnetic sensors can cause oscillations in the speed output. Since only one magnetometer is used in the experiments, an artificial phase error is added manually to the simulation. Instead of the ideal 90 degrees, the phase shift between the two signals is set to 99 degrees. The resulting speed output is presented in Figure 6.17. To isolate the phase error effect, an amplitude- and ripple-corrected input signal is used.

Compared to the situation without phase offset, the speed error has increased from ±1 rad/s to ±2 rad/s. Similar behavior is noticed both when increasing and decreasing the phase angle from the ideal value. The error increases nearly linearly with a rate of ±1 rad/s for every ten percent increase or decrease in the phase angle. Like the other error sources, a phase error only increases the variation of the speed signal, and does not create any speed offset. Still, it can be concluded that a phase error has a significant effect on the speed estimation accuracy. Some methods to mitigate this effect are described in the discussion section.

It should be noted that since a constant phase shift between the two magnetometer signals was used, any rapid oscillations in the speed are not visible in the simulation input. Although machine inertia prevents most of these oscillations, this brings a small degree of uncertainty in

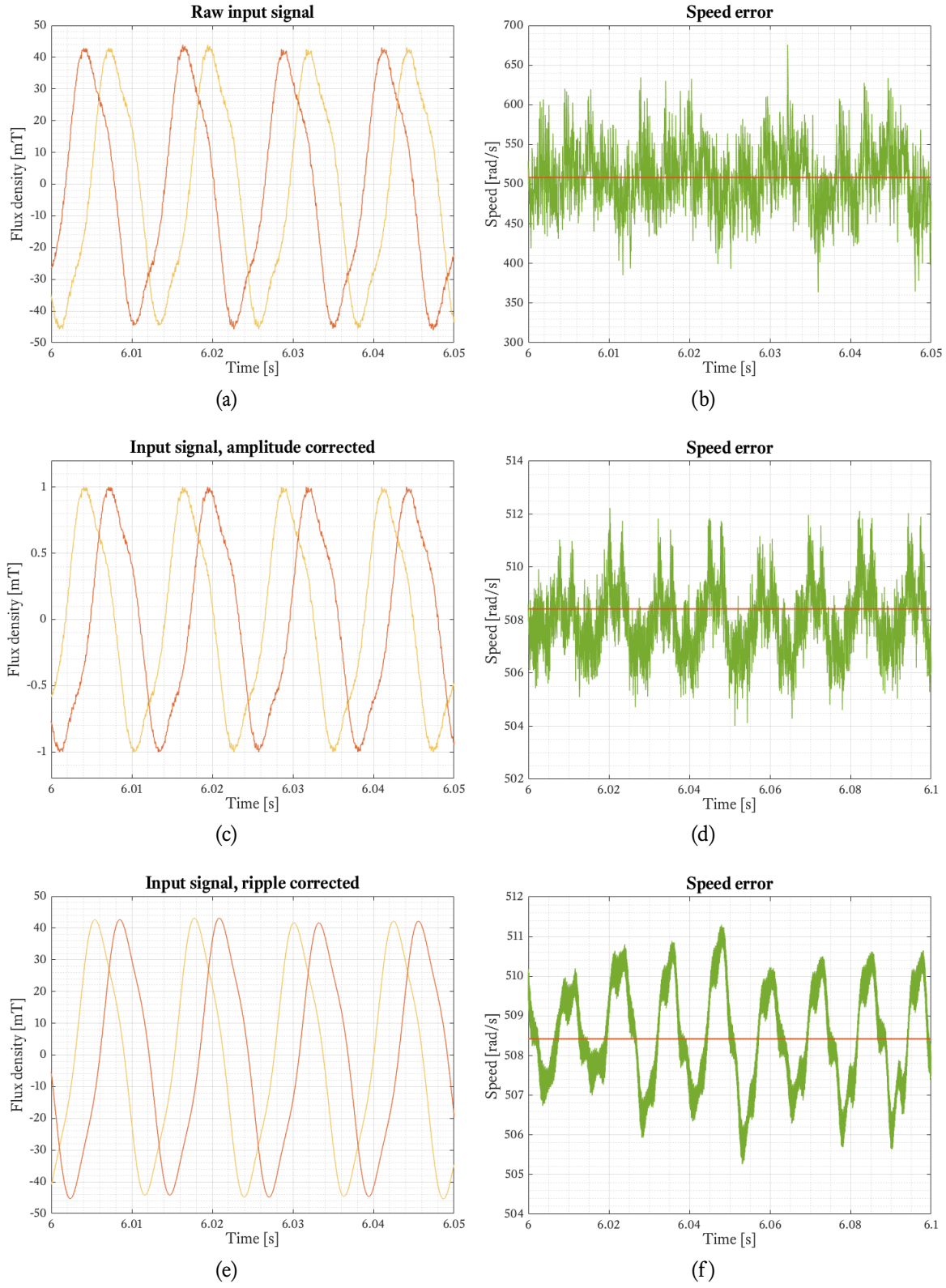

Figure 6.15. Simulated speed errors with an acceleration current: (a) a raw input signal; (b) speed error with the raw signal; (c) an amplitude-corrected input signal; (d) speed error with the amplitude correction; (e) a ripple-corrected input signal; (f) speed error with the ripple correction.

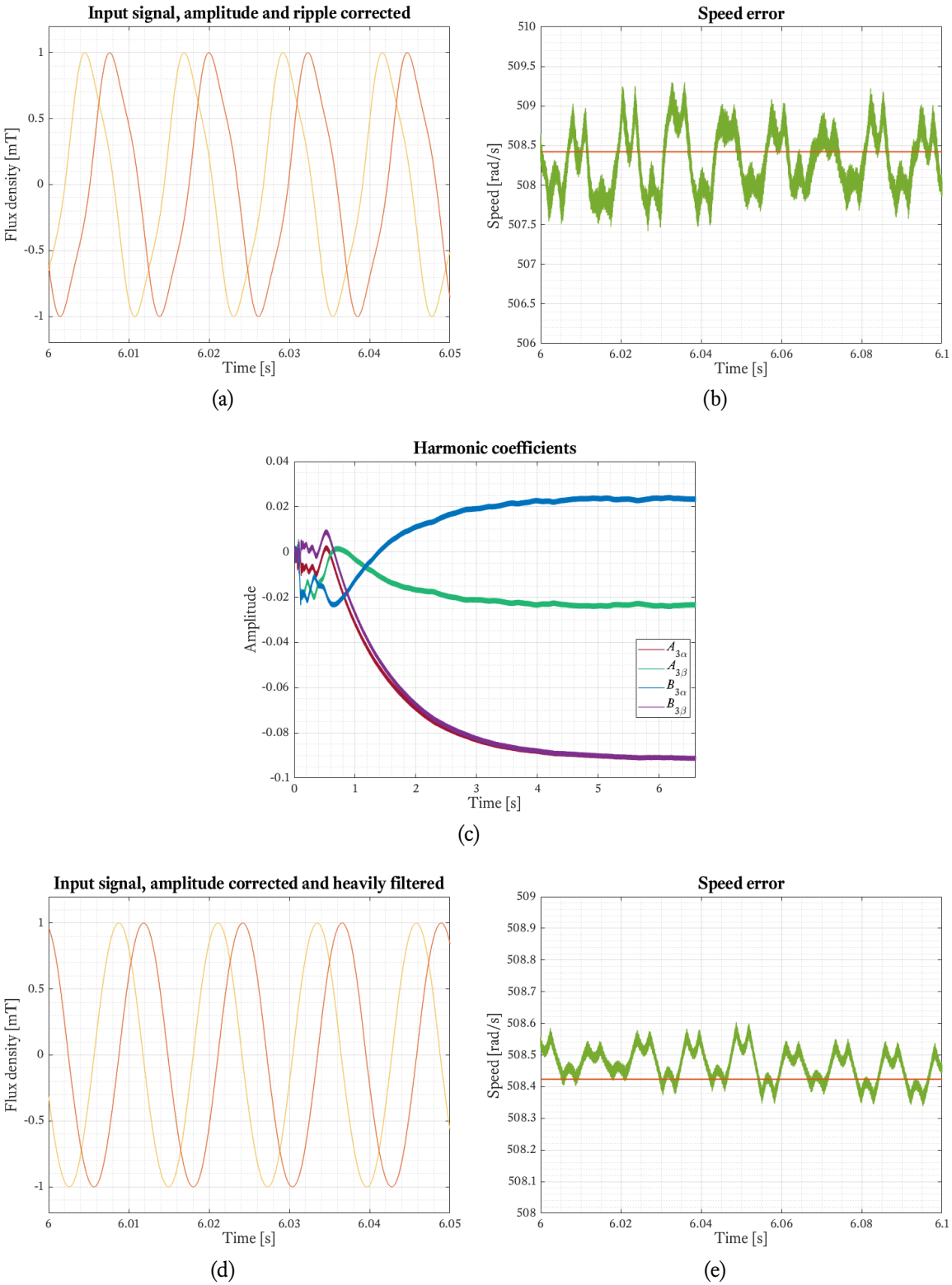

Figure 6.16. Simulated speed errors with an acceleration current: (a) an amplitude- and ripple-corrected input signal; (b) speed error with the amplitude and ripple correction; (c) harmonic coefficients with the amplitude and ripple correction; (d) an amplitude-corrected and heavily filtered input signal; (e) speed error with the amplitude correction and heavy filtering.

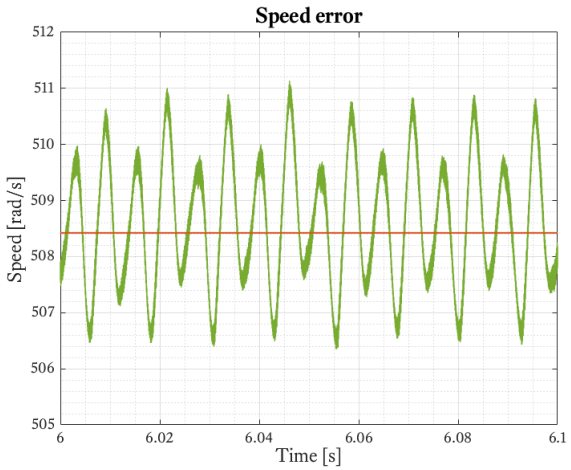

Figure 6.17. The speed output with a 10 percent phase error.

the simulation results.

6.5 Discussion

Based on the measurements described in the previous section, some conclusions can be drawn. When estimating the rotor position with magnetic sensors, the accuracy of the measurement depends on several factors. If the angle calculation is done by measuring two signals and treating them as sine and cosine, their amplitudes should be equal and the phase-shift between them should be 90 degrees, i.e. they should be orthogonal. Any variations in these two requirements will introduce uncertainty in the measurement. Most error sources can be thought as disturbances to either amplitude or phase.

The leakage flux pattern formed by the PMs is not perfectly sinusoidal. The main error sources that distort the shape are:

1. Variations in the magnetization of the PMs
2. Rotor deformations causing anomalies in the measurement signal
3. Axial run-out of the rotor
4. Harmonics in the magnetic flux density

Out of these factors, 1, 2 and 3 cause a non-zero DC-component to the sensor output, which is

then seen as an amplitude error. An amplitude error can be modeled as

$$\hat{\theta} = \tan^{-1}\left(\frac{U_{\sin}}{U_{\cos}}\right) = \tan^{-1}\left(\frac{A_0 + A_1 \sin\theta}{A_0 + A_1 \cos\theta}\right), \tag{6.1}$$

where $\hat{\theta}$ is the decoded electrical angle, θ is the real angle, A_0 is the DC-component and A_1 is the amplitude of the fundamental frequency. Similarly, an orthogonality error between sine and cosine can be expressed as

$$\hat{\theta} = \tan^{-1}\left(\frac{A_1 \sin(\theta + \delta)}{A_1 \cos\theta}\right), \tag{6.2}$$

where δ is the angle error. Finally, a harmonic error with a third harmonic component can be modeled as

$$\hat{\theta} = \tan^{-1}\left(\frac{A_1 \sin\theta + A_3 \sin 3\theta}{A_1 \cos\theta + A_3 \cos 3\theta}\right). \tag{6.3}$$

It is clear that compensating actions should be made to ensure good estimation accuracy. To mitigate amplitude errors, the magnets in the rotor should be pre-selected so that they have similar performance. To avoid harmful effects to the magnetic field density caused by temperature variations, magnetic material with good temperature stability, like SmCo, should be chosen. The Hall effect sensors themselves can also have temperature compensation, so in a multiple-sensor setup similar sensors should be used.

Errors caused by items 2, 3 and 4 can be compensated by using several magnetometers. For example, errors in the sine and cosine signal forming can be mitigated by using four sensors instead of just two and feeding each pair to a differential amplifier. The amplifier would receive both the original signal and its inversion. The method would provide better external noise immunity.

Assume that there should be a 180 degree phase shift between two sensors named H1 and H2, but in reality there is some misalignment. When the phase of sensor H1 is leading the ideal sine curve by θ_1 and sensor H2 is lagging it by θ_2, a new phase can be calculated with $(\theta_1 - \theta_2)/2$. On the other hand, if both sensors are leading the phase of the ideal sine curve, a

new phase can be calculated with $(\theta_1 + \theta_2)/2$, as shown in Figure 6.18. Although the error will not be compensated completely, in both cases the final phase error will decrease. A case with both sensors phase-lagging is similar to the case with both sensors phase-leading. However, it should be noted that any DC-component in the output signal should be compensated before phase correction, since a differential amplifier will amplify any DC-offset. (Hu et al., 2012)

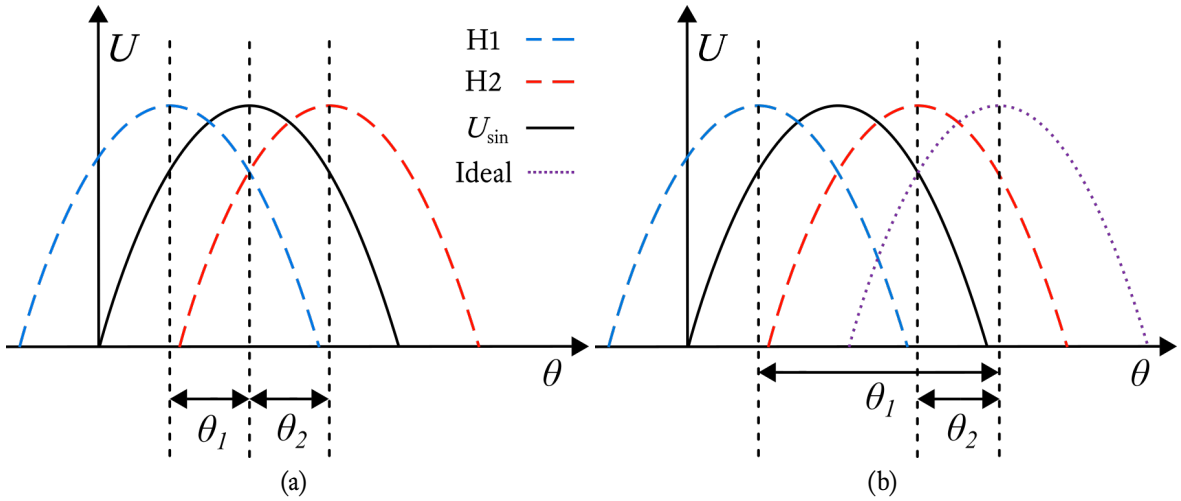

Figure 6.18. Compensation of phase errors in Hall signals: (a) leading and lagging signals. $U_{\sin}$ and the ideal signal are on top of each other. (b) Both signals leading. (Hu et al., 2012)

The number of magnetic sensors can be increased in pairs, $N = 2^i, i = 1, 2, 3...$ Best results can be achieved when the sensors are mounted over one electrical period, since variable magnetic field strengths of different magnets can otherwise cause errors. Due to constraints in the size of the sensors and the physical length of one electrical period on the rotor, $N = 4$ should be applicable in most cases.

Chapter 7

Conclusions

Implementing a speed and position feedback system based on the leakage flux is not an easy task. The leakage flux is highly analog by nature, and transforming it to a reliable digital signal is challenging. The signal should be in a form that can be read by a frequency converter. The task is not made easier by the especially strict ride comfort requirements present in the elevator industry.

By feeding a real leakage flux signal to the simulation model, it was shown that it is possible to extract speed information from the leakage flux. In an elevator system, electrical angular speed errors less than one percent can be tolerated. If the signal is fed to the simulation without filtering, the speed error exceeds this limit, so further pre-processing is required. By removing high-frequency ripple from the signal with a low-pass filter, the speed error can be brought to an acceptable level. Recalling the thesis question from the introductory section of Chapter 1:

"Is it possible to use the magnetic leakage flux from a PMSM as a feedback signal in order to accurately control the speed and position of an elevator?"

Based on the results obtained in this thesis it can be concluded that the thesis question, at least up to this point, stands true. Since the discussed method was not implemented into a real elevator system within the scope of this thesis, a final confirmation is still missing. However, with adequate error correction, the calculated speed signal was shown to follow the true speed accurately. In addition, any variations are evenly distributed around the true speed. It is correct to assume that the rotor speed information is available in the leakage flux waveform.

As described in the experimental section, the leakage flux was measured with a magnetometer and its location was varied. The flux shape was affected by the stator end-winding currents. When a probe was placed under a stator slot, the deformation was less severe compared to placing the probe under a stator tooth. Under a tooth the end-winding is perpendicular to the radial direction of the machine and extend farthest out from the machine, which could make it easier for its flux to influence the measurement. As the magnetometer probe is moved closer to the rotor, the effect of the end-winding is reduced. The flux from the PMs is also reduced, but not enough to prevent reliable measurements. Based on these results, under a stator slot and close to the rotor seems to be the best location for a magnetometer.

The ANF-PLL method used in this thesis relies on being able to estimate the harmonic components in the leakage flux in real time. The estimation takes several seconds to converge, which is not acceptable at elevator start-up. It was proposed that the coefficients for the harmonic components could be pre-calculated and stored to the memory of the system. This way the speed estimation could work properly also during start-up and zero-crossing. The end-winding currents also have an effect to the harmonic coefficients. Therefore it would not be enough to store only one set of coefficients. Instead, they should be available for the whole load range in which the elevator is operating.

7.1 Summary

In this thesis, a system for estimating the speed of a PMSM based on its magnetic leakage flux was investigated. To begin with, traditional speed measurement and PMSM control methods were introduced. An analytical model of different components of the leakage flux was investigated in order to better understand the behavior of the flux and the ways it could be measured. It was concluded that in a radial type PMSM, the magnetic flux flowing in the radial or tangential direction would be difficult to measure. The situation is similar in an axial flux machine, so it was decided to focus on the edge leakage from the PMs in a radial flux machine. Three magnetic flux measurement devices potentially suitable for this application were covered. Out of those three, Hall sensors were used as an example further in the thesis.

Prior measurements of the leakage flux showed that as the PMs rotate, the flux amplitude resembles a sine wave. A clear third harmonic component was also identified in the signal. Based on this result, angle detection algorithms used by sinusoidal encoders were investigated in order

to have a broader view of different methods that could be used for extracting angle information from a sinusoidal signal. In the end, a method based on an adaptive notch filter and a phase-locked loop was selected for further analysis. The advantage of this method is that it takes into account the possible changes to the third harmonic and does not introduce a large phase shift between the input and output signals, which makes it more suitable for real-time measurement.

A simulation model based on the ANF-PLL filter was built in Simulink and tested with cases representing the speed profile of an elevator. It was noticed that the filter was indeed effective in calculating the speed signal, but it took several seconds for it to start functioning properly. This requires special attention in an elevator system since power-saving features are often used, cutting power to the filter. The filter was modified and tested again with similar speed profiles. The modification performed as expected, enabling speed measurements starting from stand-still. However, it also limited the filter's real-time capabilities in the event of sudden change in the leakage flux profile, which can occur for example in case the measurement probe moves to a different location.

A measurement setup was built in order to obtain real leakage flux data for further analysis. An IPMSM was rotated both with and without load, and the shape of the leakage flux was recorded. Two different types of IPMSMs showed similar leakage flux shapes with a clear third harmonic component present. As the load of the motor increased, the effect of the flux created by the stator currents started to show. By changing the location of the magnetic probe, it was shown that the stator current had least effect when the measurement was done under a stator slot.

A substantial part of the analysis focused on how different nonidealities would affect the measurement result. In simulation, one magnet that had lower flux density amplitude than the others produced a clear but quickly disappearing error to the results. Since in reality all of the amplitudes have a slightly different value, it produces a continuously varying error. This was confirmed by feeding previously recorded leakage flux signals to the simulation. It was concluded that both the amplitude variations and the high frequency ripple in the measurement signal created the biggest fluctuations to the speed output. The effect of the third harmonic was small since it was handled by the filter. Finally, the compensation of phase error in the filter input was discussed since in a real system it would also create a separate error component.

7.2 Future work

Although this thesis provides useful data about using the leakage flux as means of measuring the speed of a PMSM, it is hardly a complete description of the topic. In developing a leakage flux–based system, a long-term goal would be the development of a working prototype that uses signals from several magnetometers, executes on-line calculations and outputs speed and position data that an existing frequency converter could understand. As an online system, special attention should be paid into shortening the computation times and phase delays of the system. The phase-locked loop used in the simulation section of this thesis is useful in minimizing phase delays, but as previously concluded, the input for the filter requires further pre-filtering. These filters can introduce additional phase delays.

Due to time constraints, only one magnetometer was used in the experimental section. A logical next step would be to repeat the measurements using multiple probes, as was described in section 4.2. Combining the signals could possibly compensate phase shift errors in the final output. In addition, experiments should be conducted using Hall effect sensors or other small and inexpensive magnetometers. In this thesis an accurate magnetometer was used in order to detect any variations in the leakage flux, but in a real system, the limited measurement range of cheap sensors should be taken into account to prevent signal clipping. With multiple sensors, the computational burden also increases, prolonging the signal processing time. Even small delays can cause torque ripple. All in all, realizing an online system would need closer examination regarding signal delays, DSP choice and implementation of the computing steps.

The magnetic probe that was used to measure the leakage flux was affected by the flux from the stator currents, which also deteriorated the performance of the speed estimation system. The effect of the stator currents could possibly be attenuated by constructing a case or some other type of protection around the measurement probes. The case would have to be designed in a way that blocks flux from the stator but does not affect flux from the magnets. It could be investigated whether adding the protection would be worth the additional cost.

A different approach to the speed estimation not investigated in this thesis would be to utilize the third harmonic in the leakage flux instead of the fundamental harmonic. In case the fundamental could be filtered and only the third harmonic would remain, there would be three times the amount of full sinusoidal cycles compared to the fundamental. In theory, this would also mean three times the resolution in the speed measurement system. Some of the drawbacks in this approach would be a smaller amplitude of the leakage flux signal and possibly a large phase

delay due to heavy filtering.

Bibliography

Adam, A., Gülez, K. and Koroglu, S. (2011), 'Stray magnetic field distributed around a PMSM', *Turkish Journal Of Electrical Engineering And Computer Sciences* **19**, 119–131.

Best, R. E. (2007), 'Phase locked loops: Design, simulation, and applications: 6th edition'. McGraw-Hill Education.

Burke, J., Moynihan, J. F. and Unterkofler, K. (2000), 'Extraction of high resolution position information from sinusoidal encoders', *Proceedings of the international intelligent motion conference,* pp. 217–222.

Chang, Y.-C. and Tzou, Y.-Y. (2007), 'Design of a digital servo control IC for permanent magnet synchronous motors with linear hall sensors', *IEEE Power Electronics Specialists Conference 2007,* pp. 599–605.

Eitel, E. (2014), 'Basics of rotary encorers: Overview and new technologies', `http://www.machinedesign.com/`. Online; accessed 26. April 2018.

Ellis, G. (2002), 'Observers in control systems: A practical guide'. Elsevier Science, pp. 177-178.

Ertan, H. B. and Keysan, O. (2009), 'External search coil as a means of measuring rotor speed of an induction motor', *2009 8th International Symposium on Advanced Electromechanical Motion Systems Electric Drives Joint Symposium,* pp. 1–6.

Eskola, M. (2006), 'Speed and position sensorless control of permanent magnet synchronous motors in matrix converter and voltage source converter applications'. Doctoral thesis. Tampere University of Technology.

Goktas, T., Lee, K. W., Zafarani, M. and Akin, B. (2016), 'Analysis of magnet defect faults in permanent magnet synchronous motors through fluxgate sensors', *2016 IEEE Applied Power Electronics Conference and Exposition (APEC),* pp. 2875–2880.

Goktas, T., Zafarani, M., Lee, K. W., Akin, B. and Sculley, T. (2017), 'Comprehensive analysis of magnet defect fault monitoring through leakage flux', *IEEE Transactions on Magnetics* **53**(4), 1–10.

Hanselman, D. (2006), 'Brushless permanent magnet motor design'. Magna Physics Publishing, pp. 67-72.

Hohner Automáticos (2015), 'Interpolated signals', `http://www.encoderhohner.com/interpolated-signals/`. Online; accessed 20. May 2018.

Hu, J., Zou, J., Xu, F., Li, Y. and Fu, Y. (2012), 'An improved PMSM rotor position sensor based on linear Hall sensors', *IEEE Transactions on Magnetics* **48**, 3591–3594.

Hwang, C.-C. and Cho, Y. H. (2001), 'Effects of leakage flux on magnetic fields of interior permanent magnet synchronous motors', *IEEE Transactions on Magnetics* **37**(4), 3021–3024.

iC Haus GmbH (2014), 'High-precision sine/cosine interpolation'. White paper.

Imperial College London (2008), 'How a fluxgate works', `http://www.imperial.ac.uk/`. Online; accessed 20. May 2018.

Jokinen, M. (2018). Senior chief design engineer. An interview.

Jung, S., Lee, B. and Nam, K. (2010), 'PMSM control based on edge field measurements by Hall sensors', *2010 Twenty-Fifth Annual IEEE Applied Power Electronics Conference and Exposition (APEC),* pp. 2002–2006.

Jung, S. Y. and Nam, K. (2011), 'PMSM control based on edge-field Hall sensor signals through ANF-PLL processing', *IEEE Transactions on Industrial Electronics* **58**(11), 5121–5129.

Kim, S. Y., Choi, C., Lee, K. and Lee, W. (2011), 'An improved rotor position estimation with vector-tracking observer in PMSM drives with low-resolution Hall-effect sensors', *IEEE Transactions on Industrial Electronics* **58**(9), 4078–4086.

Kiss, G. M. and Vajda, I. (2014), 'Magnet leakage flux of axial flux PM synchronous machines for EV', *2014 IEEE International Electric Vehicle Conference (IEVC),* pp. 1–5.

Kivimäki, O. (2005), 'Takometrin nopeusmittavirheiden kompensointi'. Master's thesis, Helsinki University of Technology.

Kokko, V. (2003), 'Condition monitoring of squirrel-cage motors by axial magnetic flux measurements', *Acta Universitatis Ouluensis. C, Technica*. Faculty of Technology, University of Oulu.

Lee, S. G. and Kim, W. H. (2017), 'A study on the axial leakage magnetic flux in a spoke type permanent magnet synchronous motor', *2017 IEEE International Electric Machines and Drives Conference (IEMDC),* pp. 1–6.

Lee, S. T., Kim, Y. K. and Hur, J. (2017), 'Pseudo-sensorless control of PMSM with linear Hall-effect sensor', *2017 IEEE Energy Conversion Congress and Exposition (ECCE),* pp. 1896–1900.

Lidozzi, A., Solero, L., Crescimbini, F. and Napoli, A. D. (2007), 'SVM PMSM drive with low resolution Hall-effect sensors', *IEEE Transactions on Power Electronics* **22**(1), 282–290.

Luo, S. and Hou, Z. (1995), 'An adaptive detecting method for harmonic and reactive currents', *IEEE Transactions on Industrial Electronics* **42**(1), 85–89.

Perera, C. (2003), 'Sensorless control of permanent-magnet synchronous motor drives'. Doctoral thesis. Institute of Energy Technology, Aalborg University.

Prentice, M. (2018), 'Resolvers 101'. White paper by Dynapar.

Pyrhönen, J., Hrabovcova, V. and Semken, R. S. (2016), 'Electrical machine drives control: An introduction'. Wiley.

Pyrhönen, J., Jokinen, T. and Hrabovcova, V. (2009), 'Design of rotating electrical machines'. Wiley. Chapter 4.

Qu, R. and Lipo, T. A. (2004), 'Analysis and modeling of air-gap and zigzag leakage fluxes in a surface-mounted permanent-magnet machine', *IEEE Transactions on Industry Applications* **40**(1), 121–127.

Rajput, R. K. (2009), 'Basic electrical engineering'. Laxmi Publications Ltd.

Sick Stegmann (1999), 'ADMC401 as an interface to the Stegmann SINCOS® encoder'. Application note.

Sick Stegmann (2016), 'Operating instructions | Specification Hiperface®: Motor feedback protocol'. Protocol specification.

Tsai, W.-B. and Chang, T.-Y. (1999), 'Analysis of flux leakage in a brushless permanent-magnet motor with embedded magnets', *IEEE Transactions on Magnetics* **35**(1), 543–547.

Wenlin, H. (2018). Electrical desing specialist. An interview.

Yang, Y. P. and Ting, Y. Y. (2014), 'Improved angular displacement estimation based on Hall-effect sensors for driving a brushless permanent-magnet motor', *IEEE Transactions on Industrial Electronics* **61**(1), 504–511.

Appendix 1. Simulation schematic

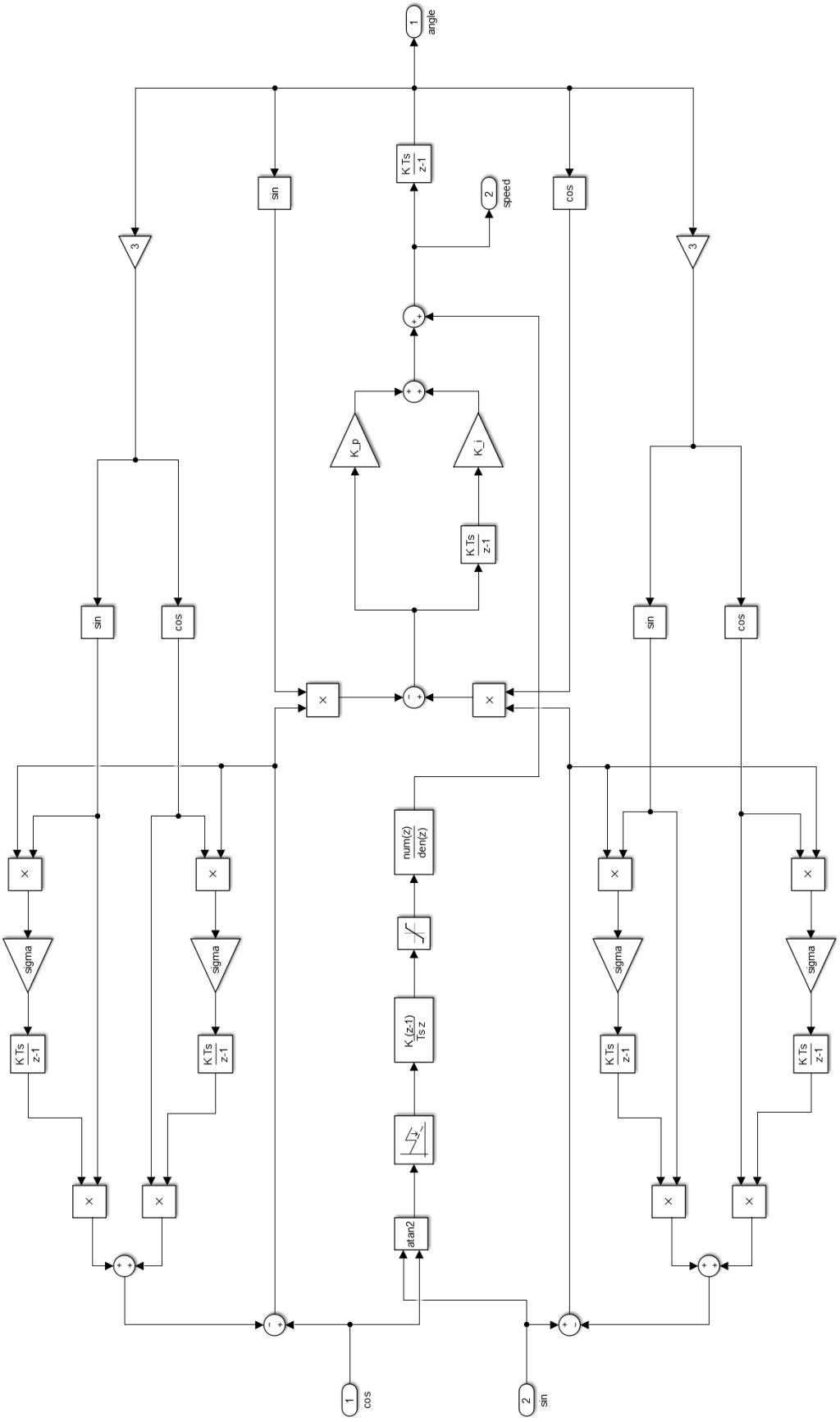

Figure A1.1. Complete filter schematic